CRANFIELD UNIVERSITY

SABINO LOIODICE

MODELLING NOISE FROM ROTATING SOURCES IN SUBSONIC AND SUPERSONIC REGIMES

SCHOOL OF ENGINEERING

Ph.D. THESIS

CRANFIELD UNIVERSITY

SCHOOL OF ENGINEERING

Ph.D. THESIS

Academic Years 2004-07

SABINO LOIODICE

Modelling noise from rotating sources in subsonic and supersonic regimes

Supervisor: Prof. Dimitris Drikakis

2008

This thesis is submitted in fulfilment of the requirements for the Degree of

Doctor of Philosophy

Abstract

Noise is an environmental concern and due to the increasing interest in helicopters as an alternative inter-city transportation, research for more environment friendly helicopters is continuously growing. Building on this demand, this study aims at finding an efficient and accurate noise prediction tool for rotating sources.
This study therefore investigates the modelling of noise from rotating sources such as helicopter rotors by addressing noise propagation in both subsonic and transonic/ supersonic regimes. The aim of this research is to explore the field of aeroacoustics prediction for rotor generated noise and to develop a noise prediction tool for sources moving in subsonic or supersonic flow regimes. The aeroacoustics predictions presented have been obtained using a hybrid approach. With such an approach the near field noise generation process is simulated by means of an aerodynamics prediction tool while the noise propagation to the near field is computed by mean of the Ffowcs Williams-Hawkings equation in time domain.
For the near-field aerodynamic calculations different CFD tools have been exploited. More precisely, three test cases have been analysed. For the first test case of 2D aerofoil-vortex interaction, reproducing the experimental campaign of Lee et al., the near-field is computed via the commercial software Fluent. The unsteady implicit Euler solver with second order discretisation both in space and in time is exploited. This uses the ROE FDS scheme for the fluxes calculation. The same solver is used in the near-field simulations of the third test case, where the analysis of a non-lifting hovering rotor is carried out in delocalised conditions, reproducing the experiments of Purcell on the UH1H model rotor. The second test case analysed is based on the HELISHAPE experimental campaign for the ONERA model rotor in BVI conditions. Two comprehensive codes, from Agusta-Westland and Roma Tre, are used to simulate the complex aeromechanics of the rotor in low speed descent.
The noise propagation phase has been performed via the new noise prediction tool developed during this study, named HelicA (for Helic-opter A-coustics). This tool is based on the Emission Surface formulation and exploits a novel root finder and Emission Surface construction algorithms. It can use control surfaces which are in subsonic or transonic/supersonic conditions. Verification and validation processes have been performed on the noise prediction tool before using this code in the aforementioned test cases. These processes are based on the comparison of the tool's predictions with available analytical and numerical results. The verification and validation cases include sources moving at Mach numbers ranging from $M_T = 0$ to $M_T > 1$. The noise prediction tool is applied to the three aforementioned test cases and the results are in very good agreement with the measurements even for the strong shock delocalisation cases.

Acknowledgements

I would like to sincerely thank the people supported me through the completion of this project:

My supervisor, *Prof. Dimitris Drikakis*, for his invaluable guidance, help and support over the period of this research.

I would like to express my gratitude to *Prof. Anastasios Kokkalis* (visiting Professor in the Fluid Mechanics and Computational Science Group) for his continual support and shared expertise that made this project possible.

I also acknowledge the European Commission and the "Friendcopter" FP6 project for funding this research and the project partners, in particular *Prof. Massimo Gennaretti* and *Dr.Giovanni Bernardini*, for their help and advices.

I thank also the staff and colleagues at Cranfield University for their support. My friends for all the good times and for making my period at Cranfield very enjoyable.

A particular thank to my friend *Timos* for his help and his patience in reading this work.

to Alexandra, my mother and my family for their love and support.

All truths are easy to understand once they are discovered;
the point is to discover them.
Galileo Galilei

Contents

List of Figures

List of Tables

Nomenclature

Acronyms

ADV	Advanced or Forward time algorithm
APE	Acoustic Perturbation Equations
BERP	British Experimental Rotor Program
bpf	blade passage frequency
BR	engine Bypass Ratio
BVI	Blade Vortex Interaction
BWI	Blade Wake Interaction
CAA	Computational AeroAcoustics
CFD	Computational Fluid Dynamics
CS	Collapsing Sphere
DNC	Direct Noise Computation
DNS	Direct Numerical Simulation
DNW	Dutch German Windtunnel
ES	Emission Surface
FAR	Federal Aviation Regulations
FDS	Flux Difference Splitting
FW-H, FWH	Ffowcs Williams - Hawkings equation
GL	Gauss-Legendre
HSI	High Speed Impulsive
ICAO	International Civil Aviation Organization
LAA	Lighthill's Acoustic Analogy

LEE	Linearised Euler Equations
LES	Large Eddy Simulation
NS	Navier-Stokes
OASPL	Overall Sound Pressure Levels
PIV	Particle Image Velocimetry
RANS	Reynolds Averaged Navier-Stokes
RET	Retarded Time formulation
RF	Reference Frame
SPL	Sound Pressure Levels
TE	Trailing Edge
URANS	Unsteady Reynolds Averaged Navier-Stokes
V/STOL	Vertical/Short Take-Off Landing
WT	Wind Tunnel

Roman Symbols

$(1 - M_r)$	Doppler factor
$\Box^2$	wave operator,$\Box^2 = \frac{1}{c_o^2}\frac{\partial^2}{\partial t^2} - \nabla^2$
$\hat{\mathbf{n}}$	unit normal vector, components $\hat{n_i}$
$\hat{\mathbf{r}}$	unit vector in the radiation direction $\mathbf{r}/r$, components $\hat{r_i}$
$\mathrm{d}S$	element of source surface area
$\mathbf{M}$	local Mach number vector, components M_i
$\mathbf{r}$	vector observer and source $\mathbf{x} - \mathbf{y}$
$f(\mathbf{x}, t) = 0$	function describing the source surface, e.g. rotor blade etc.
$F(\mathbf{x}, t, \mathbf{y})$	$F(\mathbf{x}, t, \mathbf{y}) = f(\mathbf{y}, \tau = t - \frac{r}{c})$
G	Green's function
g	$= \tau - t + \frac{r}{c}$
$H(\cdot)$, $h(\cdot)$	Heaviside function
L_τ	differential operator defined as $\frac{\partial}{\partial \tau} - \frac{\partial \eta}{\partial \tau} \cdot \nabla_\eta$
M_c	aerofoil critical Mach number

M_n	source Mach number along surface normal direction, $M_i\hat{n}_i$
M_r	source Mach number in radiation direction, $M_i\hat{r}_i$
M_T	Blade Tip Mach number
p	pressure $[Pa]$
p'	acoustic pressure $p - p_0$
R	radius, e.g. rotor radius
t	observer time
T_{ij}	Lighthill's stress tensor: $T_{ij} = (\rho v_i v_j + p_{ij} - c_o^2(\rho - \rho_0)\delta_{ij})$
v and u	velocity $[m/s]$
He	Helmholtz number $He = \frac{\Omega L}{c_0}$

Greek Symbols

$\delta(\cdot)$	Dirac delta function
δ_{ij}	Kronecker delta
Γ	element of length of the Γ curve (intersection of collapsing sphere and $f = 0$)
Λ	$\sqrt{1 - 2M_n \cos\theta + {M_n}^2}$
ρ	density $[kg/m^3]$
ρ'	$\rho - \rho_0$
Σ	Emission Surface
τ	retarded time or emission time
τ_{ij}	viscous stress tensor: $\tau_{ij} = \mu\left(\frac{\partial v_i}{\partial x_j} + \frac{\partial v_j}{\partial x_i}\right) - \frac{2}{3}\mu\frac{\partial v_k}{\partial x_k}\delta_{ij}$
θ	angle between normal direction $\hat{\mathbf{n}}$ and radiation direction $\hat{\mathbf{r}}$
dΣ	element of emission surface area

Subscripts

0,∞	properties of quiescent medium
FL	transfer from Flapping frame to Lead-Lagging frame
GM	transfer from Ground frame to Moving frame
LB	transfer from Lead-Lagging frame to Blade frame

MR	transfer from Moving frame to Rotating frame
Ob	observer vectors
OG	transfer from Observer frame to Ground frame
r	quantities projected along the radiation direction
RF	transfer from Rotating frame to Flapping frame
ret	quantity evaluated at the retarded time $\tau = t - r/c$

Chapter 1

Introduction

Aeroacoustics is a research field of growing interest and is becoming even more important since the preservation of the environment is currently one of the principal issues for mankind. Environment pollution in fact comprises both air and noise pollution mainly generated by transport vehicles, cars, ships, airborne vehicles, etc. In parallel with the efforts of lowering the CO_2 emissions, noise reduction is a research challenge which attracts increasing research investments and concerns any type of vehicle, from cars to airplanes and helicopters.

With the progress achieved in aerospace technology the air transportation is used much more frequently than in the past, thus requesting higher safety levels, lower emissions and noise reduction. Both airplanes and helicopters fulfill the human desire to fly, but they have quite different physical characteristics. Fixed-wing aircrafts, also called airplane, may have faster cruise speed, higher operation altitude, longer operation distance, and larger capacity, but they also require large spaces for take-off and landing operations. Hence, airports are commonly build far away from the cities. This arises the need for commuting to and from the airport which can add much time to the trip and increase the traffic, already a big problem for some cities.

The general public has great expectations for helicopters to provide more convenient inter-city transportation since this kind of vehicle is capable of taking off and landing in very small spaces with added capabilities of very low speed flying and hovering. Besides simple transport, many life saving operations are suited for helicopters, such as heli-ambulances, law enforcement, fire-guard. For instance, operations like medical evacuation or crime monitoring are very important for the community and can be carried out only by helicopters. Furthermore this vehicle can often perform

take-off and landing operations in a constrained space making it the best choice for rescue mission in mountainous regions or even in deep-sea thanks to its hovering capabilities.

In this context noise reduction is even more necessary for helicopters in order to be able to operate closer to populated areas and in any possible hour. With the aim of meeting these requirements the regulatory bodies are imposing more severe criteria and regulations, challenging helicopters' manufacturers to resolve the annoying noise emission problem. For example, new laws and regulations such as ICAO annex16 chap8, and FAR36 App H impose more stringent limits for noise pollution of helicopters. These restrictions have severely limited the deployment of helicopters in the metropolitan area and the development of the commercial helicopter industry.

A great deal of effort has been devoted to research in the last few decades in order to reduce helicopter noise on the surrounding environment. Helicopter noise is usually categorized into three major sources:

Engine noise Since the introduction of turbo-shaft engine replacing the old piston engines, this is no longer the dominant source of helicopter noise during flyover and descent. During these phases the main and tail rotors are the primary helicopter sources of noise. Engine noise is still dominant during take-off. It is emitted through the air intake (tonal and broadband noise from the compressor) and the exhaust nozzle (combustion noise at low frequencies and core noise at medium frequencies). Depending on the installation of the helicopter, air intake noise or exhaust noise can be dominant.

Drive train noise This noise can be reduced via improved mechanical design of the gearbox and much progress has been made since the early gearbox designs. This source now affects mainly the cabin environment.

Rotor generated noise This type of noise is still a problem which needs to be resolved and it is now on the top of the list for helicopter noise research.

1.1 Rotor Generated Noise

Among the various sources of noise which can be identified in a helicopter, the most recognisable and characteristic one is its main rotor. The rotor is responsible for the main part of the perceived noise during the helicopter's flight in urban areas.

In this section, the main steps towards the current status of helicopter's rotor noise research are described.

1.1.1 Early studies

Research on helicopter rotor generated noise began in the late 1930s but the studies focused on propeller noise since, at that time, helicopter technology was in its infancy and the rotor mechanics had many similarity with a propeller. Researchers were able to identify two major noise sources for the propeller: *Thickness noise*, due to the displacement of the fluid in the flow field by the blade thickness, and *Loading noise*, caused by the accelerating force on the fluid generated by the moving blade surface.

Demming and Ernsthausen contributed together to the development of the theory for thickness noise [1, 2] while Gutin developed the theory for loading noise [3]. Later, in the early 1950s, Garrick and Watkins [4] extended Gutin's work by replacing the normal-pressure distribution over the propeller by a distribution of acoustic pressure doublet acting on the propeller subject to uniform rectilinear motion for a rotating propeller in forward flight. This established the fundamentals of the methodology for rotor noise prediction.

With the increasing popularity of helicopters, engineers opted for a more complicated design of the rotor mechanism and blade shape, adding many hinges and hence degrees of freedom in order to improve the flight comfort. This meant that helicopter's rotors could not be anymore considered similar to propellers, so that the acoustic theory developed previously and based on this assumption became less accurate and unable to capture the complex fluid mechanics of helicopter rotors. Lowson [5] and Wright [6] were the first to attempt the noise prediction for a real helicopter's rotor and Lowson and Ollerhead [7] also developed a computer code capable of predicting rotor noise.

In 1952 Lighthill developed the Acoustic Analogy,[8]-[10], on which relies a large part of the modern aeroacoustics theory. In 1969, starting from Lighthill's idea, Ffowcs Williams and Hawkings published their classic paper on sound generation by solid surfaces and turbulence, [11]. The paper generalises the theory introduced by Lighthill's to include very general types of surfaces and motions. The brilliant idea of the paper was to exploit the advance mathematic theory of generalised functions. Using this powerful mathematical tool the two researchers obtained the integral solution of the inhomogeneous wave equation known as the Ffowcs Williams-

Hawkings (FW-H) equation.

Based on Ffowcs Williams - Hawkings findings many researchers began their own theoretical work on helicopter rotor noise prediction and modelling in the 1970s. Hawkings and Lowson [12] and Farassat were among the first researchers applying the FW-H equation to rotor noise prediction. Farassat developed his Formulations 1 [13] and 1A of the FW-H equation in retarded time which have been widely used in computational prediction tools for rotor noise.

1.1.2 Recent research programmes

The 80s and 90s were decades of very intense research both in USA and in Europe. NASA together with the major U.S. helicopter companies organized the NASA/AHS Rotorcraft Noise Reduction Program,[14]. During mid 90s a collaboration between USA and Europe began in the HART (Higher-harmonic Aeroacoustics Rotor Test) project, [15], in which the newly build German Dutch Windtunnel (DNW) was exploited to perform aerodynamics and aeroacoustics tests on a scaled model of the BO-105 main rotor in the open-jet anechoic test section. In this first HART program, extensive measurements of aerodynamics and acoustics, blade deformations as well as some limited rotor wake measurements clarified the understanding of the physical mechanism involved in rotor noise generation.

In the same period some European research projects were established with the aim to assist the development of computational aerodynamics and noise prediction tools. In particular the HELINOISE research programme, [16], formed a cooperative research effort involving some European manufacturers, research establishments and universities. It was run in parallel with the HART project in the DNW windtunnel exploiting the same BO105 model rotor. The primary objective of this experimental study was to generate an extensive aerodynamic and acoustic data base for code validation and as a further objective to obtain initial detailed information on blade-tip vortex trajectories and blade positions during Blade-Vortex Interactions (BVI).

HELINOISE was shortly followed by the European cooperation research project Helishape, [17]. This was essentially a parametric windtunnel test study, in the DNW, on a scaled model of a fully articulated Eurocopter rotor equipped with blades of advanced design and two exchangeable blade tips, a more modern and complex rotor compared to the one analysed in the Helinoise tests. The aims of the Helishape project were the evaluation of noise reduction techniques, the identification of low

BVI noise descent procedures and also the generation of a database for computational noise prediction tools validation. Both HELINOISE and HELISHAPE offered great improvements to the computational noise prediction and the understanding of the physics involved in the BVI phenomena.

In the end of the 1990s European rotorcraft industries and researchers realised the need to have common computational tools for both aerodynamics and aeroacoustics calculations. With this objective under consideration, two projects, EROS and ROSAA were launched. The former, [18], had the purpose to provide the European partners with a common CFD Euler solver capable of analysing the 3-D rotor flow environment and capture rotational phenomena and correctly predict unsteady blade pressures over a range of different flight conditions, from hover to high speed forward flight. The latter, the ROSAA project, [19], was aimed at including advanced aeromechanics in rotorcraft simulation systems together with aerodynamics and aeroacoustics.

In the same framework programme, BRITE/EURAM III "Industrials and Materials Technologies", together with the two aforementioned projects was launched also the HELIFLOW project, [20], aiming to improve experimental and theoretical tools for helicopter aeromechanic and aeroacoustic interactions. In particular it was one of the first projects focused on Main/Tail rotors interactions and on the effects of Main rotor fuselage interactions.

More recently another collaboration between US and some European countries led to HART II , [21]. This project was established in order to improve the basic understanding and the analytical modelling capabilities of rotor BVI noise applying the latest experimental techniques such as 3D Particle Image Velocimetry (PIV) measurements. Given the great progress achieved in the knowledge and understanding of main rotor noise and the necessity of further investigating the problem of Tail rotor noise, some researchers launched the European project HELINOVI, [22]. This project, which has been completed in 2006, had the aim to investigate more in detail the potential of tail-rotor noise and helicopter vibration reduction.

Currently two projects on helicopter research are still running within the 6th European Framework Programme: the GOAHEAD project and the Friendcopter project. The former is focused on the aerodynamic analysis of complete helicopter configurations with the purpose to enhance the aerodynamics prediction capabilities of Europe's helicopter industry. This will be achieved via experimental campaigns in order to create a database which will be then used for validation of 3D CFD un-

steady viscous URANS solvers on complete helicopter configurations. The European project Friendcopter was launched in 2004. It is a wide scope project which does not focus only on rotor generated noise but tries to address also cabin, engine noise and NO_x emissions, as will be discussed in more detail in the following section.

1.2 Friendcopter: Parent Project of this Research

The research presented in this Thesis is carried out as part of the European project Friendcopter, titled 'Integration of technologies in support of a passenger and environmentally friendly helicopter', under the European Union 6th Framework Programme for Research and Technological Development. The Friendcopter project, [23], is a collaborative European project in which are involved the most experienced European companies, research institutes and academic institutions in the field of helicopter design. The total number of participating partners is 34, among these are present four national research establishments NLR, DLR ,ONERA, CIRA, helicopters manufacturers such as EUROCOPTER, AGUSTA and universities such as Cranfield, Roma Tre, Politecnico di Milano.

The participating partners realised that helicopters needed to be improved further with respect to environmental and public acceptance. The aim of the project is to obtain environment friendly helicopters addressing the problems of external noise, cabin noise and vibrations and the NO_x emissions. The partners have envisaged in particular the following goals:

- Acoustic footprint areas reduced between 30% to 50% depending on the flight condition
- A reduction to fuel consumption up to 6% for high speed flights.
- Cabin noise levels below 75dBA similar to airliner cabins for normal cruise flight
- Cabin vibrations below $0,05$ g corresponding to jet smooth ride comfort for the same flight regime

Because of the large and fast rotating rotor, the non-symmetric rotor flow, the close vicinity of main gearbox and passenger position and the specific requests of engine performance, the proposed goals are highly challenging. In order to comply with

the aforementioned targets, an extreme high tech initiative is required and this can be done only by completion of specific short and long term objectives: Short term goals include:

- reduction of cabin and engine noise using noise absorbing structures and active structures control.
- noise abatement flight procedures

The engine noise emission will be tackled by acoustically treating the engine inlet and outlet ducts with noise absorbing structures. The reduction of the cabin noise level will be addressed by tackling cabin noise emission at the source via a modification of the gearbox elements and use of active elements to interrupt the interfaces between gearbox and fuselage. Furthermore the cabin structure will be acoustically treated. It is possible to significantly reduce annoyance of both new and already fielded helicopters by using adequate low noise flight procedures in the vicinity of sensitive areas. In particular the research presented during this thesis falls inside the noise abatement flight procedure short term goal. Long term goals include:

- lowering of impulsive exterior noise
- lowering excessive cabin vibrations
- lowering high fuel consumption

The long term goals will be obtained via an advanced blade design including full Active blade control.

1.2.1 Noise abatement flight procedures

The helicopter noise emission intensity and directivity heavily depend on flight conditions such as: airspeed, rate of climb/descent, acceleration, manoeuvres. Consequently, a noise reduction strategy can be based on some carefully chosen pilot actions. For instance, the level of noise affecting a sensitive ground populated area is inversely proportional to the distance from the area. The noise emission reaching this area can be minimised by choosing a flight path in order to increase the distance of the helicopter relative to the populated area and expose it only in the directions

where noise radiation is minimal. Alternatively careful control of the power settings at take-off and climb-out can be achieved, in order to reduce the engine noise.

Definition of such noise abatement procedures is the first step and it will be accomplished via the use of an optimization suit of software, called HELENA, produced within the Friendcopter framework, which will rely on experimental and numerical databases. As a short term goal of external noise reduction, the impulsive noise due to BVI during the specifically sensitive approach operation will be tackled by dedicated flight procedures taking into account also aspects of safety and certification. The goal is to identify a combination of glide path angle and flight speed to circumvent the area of high blade slap. Noise prediction codes, such the one that will be presented in this thesis, will be used for noise footprint prediction and will be included in the HELENA software in order to explore the optimum flight path choices for a given helicopter configuration.

1.3 Trends in Open Rotors Research

Lower noise emissions and fuel consumption issues are not the only concerns affecting rotorcraft research. In the rotorcraft industries, including helicopters and Vertical/Short Take-Off Landing(V/STOL) aircrafts, a problem has been identified which limits helicopters competitiveness towards airplanes. In fact helicopters fly at lower cruise speed compared to those that fixed wing aircrafts are capable to achieve. The top cruise speeds of helicopters in service today, roughly 150 to 170 knots, are only incrementally better than what they were decades ago due to the fundamental limits of conventional rotor systems. Traditional helicopters suffer from the effect known as retreating blade stall, which is the main limiting constraint acting to the top speed.

In forward flight, as opposed to hover, the main rotor blades are subject to a strong flow asymmetry. The blades rotate towards the incoming airflow on one side the helicopter, which is commonly called advancing side, while on the other side the blades rotate following the airflows direction. This side is named retreating side. The retreating blades experience slower incoming airflow since the relative velocities of the blades and airflow subtract. This results in a reduction of the lift on the retreating side, while on the advancing side, the increased relative velocity enhances the lift. The lift imbalance across the rotor disk was identified since the early helicopters developments and it was alleviated by the introduction of flapping hinges

in the rotor hub. The blades flapping produces a variation in the angle of attack, which is increased in the retreating side and decreased in the advancing side. This flapping induced variation compensates the lift asymmetry which affect the rotor.

However, as the helicopters forward velocity increases, there exists a limit to the degree by which dissymmetry of lift can be diminished by this means. Since the forward speed is important in the phenomenon, this imposes an upper speed limit upon the helicopter in order to prevent the condition known as retreating blade stall. This upper speed limit is called "Velocity Never-Exceeded", and as discussed above it ranges from 150 to 200 knots for the modern helicopters. Research efforts towards the defeat of these limitations began in 1976 when a ten-years collaboration in aerodynamic research was established between Westland Helicopters and the Royal Aircraft Establishment. As a result the so called BERP blade was obtained. The Lynx helicopter, a Westland demonstrator equipped with this particular blade design, attained the world absolute speed record for any helicopter, still in place more than ten years later. The Lynx achieved an average speed of $249.1mph$ (almost 220 knots) over a $15km$ course, thanks to the BERP blade peculiar design. Given its success this technology is now being applied to other helicopters.

More recently two main research trends are being investigated to further increase the flight speed and the helicopter competitiveness towards airplanes. Some industries such as BELL and AGUSTA are collaborating towards the finalisation of the tiltrotor idea for the future V/STOL aircraft, the V22 Osprey, [24], which is currently being flight tested (the military version, started in early 90s is in a more advanced status than the civil one). This is a hybrid type of rotorcraft which has V/TOL capabilities and can then rotate its wings by $90°$ so to behave like a traditional airplane in forward flight conditions.

The Osprey configuration can reach cruise speeds of up to 250 knots but has some drawbacks with respect to traditional helicopters. The necessity to rotate its wings in order to operate in hover conditions leads to a degraded hover performance for this craft and a much higher cost of up to $4-5$ times that of a traditional helicopter,[25]. Since the helicopters' hover capability is one of the most exploited characteristics of these particular class of airborne vehicles some other industries, such as Sikorsky, have planned a different design concept to solve the low cruise speed issue without penalising the important hover performances.

The Sikorsky concept named X2, and announced in the end of 2005, [26],will have 2 coaxial counter rotating main rotors which are supposed to alleviate the lift dis-

symmetry allowing cruise speed in the range of 250 knots and above. The forward thrust component will be provided by an aft propeller. The X2 configuration will then have the same hover capabilities as the conventional helicopters and speeds that are not reachable with the current helicopter configurations.

1.3.1 Open rotors in aircrafts

Open rotors technology, currently exploited in rotorcrafts and Wind Turbines, had its first applications during the early developments of aircrafts. In that period propeller engines were the only mean of producing the required thrust. During the 50's, for commercial flights, this technology was abandoned in favour of the most promising turbojet engines which were capable of producing much higher thrust, and thus increasing the cruise speeds and decreasing the flight duration. The drawback of turbojet engines was their law efficiency and the high noise levels that they were generating. Since the 60's these problems were addressed with the introduction of Turbofans which had initially Low Bypass-Ratios(BR). This feature of turbofan engines, on which depends their high efficiency and low noise characteristics has been steadily improved resulting in the modern High BR Turbofans.

The current aircraft engines, given the High BR of $6 - 8$, in fact generate much lower noise emissions compared with the initial turbojet engines and also have higher efficiencies. However a further increase in BR ratios, in order to reduce CO_2 and NO_x emissions, is technically not achievable. Some manufacturers, [27], are looking at a different technology, a propulsion system for aircrafts which was designed and investigated during the mid 70's and 80's, know as Propfan.

The Propfan engine could be considered as fusion of the propeller and turbojet technology. Its main characteristic is the high efficiency due to the ultra high BR of over 15, obtainable with this design. Since 1988 it was assumed that such design could bring a reduction in fuel consumption of 15% to 35%, [28], compared to the turbofan engines available at that time. A recent revision of these figures by Birch, [29], showed that a possible reduction of $10 - 15\%$ of fuel consumption, and as a consequence to the CO_2 emissions, is achievable with respect to the current turbofan consumption.

Various versions of the propfan, with different number of blades and blade shapes, have been designed and tested in wind tunnels in order to find an optimum in efficiency. General Electric in USA designed also the counter rotating UnDucted

propFan (UDF). Since the 90's the actual pace of developments on propfan technology has been practically at a stand still. According to Schimming, [30], only few technical programmes for designing UDFs in terms of aeroacoustics, aerodynamics and aeroelasticity are still ongoing in different countries. On the contrary, the trends envisaged by Kehayas, [31] and Garcia, [27] show that the propfan technology, in particular UDFs could be the answer to the future demands of higher efficiency aircraft propulsion.

From the technical point of view, in order to allow a wide diffusion of this technology, two problems need to be addressed: cabin noise and blade containment requirements, [31]. However some industries, such as CFM, a 50/50 joint company between Snecma (SAFRAN Group) and General Electric Company, have already announced in 2007 their plans to investigate this efficient mean of propulsion further, for a future version of the LEAP56 engine.

1.4 Problem Statement

From the arguments above the increasing importance of the use of noise prediction is clear during the design process in modern aerospace industries. Both theoretical and experimental studies are being conducted to obtain such predictions. Flight or wind-tunnel tests have been widely exploited in the past and many current research investigations are based on them given the accuracy achievable in modern experimental campaigns. However,these tests have a major drawback, the high costs involved.

For instance an acoustic test on a scale model helicopter in a Wind Tunnel (WT) costs around 200k Euro per week without taking into account the design and production costs of the WT model. In-flight aeroacoustics experiments are even more expensive given the needs to insure the pilots and the larger number of microphones and equipments required. Currently, numerical aeroacoustic analysis tools represent a valid alternative for the prediction and control of aerodynamically generated noise, given the rapidly increasing computational power and the increased accuracy and reliability of CFD prediction.

Thus, the development of improved computational noise prediction tools constitutes a very important part in the quest for future environment friendly and high speed airborne vehicles. Given the aforementioned trends for future open rotors

applications, a computational noise prediction tool must be capable of dealing with subsonic, transonic and supersonic flight conditions for rotating noise sources, but the same tool could be easily extended to other more general external noise applications.

These are the main reasons which lay behind the research presented in this thesis. Furthermore the research has the purpose to make a direct contribution to tasks of the Friendcopter project, described in Par. 1.2.1.

1.5 Thesis Structure

The thesis outline is as follows:

- In the first Chapter is presented an introduction on helicopter's rotor noise research and some future trends for open rotors applications followed by the research problem statement and thesis outline.
- Chapter 2 presents the research design, scope and methodology. The research aim and objectives are also stated in this Chapter.
- The Third Chapter describes the physics of rotor noise generation identifying the main sources which contribute to the overall noise. This discussion is then followed by a description of the current approaches and state of the art in aeroacoustics prediction.
- The numerical approaches developed during the course of this research are discussed in Chapter 4. Here a detailed description is presented for both the novel root finder algorithm and the Emission Surface construction approach that have been developed in this study.
- In Chapter 5, the test cases used for Verification and Validation are presented. First the root finder algorithm is applied to the solution of the retarded time equation in subsonic and supersonic conditions. The efficiency of the algorithm is compared to the classical methods used in aeroacoustic codes. The noise prediction tool is then applied to the analysis of $3D$ monopole dipole and quadrupole sources for which are available analytical solutions. Finally the tool is tested for the calculations of the emission surfaces of three different geometries which are rotating in transonic/supersonic motion.

- In Chapter 6 the code is applied to test cases in both subsonic and supersonic regime. The test cases have been chosen to match two renowned experimental campaigns: in subsonic regime the Helishape experiments, [17], for BVI noise are analysed; since in supersonic conditions HSI noise is the most important source, the experimental campaign from Purcell, [32] is chosen. This is a wind-tunnel experimental study on the $UH1H$ rotor blade in delocalised conditions.

- Finally in Chapter 7 are drawn the conclusions and recommendations for future investigations.

Chapter 2

Research Design

In this Chapter the research aim and objectives are stated. Then, the research scope and methodology adopted in order to carry out the current research are discussed.

2.1 Research Aim

The first aim of this research is to explore the field of computational aeroacoustics prediction applied to rotor generated noise, and secondly to develop a computational noise prediction algorithm capable of dealing with noise sources in both subsonic and transonic/supersonic regimes. The motivation for this work is that many noise prediction algorithms are available for subsonic cases, while only 2 strategies have been developed for dealing with transonic and supersonic sources but are not efficient for the analysis of sources in subsonic regime.

2.2 Research Objectives

The following objectives have been identified for the fulfilment of the proposed research:

- to carry out a literature survey in order to identify the current state of the art in noise prediction algorithms for external noise applications,
- to develop a computational prediction tool based on the state of the art algorithms identified in the literature survey,

- to create a novel algorithm for transonic and supersonic sources and to implement it in the noise prediction tool,
- to identify specific verification and validation cases for both subsonic and transonic/supersonic regimes,
- to validate the noise prediction tool for the selected cases.

2.3 Research Scope

Based on the research objectives mentioned above, the scope of this research can be summarised as follows:

Domain: This research focuses only on aeroacoustic analysis of external noise from stationary and rotating sources, such as helicopter rotor and open rotors. Both noise generation and propagation are discussed. The analysis does not include full helicopter configuration with fuselage and tail rotor. The main research domain comprises hybrid approaches for aeroacoustic predictions with particular focus on methods based on the FW-H equation. Although CFD calculations have been executed successfully for some of the case studies which will be presented in the next chapters, the primary objective of this study is the development of algorithms to be exploited during the propagation phase of the hybrid approaches.
Noise prediction techniques: This research considers only algorithms based on the integral form of the FW-H equation exploring the use of both "Retarded Time" and "Emission Surface" formulations. These are the most promising techniques for the particular analysis on which this study is focused.
Literature Survey: The literature survey of the current research covers the principles of helicopter rotor noise and the sources which are responsible for the overall generated noise. Furthermore, a review of the available noise prediction methods is presented with particular emphasis on those used for the aeroacoustic analysis of helicopter's main rotor. The review is divided in methods which can be used in subsonic flow conditions and methods more appropriate for supersonic regimes.
Test Cases: The test cases included in this thesis have been chosen to represent the most important noise sources for helicopter rotor noise, Blade Vortex Interaction and High Speed Impulsive noise. The former is considered here only during subsonic flow conditions, while the latter is typical of transonic and supersonic sources. Thickness and Loading noise are also included since they are an intrinsic part of rotor noise sources.

Verification and Validation: These processes will be performed via the classical approach in CFD research. The software developed during the current research will be tested on cases for which analytical or computational results are available in literature. Then, the prediction tool is applied to the analysis of the aforementioned test cases and its results are compared against the experimental data available in literature.

2.4 Methodology

During this research a set of algorithms were developed and tested for their efficiency and capabilities of handling sources in both subsonic and supersonic regimes. The current state of the art for helicopter rotor noise prediction is analysed through a literature based investigation which highlights the scarce availability of aeroacoustic prediction tools and algorithms for treating sources moving in transonic and supersonic conditions. In addition, the literature survey shows the lack of research studies on the behaviour of the retarded time equation for $M_r \geq 1$ when the appearance of multiple roots does not allow the use of classical root finder algorithms.

This is followed by the development of an algorithmic framework which will implement the state of the art methods for helicopter rotor noise prediction as the starting point. In this way, all the strengths of the current status of noise prediction research are inherited, while during the development the weaknesses will be addressed. The process will be based on the hypothesis that the noise prediction tool will handle moving and rotating sources in subsonic as well as supersonic conditions. The development is carried out in a systematic, step-by-step fashion, i.e. every feature is tested after implementation before a new feature is added.

Since the noise prediction tool is based on three main components, i.e. quadrature algorithm, root finder algorithm, kinematics and Emission Surface (ES) construction, the verification and validation processes are applied to each one of its components. More precisely, the available analytical solutions for $3D$ monopole, dipole and quadrupole sources are used to test the quadratures. The root finder algorithm used to solve the retarded time equation for a rotating point source, represented by a panel, both in subsonic and supersonic regimes and its computational time and efficiency are compared against the two classical root finder methods, Newton and Brent's scheme and the "Advanced Time" solution.

Finally the kinematic and ES construction modules are applied to the computation of the ES for some geometries which emission surfaces have been presented in literature. Once the verification and validation processes are completed, the hypothesis is tested by applying the noise prediction tool to test cases typical of helicopter rotor noise. The literature survey assists to the definition and identification of rotor noise sources, and the test cases will comprise those sources, i.e. BVI and HSI, which, as described in literature, contribute more to the overall rotor generated noise. The results obtained are compared to the experimental analyses, available in literature and upon which the test cases are built.

Chapter 3

Literature Review

In order to better understand the mechanisms involved in rotor noise generation, the physical phenomena which govern the complex noise source will be described in the first section of this chapter. This is then followed by a detailed discussion on the current approaches available for aeroacoustics prediction and in particular the FW-H equation. Many different formulations based on this equation have been defined. In the last part of this Chapter those formulations which constitute the current state of the art in rotor noise prediction will be described, with a more detailed description of those which have been implemented in the noise prediction tool developed during this research.

3.1 Rotor Generated Noise: Physics

Rotor generated noise can be considered as the noise generated by both the helicopter's main and tail rotors. These two sources operate in different frequencies range, the main rotor noise dominates the lower frequencies and the tail rotor noise dominates the mid frequency range. This research focuses only on the main rotor generated noise.

A helicopter in operation can be easily recognised by the harshness and periodicity of its noise. The sharp and loud periodic sounds emitted are known as Impulsive noise. Together with the so called rotational noise, which has similar characteristics to the impulsive noise but milder amplitude, constitute the discrete frequency component of the main rotor noise. The other part of the frequencies spectrum is dominated by the broadband noise sources.

The sources that produce the overall rotor noise can be divided into deterministic and non deterministic. Thickness, Loading, BVI and High Speed Impulsive (HSI) noise belong to the deterministic sources, while broadband noise belongs to non-deterministic sources. Thickness and Loading noise are also known together as Rotational noise and are related to linear aerodynamic theory. HSI and BVI are related to non-linear aerodynamic effects and these two types of Impulsive noise are very important since they dominate the noise signal when they occur. Impulsive noise is in fact the most annoying rotor generated noise. The non-deterministic noise, Broadband noise, is generally classified in three different sources: Blade Self-Noise, Blade Wake Interaction (BWI) noise and Turbulence Ingestion Noise.

Each one of the sources introduced above will be now described in more detail.

3.1.1 Thickness noise

Thickness noise is generated due to the fluid displacement created by the rotor blade thickness. It is governed by the rotor speed and airfoil thickness distribution, [33]. Thickness noise propagates primarily along the rotor disk plane in front of the rotor. The main contribution to thickness noise arises from the blade tip region, where high rotational speed is recorded. Thickness noise is characterized by a symmetric negative pulse shape in the acoustic pressure, both in hover conditions and in forward flight. It was the first rotating noise source to be studied, [1, 2] and, since it only depends on the geometry and kinematics of the rotor blades, the computation of this rotor noise source does not require to perform any flow measurements or predictions. These characteristics made it possible to compute thickness noise since the early studies and Farassat exploited for the first time an algorithm based on the FW-H equation in 1979, [13, 34].

3.1.2 Loading noise

This term usually refers to the harmonic noise from non-impulsive loading sources. Loading noise is caused by both steady and unsteady force distributions on the fluid generated by moving blade surface. The loading noise propagation direction is usually concentrated below the rotor disk. Loading noise generally radiates as a dipole pattern with a maximum along the rotor axis of rotation.

Loading noise becomes the dominant source of rotor noise in the absence of impulsive

noises. Due to its magnitude and since it radiates below the rotor disks loading noise has been a major concern for helicopter civil operation. Loading noise was also studied, like Thickness noise, since the early stages of open rotors noise research, in propellers by Gutin, [3] and Garrick et al., [4], and in helicopter rotors by Wright,[6] and Lowson and Ollerand, [7]. This noise source depends on the blade pressure distribution and hence in order to obtain a noise prediction it is necessary to know the pressure distribution along the blade. This can be done using experimental data, as it was common practice,[35], when CFD predictions could not be accurate because of the lack of computational power, or using the accurate CFD prediction codes available today.

3.1.3 High Speed Impulsive noise

The thickness noise described above is influenced only by linear effects, when the blade tip Mach numbers are well below $M_T = 0.85$, [33]. Instead, when the forward flight speed increases, the non-linear effects play an important role. As M_T approaches 0.9 the compressibility effects make the negative pulse to increase dramatically in amplitude and a further increase in M_T produces also a change in shape, i.e. the symmetric shape that is characteristic of the thickness noise becomes asymmetric. In this condition of high-speed forward flight, HSI dominates the waveform spectrum. HSI is generated by nonlinear effects, appearance of compressibility and shock delocalisation.

Shock delocalisation is a phenomenon that arises when, due to the increase in M_T, the localised shock and supersonic flow bubble, close to the advancing blade tip, reach the so called sonic cylinder. This virtually divides the subsonic and supersonic flow around the rotor. When the aforementioned phenomenon happens, the shocks over the blades are able to radiate in the acoustic far-field, intensifying the acoustic pressure disturbance perceived by the observer. This means that, when shock delocalization occurs, this source will dominate the overall perceived noise. HSI noise usually propagates along the rotor disk plane in a direction similar to thickness noise, so that it was considered as part of the thickness noise. In early studies, this phenomenon was in fact considered as transonic thickness noise, [36, 12], but soon after, researchers identified the importance of the non linear terms, represented by the quadrupole term in the FW-H equation, which are the main factor in HSI noise radiation.

The prediction of HSI noise requires the use of unsteady compressible Computational

Fluid Dynamics (CFD) codes in order to obtain the shock and transonic flow fields. Some very interesting experimental campaigns, in order to measure HSI noise, have been performed by Boxwell et al. [37] and the first computational studies for HSI noise evaluation in helicopters were proposed by Purcell, [32] and Baeder, [38].

Given the importance of the quadrupole term in the propagation of this noise source, Farassat, [39, 40], Brentner and Holland, [41], introduced the far-field approximation method for the quadrupole term. This technique was aiming to reduce the computational time necessary to calculate the contribution to noise generation from this term, using a surface integral instead of the more time consuming volume integral. Most of the later studies exploited this simplification in order to perform faster noise predictions, but almost all of the computations published were performed in retarded time formulations. The use of this formulation limited the analyses to high subsonic regimes because the Doppler singularity, $1 - M_r$ at the denominator of retarded time integrands, does not allow to consider transonic conditions where the shock delocalization, and hence HSI noise, is stronger. The only studies exploiting different formulations, not affected by the Doppler singularity, were the pioneering works of Farassat [42, 43] and more recently, Brentner, [44], Ianniello, [45]-[48] and Prieur et al., [49], as will be discussed in the next section.

3.1.4 Blade-Vortex Interaction noise

Blade-Vortex Interaction noise is generated by the tip vortices shed from one blade and interacting with the following blades. A very rapid fluctuation in the aerodynamic forces, particularly strong in the tip region, is produced over the blade interacting with the incoming vortices generating BVI noise. This phenomenon, when it occurs, is an extremely annoying noise source. Usually it arises during specific types of operations such as descent flight with low forward speed. Unlike HSI noise, which propagates mostly in the plane of the rotor, BVI noise radiates usually forward and down at about a $30° - 40°$ angle. This radiation pattern makes the noise more audible to observers on the ground as the helicopter is landing.

Extensive research has been carried out, both experimental and computational in order to understand the physics of BVI noise. The studies highlighted how the magnitude of BVI noise depends on the tip vortices strength, the core size of the vortices, the interaction angles and vertical separation between the vortices and the blade, labelled as miss distance. Experimental studies of BVI noise began with the work of Leverton and Taylor [50] when community annoyance and aircraft detection

were initially considered. Some flight testings were also performed, delivered by Schmitz and Boxwell [51, 52] specifically to study BVI.

The use of an independently generated vortex referred to as "freevortex" was introduced in the experimental studies by Horner et al.,[53] and Kitaplioglu and Caradonna et al. [54]. The free vortex provides a better control on the aforementioned BVI parameters, enabling a more detailed study of the individual parameters which influence the blade load distribution, and hence the resulting acoustic pressure reaching the observer.

The analytical and computational studies of BVI phenomena were pioneered by Widnall in the 70's, [55], and it was proved that the parallel BVI generates the strongest pulse among all BVI conditions. In the late 80's Baeder and Srinivasan [56], performed a computational study of the BVI experiments from Caradonna [54].

In the last two decades, BVI noise has been the focus of much of the helicopter noise research. In fact, many of the projects described in the first chapter, such as HART, Helinoise [16], Helishape [17] and HART II, were specifically designed to provide an aerodynamic and aeroacoustic database for BVI phenomena.

3.1.5 Broadband noise

Broadband noise, the non deterministic source of helicopter rotor noise, is essentially generated by turbulence and its interactions with the rotor blades. Some of the very first studies on broadband noise were the experimental investigation conducted by Brooks et al., [57, 58]. In [57] the researchers identified for the first time the so called Blade turbulent Wake Interaction (BWI) mechanism while in the parametric study on airfoil self-noise, [58], the same research group presented for the first time a detailed list of the different mechanisms which can generate broadband noise. In particular, the importance of the Trailing Edge (TE) was highlighted in broadband noise generation, due to vortex shedding or to the interaction between the TE and the Turbulent Boundary Layer over the blades. In [33] another broadband noise source is labelled as Turbulence Ingestion noise, that arises when some turbulent eddies in the atmosphere are "ingested" by the main rotor.

The flows around helicopter rotors are characterised by high Reynolds numbers, in the order of 10^6 and above. The importance of turbulence in Boradband noise generation would require the use of advance turbulence modelling such as Large

Eddy Simulation (LES) or even Direct Numerical Simulation. Furthermore, since most of the turbulent scales need to be solved, in this case the use of Unsteady Reynolds Averaged Navier-Stokes (URANS) would give incorrect results. Given these high computational requirements, no computational studies for the analysis of broadband noise have been performed on a full helicopter rotor configuration. In effect even with the current computational power, a fully 3D CFD analysis of an helicopter's main rotor, with the purpose of analysing broadband sources, is not yet feasible.

The few computational studies on broadband noise which have been published, such as [59, 60], consider just the simple $2D$ cases of rod-airfoil interaction noise or airfoil trailing edge scattering. In this context it is clear why mainly the current methods for broadband noise prediction are semi-empirical, [61, 62, 63], and based on the findings of Brooks et al. [58].

3.1.6 Tail Rotor Noise

During the last two decades, the physical understanding of helicopter main rotor noise and the capability to predict its noise radiation generated by various aeroacoustic source mechanisms has significantly been improved. However, research on tail rotor noise has been almost ignored for a long time. Tail rotor noise contributes to the overall helicopter noise and during certain flight conditions, e.g. at take-off, can even dominate the overall noise radiation.

Tail rotors are smaller versions of the main rotors; their plane of rotation is in vertical position and their rotational speed is much higher than that of main rotors. It is trivial to understand that the noise generated by tail rotors has the same characteristics and is composed by similar sources as the noise produced by the main rotor. The main difference with the respect to main rotor sources is the higher frequencies at which tail rotor generate noise. It must be highlighted that high frequencies are more annoying for the human ears than mid to low frequencies.

In addition, the interaction of the main rotor wake with the tail rotor could be a further source of tail rotor noise that is not necessarily periodic. The main/tail rotor interaction noise is due to the interaction of tip vortices generated by the main rotor interacting with the tail rotor. Thus, in order to predict the tail rotor noise it is necessary to compute also the aerodynamic field around the main rotor, the wake that this generates and the location of tip vortices generated from the main rotor.

The European projects Heliflow, [20], and HELINOVI, [22], were particularly focused on this kind of interaction noise, investigating also some parameters, such as Tail Rotor sense of rotation, variation of position between Main and Tail rotor and variation of rotor rotational speed, which are thought to influence the tail rotor noise generation.

3.2 Noise Prediction Approaches

Aeroacoustics and aerodynamics could be considered as two different points of view for the analysis of fluid motion, Computational Aero Acoustics (CAA) problems in fact have the same governing equations as CFD problems, namely the time-dependent, compressible Navier-Stokes (NS) equations. The difference between the two disciplines lies in the modelling of the NS equations and in the scales of interest for the flow solution.

CFD has had a great development during the last 30 years and many different models have been proposed in order to resolve the NS equation, with each model being more suitable for a particular range of Reynolds or Mach numbers. The acoustic fluctuations in an unsteady fluid flow are orders of magnitude smaller with respect to the aerodynamic fluctuations. Hence, some simplifying assumptions, such as incompressible flows, steady state flows, laminar flows, which can be used in aerodynamics are not valid in aeroacoustics. Thus CAA problems must be resolved always considering an unsteady, compressible flow and in the majority of cases also turbulent. As a consequence the computational time required in CAA is dramatically increased.

3.2.1 Direct Noise Computation

The possibility of using the so called Direct Noise Computation (DNC), which is equivalent to the Direct Numerical Simulation , is very recent. The first applications of this method can be found only from the end of 90s, by Lele et al. [64], Freund et al., [65], more recently Bogey et al. [66] and Jiang et al. [67]. In effect, the acoustical field induced by an unsteady flow can be calculated very accurately using DNC but this accuracy comes at a high computational cost because the number of grid points required for a DNC computation depend exponentially on the flow Reynolds number, eq.3.2. Thus, the currently available computational power allows only to simulate flows with relatively small Reynolds numbers. On the other hand

the engineering applications, which require noise prediction, are characterised by high Reynolds number beyond the current capability of the existing computers.

It is known that in DNS the number N^3 of spatial grid points required in order to solve the 3D isotropic turbulent flow is function of the Reynolds number, [68], as follows:

$$N^3 \geqq {Re_l}^{\frac{9}{4}} \tag{3.1}$$

in which Re_l is the turbulent Reynolds number based on the integral length scale of turbulence, l, which for isotropic turbulence is proportional to the Kolmogorov scale η as $(l/\eta \propto {Re_l}^{\frac{3}{4}})$.

Sarkar and Hussaini, [69], and more recently Bailly and Bogey,[70] , calculated the computational costs related with a DNC, i.e. a CFD simulation which must resolve not only the turbulent near-field, but also the acoustic far-field. For a jet noise calculation in the hypothesis of isotropic turbulence the number of points required in the domain discretisation can be calculated as follows.

Defining the integral length scale of turbulence as $l \sim D$, where D is the diameter of the Jet, the dominant wavelength, λ_s, of the radiated sound can be estimated as $(\lambda_s \propto l/(St * M_t))$, where M_t is the turbulent Mach number. The time step size for a DNS is $\Delta t \propto \frac{\eta}{c}$ so that the number of time steps needed for the solution of the turbulent fluctuations is $n_t \propto (l/U)/\Delta t \propto {Re_l}^{3/4}/M_t$. The total number of spatial grid points and time steps required in order to resolve both the turbulent near-field and extend the domain up to the acoustic far-field becomes:

$$\begin{aligned} {N^3}_s * n_t &\propto \frac{{Re_l}^{\frac{9}{4}}}{St * {M_t}^3} * \frac{{Re_l}^{3/4}}{M_t} \\ {N^3}_s * n_t &\propto \frac{{Re_l}^3}{(St^3 * M_t^4)} \end{aligned} \tag{3.2}$$

This means that for a subsonic turbulent flow the number of points required to solve both near and far-field is proportional to ${M_t}^{-4}$ with respect to the grid spacing needed to solve only the turbulent near-field. In other words, keeping the number of spatial grid points constant, the Reynolds number achievable decreases with a factor of ${M_t}^{4/3}$, e.g. for a $M_t = 0.01$, Re_l decreases by a factor of 0.004. Of course for higher Mach number the dominant wave length λ_s becomes smaller so a smaller extension of the domain is required in order to reach the acoustic far-field.

For a DNC computed using LES instead of DNS the cost can be obtained with similar arguments but keeping in mind that in the LES case the scales to be resolved go from the large eddies up to the Taylor microscales,l_m, while the smaller scales can are modelled. l_m for isotropic turbulence is related to the integral length scale l as $(l/l_m \propto {Re_l}^{\frac{1}{2}})$, hence the total cost for a DNC with LES would be:

$$ {N^3}_s * n_t \quad \propto \quad \frac{{Re_l}^2}{(St^3 * M_t^4)} \tag{3.3} $$

Such requirements of computational resources are certainly demanding even for small Re_l so for practical cases a DNC is not yet feasible. Some studies have, although, been attempted, particularly in Jet Noise analysis from Freund,[65] , for $Re_l = 2{*}10^3$ via DNS using $22.1 * 10^6$ grid points, and from Bogey et al., [66], via LES for $Re_l = 4 * 10^5$ and $16.6 * 10^6$ grid points.

3.2.2 Hybrid Approaches

As discussed above, DNC has the advantage of high accuracy but it is very demanding in terms of computational cost and time, hence, real engineering problems cannot yet be computed using this method. The solution of aeroacoustics problems for engineering applications can be currently obtained via the so called Hybrid Methods. In these methods the computational domain is divided into two different regions; a near-field region in which are enclosed all the source terms and a far-field domain in which the acoustic signal propagates up to the observer. This would involve using different numerical modelling for each region, such as a CFD prediction tool in the near-field region and an acoustic solver in the regions outside the near field.

The acoustic prediction tools to be used in the outer region can be grouped into two categories, integral approaches and differential approaches as follows:

- Differential Methods
  - LEE
  - APE
- Integral Methods
  - Lighthill's Acoustic Analogy
  - Kirchhoff equation

– FW-H equation

In the following subsections these methods are discussed and then particular focus is given to the approach used during this research, i.e. the FW-H equation.

3.2.2.1 Linearised Euler Equations (LEE) and Acoustic Perturbation Equations (APE)

The LEE approach was introduced initially by Tam, [71], and applied by many other researchers in jet noise prediction. The LEE method is based on two simplifying assumptions: the magnitude of acoustic fluctuations is very small compared to the aerodynamic fluctuations and viscous effects can be considered negligible with respect to the acoustic wave propagation. Under these two conditions, the original non linear system of equations, the NS equations, can be linearised obtaining the LEE equations.

These linear system of equations, although simpler with respect to the NS system, it is still a time-dependent partial differential equations system. LEE must be numerically solved exploiting high order low-dispersion and low-dissipation discrete schemes.

There have been many different forms of this approach. The initial applications were based on a one step method, i.e. the domain was computed in full, from near-field to far-field with no division between the noise generation and noise propagation phases. More recently Bailly et al., [72], introduced two steps approaches. In [72] is presented the so called Stochastic Noise Generation and Radiation (SNGR) model. Bailly et al. proposed the use of a steady RANS simulation to calculate the steady mean flow. Then the Euler equation are linearised around this mean flow and a stochastic turbulence model is used as a source term in the LEE.

In another approach, the Acoustic Perturbation Equations (APE), similar to LEE, a division between the dynamic source region and the far-field is implemented. The APE are derived by decomposition of the flow into acoustic and non-acoustic quantities, based on a filtering of the non-linear and viscous terms of the NS and continuity equations. Ewer and Schroder, [73], proposed an approach which exploited LES calculations for the generation step and the APEs to simulate wave propagation.

Careful numerical discretisation of both domain and governing equations is required in order to obtain accurate noise prediction via LEEs or APEs. This applies to both

cases, whether no distinction is made between noise generation and propagation regions or whether the domain has been divided in two parts. Tam [74], and Wells et al., [75], identified the following points which constitute some challenges for LEE methods:

- Aeroacoustics problems are intrinsically unsteady
- The frequency range involved in the solution spreads over a wide bandwidth
- Acoustic waves have small amplitudes
- The solution must be computed extending the domain up to the observer which is usually in the far field, i.e. very large domains are necessary in many cases
- The boundaries of the domain could be reached by the acoustic waves since these decay very slowly
- Aeroacoustics problems are specifically multiscale problems, i.e. the scales in the source region and in the far field can be very much different, particularly at low Mach numbers, where the acoustic length scale is proportional to the aerodynamic one with a factor of M^{-1}

In order to resolve these issues a very accurate discretisation of both domain and equations must be exploited. The separation between the flow field and the acoustic field, as proposed by Ewert et al. [73], offers a solution to the problem of the disparity of the turbulent and acoustic length scales. But for the discretisation of the differential equations governing the problem high order low-dispersion and low-dissipation discrete schemes are required, specifically studied for aeroacoustics problems, [71, 74], and complex boundary conditions.

This means that, although much smaller than the computational cost required by DNC or LES methods eqq.(3.2-3.3), the cost for the solution of the LEE is still very large and more demanding than the one required by the integral methods which will be discussed in the next section.

3.2.2.2 Integral methods

Integral methods are the less demanding in terms of computational time and resources. They are also the first methods to be considered, as some of the earliest studies were published already in late 30s,[1]. The breakthrough for the modern

aeroacoustics theory at the base of the integral methods was presented in the papers of Lighthill, [8], and Curle, [76], during 1950s and 60s. The three approaches which are exploited in the current integral methods for noise prediction are:

- Kirchhoff equation
- Lighthill's Acoustic Analogy
- FW-H equation

Since the approach implemented in this research is based on the FW-H equation, the first approach does not fall within the scope of this research. Hence, only a brief discussion of the Kirchhoff method is presented below.

Kirchhoff equation. The Kirchhoff equation was first introduced by Goldstein, [77], and then used for the first time by Farassat et al. [78]. It is based on the Kirchhoff integral theorem. The method is divided in two phases: in the first phase, the flow field inside the dynamic source region, bounded by the surface S, is obtained via CFD calculations. In the second phase, the pressure distribution on the boundary surface S and the variation of pressure along the normal direction to S, provided by the CFD analysis, are used as inputs for the linear wave equation. This propagates the acoustic pressure disturbances up to the observer position in the far-field. It is important to highlight that all the non linearities must be included inside the S surface.

This is an efficient and simple approach but it has a major drawback. The noise predictions obtained with this method are very sensitive to the positioning of the boundary surface S, which defines the extension of near-field domain. This is because it is unknown a priori whether or not the non linearities have been encapsulated within the near-field boundary. Recent works by Brentner and Farassat, [79] and again discussed in [80], have shown in fact that the Kirchhoff formulation is unreliable for aeroacoustic problems given this high sensitivity to the position of the near-field domain boundary.

In the following sections the Lighthill's Acoustic Analogy will be described, which is the base of the FW-H equation. This description will show the steps to obtain the FW-H equation from LAA and the developments which followed Ffowcs Williams - Hawkings study and brought to the current status of noise prediction methods for helicopter rotor noise.

3.2.3 Lighthill's Acoustic Analogy

The Acoustic Analogy (AA) was introduced by Lighthill,[8, 9] with the purpose to study jet noise. Since its introduction the AA has been widely used and reinterpreted in various forms, such as the FW-H equation for helicopter rotor noise or moving sources. Although the AA was introduced for jet noise studies the application on this field has been less successful than the FW-H equation in helicopter rotor blade noise. This is due to the non-deterministic nature of the jet noise which requires very sophisticated turbulence modelling in order to be resolved.

Farassat et al. in [81], give a general definition of Acoustic Analogy. It could be summarised as follows. Given some noise sources generated by turbulence or moving surfaces confined to a finite region of space V, it is possible to assume that the time-dependent information, i.e. time histories, are available on all flow parameters and surface pressure distributions inside V for a sufficiently long period of time. Assuming that pressure fluctuations outside the volume V satisfy the linear wave equation, the conservation laws can be rearranged into the following form:

$$Lp = Q \tag{3.4}$$

where p is the acoustic pressure, L is a linear or nonlinear partial differential operator. The inhomogeneous term of this differential operator, Q, depends on the flow parameters and is assumed known.

Any noise prediction methodology based on eq.(3.4), in which L is the linear wave operator, can be defined as Acoustic Analogy. In particular Lighthills equation, as will be discussed later, has the same form of eq.(3.4), where in this case L is the linear wave operator and the inhomogeneous term is represented by the so called Lighthill stress tensor T_{ij}, eq.3.12. Given the great advances in turbulence modelling and CFD predictions, researchers can now obtain very accurate jet noise prediction coupling accurate near-field CFD calculation with Acoustic Analogy. In effect, some recent results on jet noise calculations exploiting the LAA, from Hunter and Thomas [82], are in very good agreement with the measured data. This means that the Lighthill's Acoustic analogy coupled with a reliable and accurate CFD prediction represent a good alternative to the DNC or the LEEs methods.

Its application is though limited to noise prediction in the cases where no surfaces in motion are involved. In presence of surfaces in motion, such as helicopter rotor blades, wind turbines or Propfan engines, the noise prediction must be carried out

exploiting either the Kirchhoff or the FW-H method.

As discussed in the Introduction, by the early 70s noise generation mechanisms of helicopter rotors and propellers were understood fairly well. At the time, propeller noise predictions were performed exploiting the Gutins formula written in the late 30s,[3]. Helicopter noise prediction was more advanced and based on Lowsons formula, [5]. Most noise prediction methods were in the frequency domain. This was the natural approach for the researchers since time domain methods needed more computational resources. Many experimental and theoretical works were being published in Aeroacoustics during that period and a very important one, the Ffowcs Williams Hawkings paper, [11], was based on the recent Lighthills theory.

Lighthill developed the Acoustic Analogy,[8]-[10], in 1961. On this idea relies a great part of the aeroacoustics theory of the integral methods. The original Lighthill's Acoustic Analogy,[8] is an exact rearrangement of the Navier-Stokes Continuity and Momentum equations into an inhomogeneous linear wave equation. This rearrangement can be obtained as follows:

The equation of Continuity, or law of mass conservation is:

$$\frac{\partial \rho}{\partial t} + \frac{\partial (\rho v_i)}{\partial x_i} = 0 \tag{3.5}$$

The Momentum equation, without volume sources:

$$\frac{\partial (\rho v_i)}{\partial t} + \frac{\partial \left(\rho v_i v_j + p_{ij}\right)}{\partial x_j} = 0 \tag{3.6}$$

where

$$p_{ij} = p\delta_{ij} - \tau_{ij} \tag{3.7}$$

$$\tau_{ij} = \mu \left(\frac{\partial v_i}{\partial x_j} + \frac{\partial v_j}{\partial x_i} \right) - \frac{2}{3}\mu \frac{\partial v_k}{\partial x_k}\delta_{ij} \tag{3.8}$$

Lighthill's equation is obtained by applying a time derivative to eq.(3.5) subtracting the divergence of eq.(3.6):

$$\frac{\partial}{\partial t}\left(\frac{\partial \rho}{\partial t} + \frac{\partial (\rho v_i)}{\partial x_i} \right) - \frac{\partial}{\partial x_i}\left(\frac{\partial (\rho v_i)}{\partial t} + \frac{\partial \left(\rho v_i v_j + p_{ij}\right)}{\partial x_j} \right) = 0 \tag{3.9}$$

that can easily be put in a wave equation form starting with:

$$\frac{\partial^2 \rho}{\partial t^2} = \frac{\partial^2}{\partial x_i x_j} \left(\rho v_i v_j + p_{ij}\right) \tag{3.10}$$

and adding the term $-c_o^2 \frac{\partial^2 \rho}{\partial {x_i}^2}$, gives:

$$\frac{\partial^2 \rho}{\partial t^2} - c_o^2 \frac{\partial^2 \rho}{\partial {x_i}^2} = \frac{\partial^2}{\partial x_i x_j} \left(\rho v_i v_j + p_{ij} - c_o^2 \rho \delta_{ij}\right) = q \tag{3.11}$$

In which we can define the Lighthill's Stress Tensor T_{ij} like:

$$T_{ij} = \left(\rho v_i v_j + p_{ij} - c_o^2 (\rho - \rho_0) \delta_{ij}\right) \tag{3.12}$$

The final form of the Lighthill's Analogy is:

$$\frac{\partial^2 \rho'}{\partial t^2} - c_o^2 \frac{\partial^2 \rho'}{\partial {x_i}^2} = T_{ij} \tag{3.13}$$

This is the equation obtained by Lighthill [8]. Introducing the wave operator, $\Box^2$ eq.3.13 can be written in a compact form:

$$\Box^2 \rho' = T_{ij} \tag{3.14}$$

In the presence of solid surfaces and discontinuities it is not possible to find the solution of this differential equation by applying the theory of functions from classical mathematical analysis. In 1969 Ffowcs Williams and Hawkings in [11] derived the form of the Lighthill's Analogy in the case of moving surfaces, and obtained the solution of the inhomogeneous wave equation in integral form, exploiting the theory of generalized functions.

3.2.4 FW-H Equation

The FW-H equation is a generalized form of the Lighthill's Acoustic Analogy and can be used for arbitrarily moving bodies. It was derived by Ffowcs Williams and Hawkings in [11]. This approach falls in the broad category of AA, eq.(3.4) as will be discussed later. The noise prediction is divided in two phases, solution of the flow field inside the dynamic source region via CFD and propagation of the noise

waves, via the integral form of the FW-H equation, from the body surface, or from the near-field boundary in case of porous formulation, up to the far-field observer.

This allows to save computational time and resources because the CFD solution is limited only to the near-field domain, as opposed to DNC and LEEs where the solution must be computed in all the domain enclosing noise sources and the observer. The main advantage of this approach with respect to the Kirchhoff equation is that the results obtained using the FW-H equation are much less sensitive to the positioning of the near-field domain boundary as well as to the non-linearities in the flow field,[79] and [80].

The FW-H equation exploits the theory of generalized functions, briefly discussed in Appendix A and explained in detail in [83, 84]. For this reason the FW-H equation is applicable in presence of discontinuities and is particularly suitable for solid moving surfaces, such as the blades of a helicopter rotor. Almost all helicopter rotor noise prediction codes are based on this equation.

Given a discontinuity such as an impenetrable (solid) moving surface (or body) described by the function $f(\mathbf{x},t)=0$, the domain outside this surface is defined as $f(\mathbf{x},t)>0$ and $\nabla f=\hat{\mathbf{n}}$ represents the unit outward normal to the body.

The continuity (3.5) and momentum (3.6) equations in the presence of this discontinuity $f(\mathbf{x},t)$ are correct only if all the quantities are considered as generalized functions and all the derivatives as generalized derivatives. With this position eq.(3.5) becomes:

$$\begin{aligned}\frac{\overline{\partial}\rho}{\partial t}+\overline{\nabla}\cdot(\rho\mathbf{u}) &= \frac{\partial\rho}{\partial t}+(\rho-\rho_0)\frac{\partial f}{\partial t}\delta(f)+\\ +\frac{\partial(\rho u_i)}{\partial x_i}+[\rho u_i]\frac{\partial f}{\partial x_i}\delta(f) &= -(\rho-\rho_0)v_n\delta(f)+\rho u_n\delta(f)\\ &= \rho_0 v_n\delta(f)\end{aligned} \tag{3.15}$$

in which $v_n=-\frac{\partial f}{\partial t}$ is the normal velocity of $f=0$ and the condition of impenetrability $v_n=u_n$ was used.

For eq.(3.6) operating in a similar way, the following generalized form in presence of a solid surface of discontinuity is obtained:

$$\frac{\overline{\partial}}{\partial t}(\rho u_i)+\frac{\overline{\partial}}{\partial x_j}(\rho u_i u_j+P_{ij}) \;=\; [\Delta P_{ij}n_j]\,\delta(f) \tag{3.16}$$

in which $P_{ij}=\tau_{ij}+(p-p_0)\,\delta_{ij}$ is the compressive stress tensor and τ_{ij} is the viscous

stress tensor. Rearranging equations 3.15,3.16 in a similar fashion as done for the Lighthill's equation, but keeping in mind that in this case generalized derivatives need to be exploited:

$$\overline{\Box}^2 p' = \frac{\overline{\partial}^2}{\partial x_i x_j}\left[T_{ij}h(f)\right] - \frac{\overline{\partial}}{\partial x_i}\left\{\left[\Delta P_{ij} n_j\right]\delta(f)\right\} + \frac{\overline{\partial}}{\partial t}\left\{\left[\rho_0 v_n\right]\delta(f)\right\} \quad (3.17)$$

Eq.(3.17) is the FW-H equation, generalized form of the Lighthill's equation. In this equation three source terms are visible which, because their mathematical form, are labelled as monopole, dipole and quadrupole. The first two terms can be also thought as the sources, respectively, of the thickness, loading noise and, the last term, as source of broadband noise and part of the impulsive noises. Given this direct correspondence of each term with a particular noise source for rotor generated noise, the FW-H equation is the base for almost every rotor noise prediction code.

In their paper Ffowcs Williams and Hawkings presented three different variable representations for resolving the above equation in integral form and obtain the acoustic pressure at the given observer positions. These three different representations are commonly known as "Retarded Time", "Emission Surface" and "Collapsing Sphere", names which try briefly to describe the surface on which the integrals are evaluated.

3.2.4.1 Retarded time

All the integral representations can be found starting from the eq.3.17 and using the free space Green's Function:

$$G^0(\mathbf{y},\tau|\mathbf{x},t) = \frac{1}{4\pi r}\delta\left(\tau - t + \frac{r}{c_0}\right) \quad (3.18)$$

in which we can define:

$$g(t,\tau,r) = \tau - t + \frac{r}{c} \quad (3.19)$$

$$r(\mathbf{x}(\mathbf{x}_0,t),\mathbf{y}(\mathbf{y}_0,\tau)) = |\mathbf{x}(\mathbf{x}_0,t) - \mathbf{y}(\mathbf{y}_0,\tau)| \quad (3.20)$$

where r is the distance between the observer in $\mathbf{x}$ and the source in $\mathbf{y}$ positions.

The particular type of integral formulation that can be obtained depends on the choice of the variables which will be used to integrate the Dirac delta function. A

general inhomogeneous wave equation can be written:

$$\overline{\Box}^2\Phi(\boldsymbol{x},t) \;=\; Q(\boldsymbol{x},t)\delta(f) \tag{3.21}$$

in which $f(\mathbf{x},t)=0$ is the surface of discontinuity and $Q(\boldsymbol{x},t)$ is a generic source. The solution of this equation using the above Green's Function is:

$$4\pi\Phi(\mathbf{x},t) \;=\; \int_{-\infty}^{t}\int_{-\infty}^{\infty}\frac{Q(\mathbf{y},\tau)\delta(f)\delta(g)}{r}\mathrm{d}\mathbf{y}\mathrm{d}\tau \tag{3.22}$$

From this general solution of the inhomogeneous wave equation it is possible to obtain every existing formulation for eq.3.17. In particular the Retarded Time formulation can be obtained by choosing the following variable representation in the eq.3.22: $(y_3,\tau)\rightarrow(f,g)$. This yields to:

$$\mathrm{d}\mathbf{y}\mathrm{d}\tau=\frac{\mathrm{d}y_1\mathrm{d}y_2\mathrm{d}f\mathrm{d}g}{|\partial f/\partial y_3||1-M_r|}=\frac{\mathrm{d}S\mathrm{d}f\mathrm{d}g}{|1-M_r|} \tag{3.23}$$

which brings the following integral form for a generic source term $Q(\mathbf{y},\tau)$:

$$4\pi\Phi(\mathbf{x},t) \;=\; \int_{f=0}\left[\frac{Q(\mathbf{y},\tau)}{r|1-M_r|}\right]_{ret}\mathrm{d}S \tag{3.24}$$

All the values in the integral are evaluated at the retarded time:

$$\tau \;=\; t-\frac{r}{c} \tag{3.25}$$

Where $M_r=\mathbf{M}\cdot\hat{\mathbf{r}}=M_i\hat{r_i}$ and the Doppler factor $1-M_r$ comes from the derivative $\frac{\partial g}{\partial\tau}$

The simplification obtained with this position is visible, and a four dimensional integral, in space (y_1,y_2,y_3) and time is reduced to a surface integral, on the physical surface of the body ($f=0$), e.g. the rotor blade.

3.2.4.2 Emission Surface

The Emission Surface representation can be obtained by choosing the following variable representation in the eq.3.22: $(y_3,\tau)\rightarrow(F,g)$, where $F(\mathbf{x},t,\mathbf{y})=f(\mathbf{y},\tau=$

$t - \frac{r}{c}$), i.e. the surface f calculated at the retarded time $\tau = t - \frac{r}{c}$. This yields to:

$$\mathrm{d}\mathbf{y}\mathrm{d}\tau = \frac{\mathrm{d}y_1\mathrm{d}y_2\mathrm{d}F\mathrm{d}g}{\partial(F,g)/\partial(y_3,\tau)} = \frac{\mathrm{d}y_1\mathrm{d}y_2\mathrm{d}F\mathrm{d}g}{N_3|\nabla F|} = \frac{\mathrm{d}\Sigma\mathrm{d}F\mathrm{d}g}{|\nabla F|} \tag{3.26}$$

where $N_3|\nabla F| = \partial F/\partial y_3$ and $\Sigma = (dy_1 dy_2)/N_3$. With the position

$$\Lambda = |\nabla F| = \sqrt{1 - 2M_n\cos\theta + {M_n}^2}. \tag{3.27}$$

Substituting the expressions above in eq.3.22 this solution can be written:

$$4\pi\Phi(\mathbf{x},t) \;=\; \int_{F=0} \frac{1}{r}\left[\frac{Q(\mathbf{y},\tau)}{\Lambda}\right]_{ret} \mathrm{d}\Sigma \tag{3.28}$$

The values in the integral, inside the square brackets, must be evaluated at the retarded time $\tau = t - \frac{r(\tau)}{c}$. Even in this case the reduction of the number of dimensions involved in the integral is clear. The integral is reduced from a four dimensional integral to a surface integral, but this time on the Emission Surface, i.e. the locus of the points of the geometrical surface f whose disturbance reaches the observer at the same time t.

3.2.4.3 Collapsing Sphere

The Collapsing Sphere can be obtained by choosing the following variable representation in the eq.3.22: $(y_2, y_3) \rightarrow (f, g)$. This yields to:

$$\mathrm{d}\mathbf{y}\mathrm{d}\tau = \frac{\mathrm{d}y_1\mathrm{d}f\mathrm{d}g\mathrm{d}\tau}{\partial(f,g)/\partial(y_2,y_3)} = \frac{\mathrm{d}y_1\mathrm{d}F\mathrm{d}g\mathrm{d}\tau}{(\nabla f \times \nabla g)\cdot\hat{e_1}} = \frac{c\mathrm{d}\Gamma\mathrm{d}f\mathrm{d}g\mathrm{d}\tau}{\sin\theta} \tag{3.29}$$

where Γ is the curve intersection between the collapsing sphere and the surface $f = 0$, and θ is the angle between ∇f and r. Using this transformation in eq.(3.22) gives:

$$4\pi\Phi(\mathbf{x},t) \;=\; \int_{-\infty}^{t}\int_{f,g=0} \frac{Q(\mathbf{y},\tau)}{r\sin\theta}\mathrm{d}\Gamma\mathrm{d}\tau \tag{3.30}$$

The reduction of the four dimensional integral leads this time to two one dimensional integrals, one in time and the other one over the intersection curve between the surfaces $f = 0, g = 0$.

All the existing codes for rotor noise prediction are based on one of the aforementioned formulations. In particular the "retarded time" representation has been

extensively used since it allows to evaluate the integrands directly on the physical surface of the body. Hence, a complex surface construction is not required, as would be for the other two formulations.

3.2.5 Farassat's Formulations

Farassat can be considered as one of the most active researchers in aeroacoustics. He developed a formulation based on the FW-H equation in retarded time known as Farassat's Formulation 1 in 1975, [13]. Many other studies have followed his effort to find more efficient and robust formulations. In total, to the knowledge of the author, Farassat developed 4 different formulations, [13],[85]-[86], for the solution of the FW-H equation. Two different version of Farassat's first formulation, also denoted as Formulation 1 and 1A,[13]and [85], have been exploited during the course of the research presented here.

3.2.5.1 Formulation 1

This formulation is an integral formulation of the eq.3.17, based on the retarded time coordinates representation for the general solution obtained applying the free space 3D Green's Function. Let's analyse in more detail the steps to obtain this integral equation.

It is clear from eq.(3.17) that three different source terms can be identified. Each term can be treated separately as an inhomogeneous wave equation for the acoustic pressure fluctuations p'. The free space Green's function can be applied to find the solution for each one of the three wave equations:

$$\overline{\Box}^2 p' = \frac{\overline{\partial}}{\partial t}\left\{\left[\rho_0 v_n\right]\delta(f)\right\} \tag{3.31}$$

$$\overline{\Box}^2 p' = -\frac{\overline{\partial}}{\partial x_i}\left\{\left[\Delta P_{ij} n_j\right]\delta(f)\right\} \tag{3.32}$$

$$\overline{\Box}^2 p' = \frac{\overline{\partial}^2}{\partial x_i x_j}\left[T_{ij} H(f)\right] \tag{3.33}$$

The solutions for each source term, following [83], can be obtained using a form similar to eq.(3.22). Using the Retarded Time Formulation, the three terms above

have the integral form:

$$4\pi p' = \frac{\partial}{\partial t}\int \left[\frac{\rho_0 v_n}{r|1-M_r|}\right]_{ret} \mathrm{d}S \tag{3.34}$$

$$4\pi p' = -\frac{\partial}{\partial x_i}\int \left[\frac{P_{ij} n_j}{r|1-M_r|}\right]_{ret} \mathrm{d}S \tag{3.35}$$

$$4\pi p' = \frac{\partial^2}{\partial x_i x_j}\int \left[\frac{T_{ij}}{r|1-M_r|}\right]_{ret} \mathrm{d}S \tag{3.36}$$

The above results were found from FW-H [11]. In order to arrive to the Farassat's Formulation 1, the above space derivatives must be transformed in time derivatives. This can be done according to the know relationship of the Green's function:

$$\frac{\partial}{\partial x_i}\left[\frac{\delta(f)}{4\pi r}\right] = -\frac{1}{c}\frac{\partial}{\partial t}\frac{r_i}{r}\left[\frac{\delta(f)}{4\pi r}\right] - \frac{r_i}{r}\left[\frac{\delta(f)}{4\pi r^2}\right] \tag{3.37}$$

and applied to (3.34-3.36) leads to:

$$\begin{aligned} 4\pi p' = &\frac{\partial}{\partial t}\int \left[\frac{\rho_0 v_n}{r|1-M_r|}\right]_{ret} \mathrm{d}S + \frac{1}{c}\frac{\partial}{\partial t}\int \left[\frac{P_{ij}\hat{r}_i n_j}{r|1-M_r|}\right]_{ret} \mathrm{d}S \\ &+ \int \left[\frac{P_{ij}\hat{r}_i n_j}{r^2|1-M_r|}\right]_{ret} \mathrm{d}S + \frac{1}{c^2}\frac{\partial^2}{\partial t^2}\int \left[\frac{T_{ij}\hat{r}_i\hat{r}_j}{r|1-M_r|}\right]_{ret} \mathrm{d}S \end{aligned} \tag{3.38}$$

The terms in the above equation still clearly represent the Thickness term in the first row and the Loading and Quadrupole terms in the second row of the equation, respectively .

3.2.5.2 Formulation 1A

This formulation is based on the same steps followed to obtain eq.(3.38). In order to arrive to the Farassat's Formulation 1A the time derivatives outside the integrals in eq.(3.38) must be taken inside. This can be done by exploiting the following relationship between derivatives on observer time and source time:

$$\left.\frac{\partial}{\partial t}\right|_x = \left(\frac{1}{|1-M_r|}\left.\frac{\partial}{\partial \tau}\right|_x\right) \tag{3.39}$$

by applying eq.3.39 to (3.38) the thickness and loading terms are:

$$\begin{aligned} 4\pi p' = & \int \left[\frac{\rho_0 \dot{v}_n + v_{\dot{n}}}{r|1-M_r|^2} \right]_{ret} \mathrm{d}S \\ & + \int \left[\frac{\rho_0 v_n (r\dot{M}_r + cM_r + cM^2)}{r^2|1-M_r|^3} \right]_{ret} \mathrm{d}S \end{aligned} \tag{3.40}$$

$$\begin{aligned} 4\pi p' = & \frac{1}{c} \int \left[\frac{\dot{l}_r}{r|1-M_r|^2} \right]_{ret} \mathrm{d}S + \int \left[\frac{l_r - l_M}{r^2|1-M_r|^2} \right]_{ret} \mathrm{d}S \\ & + \int \left[\frac{l_r (r\dot{M}_r + cM_r + cM^2)}{r^2|1-M_r|^3} \right]_{ret} \mathrm{d}S \end{aligned} \tag{3.41}$$

3.2.6 Quadrupole term

The Quadrupole term is usually neglected if the blade motion is subsonic because its contribution is of order $o(M^4)$, [8, 9], i.e. turbulence is an inefficient sound source. In case of high Mach number flows, near transonic and supersonic, the importance of the quadrupole term is well known, [41],[40] and [46]. The Lighthill's stress tensor T_{ij} is defined as:

$$T_{ij} = \rho u_i u_j + \left\{ (p - p_0) - c_0^2 (\rho - \rho_0) \right\} \delta_{ij} \tag{3.42}$$

The integral form of the quadrupole term in eq.(3.17) is:

$$4\pi p' = \frac{\partial^2}{\partial x_i x_j} \int_{-\infty}^{t} \int_{-\infty}^{\infty} \left[\frac{T_{ij} H(f) \delta(g)}{r} \right] \mathrm{d}\mathbf{y} \mathrm{d}\tau \tag{3.43}$$

The solution for the acoustic pressure generated from such a term would require the evaluation of a 4 dimensional integral and a double differentiation in space, which would be a very computationally expensive task. However, this kind of approach is not actually necessary because the Lighthill stress tensor T_{ij} vanishes outside of the source region. For a far-field observer in the plane of rotation of the sources the collapsing sphere can be locally approximated by a circular cylinder. Since the observer is assumed to be in the rotor plane, integration in the direction normal to the rotor plane can be performed independent of the observer position.
The derivatives in observer space can be changed with derivatives computed in the

observer time t using the same method exploited in eq.(3.37):

$$\begin{aligned}\frac{\partial^2}{\partial x_i x_j}\left[\frac{\delta(g)}{r}\right] =& \frac{1}{c^2}\frac{\partial^2}{\partial t^2}\left[\frac{\hat{r}_i\hat{r}_j\delta(g)}{r}\right] + \frac{1}{c}\frac{\partial}{\partial t}\left[\frac{(3\hat{r}_i\hat{r}_j-\delta_{ij})\delta(g)}{r^2}\right] \\ &+ \left[\frac{(3\hat{r}_i\hat{r}_j-\delta_{ij})\delta(g)}{r^3}\right]\end{aligned} \tag{3.44}$$

Using the above equation in eq.(3.43) the following terms are obtained:

$$\begin{aligned}4\pi p' = \frac{1}{c^2}\frac{\partial^2}{\partial t^2}\int_{-\infty}^{t}\int_{-\infty}^{\infty}\left[\frac{T_{rr}\delta(g)H(f)}{r}\right]\mathrm{d}\mathbf{y}\mathrm{d}\tau \\ +\frac{1}{c}\frac{\partial}{\partial t}\int_{-\infty}^{t}\int_{-\infty}^{\infty}\left[\frac{(3T_{rr}-T_{ii})\delta(g)H(f)}{r^2}\right]\mathrm{d}\mathbf{y}\mathrm{d}\tau \\ +\int_{-\infty}^{t}\int_{-\infty}^{\infty}\left[\frac{(3T_{rr}-T_{ii})\delta(g)H(f)}{r^3}\right]\mathrm{d}\mathbf{y}\mathrm{d}\tau\end{aligned} \tag{3.45}$$

Where $T_{rr} = T_{ij}\hat{r}_i\hat{r}_j$ and $T_{ii} = T_{ij}\delta_{ij}$.

It is clear that this term would require the most of the computational time during the calculations, so many researchers try to neglect it whenever possible. The term cannot be neglected during HSI calculations given its important contribution to HSI noise sources. As discussed above this HSI noise source propagates mainly along directions parallel to the rotor disk plane with almost no contribution in the normal direction, for these reasons Brentner and Holland, [41] proposed an efficient approximation for the above term. They define the quadrupole source strength on the rotor plane as:

$$Q_{ij} \;=\; \int_{f>0} T_{ij}\mathrm{d}z \tag{3.46}$$

This approximation means that the quadrupole is integrated over the direction normal to the rotor disk, z, but the integration is performed only outside of the rotor blade. With this position and for the properties of the HSI noise, Q_{ij} will be non zero only in the region close to the rotor blade planform.

Using Q_{ij} inside the quadrupole term integrals and after some manipulations, it is possible to obtain the following form for the far-field quadrupole term approximation

exploiting the emission surface formulation:

$$\begin{aligned} 4\pi p' = \frac{1}{c^2}\int \frac{1}{r}\hat{r}_i\hat{r}_j \left[L_\tau^2 Q_{ij}\right]_{ret} \mathrm{d}\Sigma \\ +\frac{1}{c}\int \frac{1}{r^2}\left[3L_\tau Q_{ij}\hat{r}_i\hat{r}_j - L_\tau Q_{ij}\right]_{ret} \mathrm{d}\Sigma \\ + \int \frac{1}{r^3}\left[3Q_{rr} - Q_{ii}\right]_{ret} \mathrm{d}\Sigma \end{aligned} \tag{3.47}$$

Where L_τ is a differential operator defined as $L_\tau = \frac{\partial}{\partial\tau} - \frac{\partial\eta}{\partial\tau}\cdot\nabla_\eta$

3.2.7 FWH Porous Formulation

Although less computationally demanding with respect to the original quadrupole term, the method discussed above is an approximation of the original equation. Di Francescantonio in [87] proposed an alternative form for the FW-H equation and the Farassat Formulation 1 eq.(3.38) which allows to neglect the volume integral of the quadrupole term after a careful choice on the position of the integration surface, which in this case doesn't need to be the blade surface. This is known as the *Porous Formulation* of the FWH or, as di Francescantonio [87], KFWH meaning that it combines the 2 approaches of Kirchhoff and Ffowcs Williams - Hawkings.

The FW-H equation (3.17)has been obtained with the assumption that the surface of discontinuity, represented by $\delta(f)$ is impermeable, e.g. the blade surface. It is possible to drop this assumption, as was already suggested in the paper of Ffowcs Williams and Hawkings, [11], and reconsidered by di Francescantonio. Going back to the inhomogeneous wave equation of Lighthill [8] and assuming that S is permeable, a equation similar to (3.17) is obtained:

$$\begin{aligned} \overline{\Box}^2 p' = \frac{\overline{\partial}}{\partial t}\left\{\left[\rho_0 v_n\right]\delta(f)\right\} + \frac{\overline{\partial}}{\partial t}\left\{\left[(\rho-\rho_0)(v_n-u_n)\right]\delta(f)\right\} \\ -\frac{\overline{\partial}}{\partial x_i}\left\{\left[P'_{ij}n_j\right]\delta(f)\right\} - \frac{\overline{\partial}}{\partial x_i}\left\{\left[\rho v_i(v_n-u_n)\right]\delta(f)\right\} + \frac{\overline{\partial}^2}{\partial x_i x_j}\left[T_{ij}h(f)\right] \end{aligned} \tag{3.48}$$

where v_n is the fluid perturbation velocity normal to S and u_n is the normal velocity of S and since S is considered permeable $(v_n - u_n) \neq 0$. It is possible to rearrange the terms of this equation in order to obtain a form similar to (3.17), using the following variables:

$$V_i = v_i + [(\rho/\rho_0) - 1](v_i - u_i)\ ,\ L_{ij} = P'_{ij} + \rho v_i(v_j - u_j) \tag{3.49}$$

then (3.48) becomes:

$$\overline{\Box}^2 p' = \frac{\overline{\partial}}{\partial t}\left\{\left[\rho_0 V_n\right]\delta(f)\right\} - \frac{\overline{\partial}}{\partial x_i}\left\{\left[L_{ij} n_j\right]\delta(f)\right\} + \frac{\overline{\partial}^2}{\partial x_i x_j}\left[T_{ij} h(f)\right] \tag{3.50}$$

From eq.(3.50) applying the same consideration made to obtain (3.38), it is now possible to find the integral form for all the source terms except the quadrupole term, obtaining:

$$p'(\mathbf{x},t) = \frac{1}{4\pi c_0}\frac{\partial}{\partial t}\int_S \left[\frac{\rho_0 c_0 V_n + L_{nr}}{r|1-M_r|}\right]_{ret} \mathrm{d}S + \frac{1}{4\pi}\int_S \left[\frac{L_{nr}}{r^2|1-M_r|}\right]_{ret} \mathrm{d}S \tag{3.51}$$

Equation (3.51) is then the porous surface version of the Farassat Formulation 1. The quadrupole term can be neglected since now the porous surface can be moved farther away from the near-field in order to include the non linear terms, in a fashion similar to Kirchhoff methods. The added advantage of the porous FW-H method with respect to the standard Kirchhoff method is the much lower sensitivity of the noise prediction to the surface location, [80].

It should be noted that any acoustic source which falls inside $f = 0$ surface will only contribute to the overall noise prediction through the surface-source terms which for porous surfaces can be considered as "pseudo thickness" and "pseudo loading" terms (pseudo because they are not referred to a blade but to a porous surface). On the other hand, any acoustic source outside $f = 0$ must be included in the computation via the volume source term.

It follows that with a careful positioning of the porous surface, so that it encloses all the acoustic sources, the volume sources, i.e. quadrupole term, can be legitimately neglected. This brings a significant computational saving of time and resources, but only recently the availability of accurate CFD prediction enables the use of the FWH equation on a permeable surface

3.2.8 Supersonic formulations

The discussion above referred to subsonic sources and noise prediction methods based on the classical retarded time algorithms. This representation is in fact widely used in noise prediction codes for the simplicity of implementation and its computational efficiency for subsonic conditions. The only flaw which affects algorithms based on the "retarded time" formulation is the presence of the Doppler factor

$|1 - M_r|$ at the denominator of every integrand. This becomes a singularity when $M_r = 1$ and restricts the use of such algorithms to subsonic cases.

Hence, in cases of transonic and supersonic conditions can only be used noise prediction codes which are based on the Emission Surface or Collapsing Sphere formulations. The use of such formulations has been avoided by the majority of researchers because , the construction of the required integration surfaces is complex and arises many issues.

As will be discussed in the following subsections, few studies have investigated the possibilities of exploiting the two aforementioned representations, [42], [44] and [45]. An alternative to these two complex formulations has been recently proposed by a group of researchers, [49]. It is based on the retarded time formulation but the Doppler singularity have been eliminated with careful considerations. The method exploits a *source time dominant* or *forward time* algorithm with the assumption of *fully non compact sources*, which eliminates the mathematical singularity.

In the next subsections it follows a description of the aforementioned formulations for supersonic sources.

3.2.8.1 Collapsing Sphere and Emission Surface Algorithms

In order to avoid the Doppler singularity, one of the two formulations, Collapsing Sphere or Emission Surface, must be exploited instead of the Retarded Time representation. The integral solution of the FW-H equation using these two formulations, for a generic source $Q(\boldsymbol{y}, \tau)$, is given by: Collapsing Sphere

$$4\pi\Phi(\mathbf{x}, t) = \int_{-\infty}^{t} \int_{f,g=0} \frac{Q(\mathbf{y}, \tau)}{r \sin\theta} \mathrm{d}\Gamma \mathrm{d}\tau \tag{3.52}$$

and Emission Surface

$$4\pi\Phi(\mathbf{x}, t) = \int_{F=0} \frac{1}{r} \left[\frac{Q(\mathbf{y}, \tau)}{\Lambda}\right]_{ret} \mathrm{d}\Sigma \tag{3.53}$$

which are obtained as described in paragraph 3.2.4 but no detail was given on the meaning of the integration surfaces, $f(\mathbf{y}, \tau), g(t, \tau, r) = 0$ and $F(\mathbf{x}, t, \mathbf{y}) = 0$, and how to construct them.

It must be noted that although the Doppler singularity does not affect these formulations, two different kind of terms, $\sin\theta$ and Λ are visible at the denominators of

the Collapsing sphere and Emission surface integrands. Studies, [13, 78, 80] showed that the two terms become singular only for particular configurations and for most of these cases they are integrable singularities. Next follows a description of the available methods for the construction of the integration surfaces with a discussion on the behaviour of terms at the integrand denominators.

The **Collapsing Sphere** algorithm was devised first by Farassat in [13] and it was first exploited in a computer code by Farassat, [88, 43], during the end of 80s, when the research on Propfan applications was very active. The way of constructing the curves along which the integration is performed follows a simple idea which gives the name to this formulation. A sphere centred on the observer position with a radius $r = t - \tau$ decreasing from $r = \infty$ when $\tau = -\infty$, to $r = 0$ for $\tau = t$, i.e. collapsing, will intersect the body along the required curves. It can appear that the algorithm could have a straight forward implementation in a computer code, but the calculation of the intersection curves between the sphere and the blade surface (or the porous surface) requires large computational time. This restricts the use of the Collapsing Sphere formulation only in the case of supersonic sources, while the subsonic ones must be analysed via the classical retarded time representation. The $sin\theta$ term at the integrands denominator becomes singular only if the panel over which the integration is being performed has the unit normal vector $\hat{\mathbf{n}}$ parallel to the radiation vector $\hat{\mathbf{r}}$.

The **Emission Surface** representation is the one which shows the most simple integrands form and is not affected by the Doppler singularity, but the terms can be singular when $\Lambda = 0$. Farassat, [13], demonstrated how this singularity can be integrated for many of the cases in which $\Lambda = 0$. Furthermore Farassat and Myers, [78], showed how the singularity is eliminated when the quadrupole term is included in the equation. The fact that the Λ singularity can be integrated or eliminated makes the Emission Surface formulation the perfect candidate for high speed sources. Currently though, just two researchers, Brenter, [44] and Ianniello, [45], implemented this formulation because the construction of the emission surface is complicated and presents many issues.

The aforementioned surface is the intersection between the collapsing sphere and the volume described by the motion of the surface on which the flow variables have been calculated, i.e. the volume described by the motion of the rotor blade or by the porous surface enclosing the near field domain.

Brentner, [44], devised a particular algorithm to construct the emission surface,

labelled as the **Marching Cubes Algorithm**. This algorithm is based on a method exploited in computer graphics to produce iso-surfaces, the marching cubes method. Exploiting an advanced time algorithm the observer times are calculated for all the source times in every grid point. The values are then stored. By using the marching cubes algorithm it is possible to compute the iso-surfaces of constant observer time, i.e. the emission surfaces. Similar to the Collapsing Sphere algorithm, this procedure is also more time consuming with respect to the classical retarded time, and hence its use is confined mostly to supersonic sources.

The **K-algorithm** was proposed by Ianniello, first in [45] and recently improved [48]. It is based on a sophisticated method for the construction of the emission surface where the points are obtained solving the retarded time equation. The multiple roots, which characterise the retarded time equation in supersonic conditions, are obtained for every point by sweeping the retarded time function in two different directions. One direction with increasing source time τ and the other with decreasing τ. Ianniello then implemented in the algorithm a method of classifying each point of the surface as single, mixed or multiple source. Each point source could have in fact up to three roots, i.e. three different locations for a given observer time instant, or could have one distinct and two coincident roots, or one single root. The multiple sources are thus divided in the different categories so to have a more accurate reconstruction of the multiple branches of a supersonic Emission surface. This Emission Surface algorithm is certainly the one which gives predictions of HSI noise in very good agreement, as will be shown in Section 6.3, with the experiments, but it is clear that the surface reconstruction is very sophisticated. The process can be computationally demanding in certain conditions and the algorithm requires a careful and complex implementation in a computer code.

3.2.8.2 Advanced Time or Source Time Dominant Algorithm

The solution of the retarded time equation can be obtained much faster if, instead of considering a particular observer time and then finding the corresponding source time, the process is inverted, i.e. the source time is fixed (dominant) and the time at which the acoustic signal reaches the observer is considered as the unknown. From this assumption derives the name Advance time or Source Time dominant algorithm. If the observer $\mathbf{x}$ is stationary, then $t = \tau + r/c$, can be obtained analytically without any need to use iterative methods. Otherwise, in case of a moving observer the equation becomes slightly more complex, $t - \tau - |\mathbf{x}(t) - \mathbf{y}(\tau)|/c = 0$, but its solution

is still simpler than solving the same equation in τ. In fact, the source motion, especially for helicopter blades, is much more complex than the observer motion which could be at most a linear function of t. It should be noted that a sequence of equally spaced source times will lead to a sequence of unequally spaced observer times, hence an interpolation is required to obtain an equally spaced observer time history. Using this approach is possible to further speed up the noise predictions, as shown in [89]-[91], with respect to the classical retarded time formulation. In the classical algorithms the largest part of the computational cost for each time step is due to the solution of the retarded time equation (3.25) using iterative root finder algorithms such as Newton-Raphson and Brent's algorithms.

Still the Advanced Time formulations are characterised by the Doppler singularity for $M_r = 1$. In order to avoid the Doppler singularity Prieur et al., [89] and Kessler et al., [90] introduced the assumption of considering all the sources, even the smallest discretisation panels, as *non compact*. This means that each panel, in which the integration surface is divided, emits pressure disturbances which reach the observer over a finite time interval and not in a single time instant.

More precisely, while in the classical algorithms the integration surface is discretised in panels δS_i which are considered to be compact, $\delta S_i \to 0.$, in [89, 90] this assumption is dropped considering all the panels as *non-compact*. The signals emitted at time t by all the points of δS_i are not received at the same instant in $\mathbf{x}$, but in a finite time interval $\delta t_i = \frac{|\delta r_i|}{c_0}$, which corresponds to the difference in propagation time between the signals emitted by the closest and the farthest points from the observer.

The non-compactness is basically implemented in the method by replacing $\delta(g)$ in equation (3.22) by the function:

$$\begin{aligned} K_i(\mathbf{x}, \tau, t,) = & \left[\frac{[H(g + \Delta g) - H(g)]}{\Delta g}\right]_i \\ = & \frac{\left[H(\tau - t + \frac{(r_i + |\delta r_i|)}{c_0}) - H(\tau - t + \frac{r_i}{c_0})\right]}{\frac{|\delta r_i|}{c_0}} \end{aligned} \tag{3.54}$$

where K_i is the Kernel function. Note that $K_i \to \delta(g)$ when $|\delta r_i| \to 0$, so that the classical Greens function is recovered at the compactness limit when the panel source tends to a point source. Finally, the acoustic pressure radiated by δS_i is

written:

$$p'_i(\mathbf{x},t) = \int_\tau \Pi_i(\mathbf{x},\tau,t)\mathrm{d}\tau \tag{3.55}$$

where:

$$\Pi_i(\mathbf{x},\tau,t) \;=\; \frac{QK_i(\mathbf{x},\tau,t)\delta S_i}{4\pi r_i} \tag{3.56}$$

It can be shown that when δr_i tends to 0, given reception time t and $M_{r_i} \neq 1$, the emission time interval $\Delta\tau = \tau_a - \tau_b$ tends to:

$$|\delta\tau_i| = \frac{(|\delta r_i|/c_0)}{|1-M_{r_i}|} = \frac{\delta t_i}{|1-M_{r_i}|} \tag{3.57}$$

This means that the non-compact result (3.55) tends to the classical compact source result:

$$p'_i(\mathbf{x},t) \;=\; \left[\frac{Q(\mathbf{y_i},\tau)}{4\pi r_i|1-M_{r_i}|}\right]_{ret}\delta S_i \tag{3.58}$$

The Doppler singularity shown in formula (3.58) is avoided, apart from the case where the element is moving with a constant normal velocity equal to c_0 towards the observer.

3.2.9 Research Gaps in Rotor noise prediction

After presenting a detailed analysis of the noise prediction formulations and algorithms available in literature, it is now possible to classify them into two categories; the approaches limited to subsonic sources and approaches capable of handling transonic and supersonic sources. It has been clearly shown that for the aeroacoustic analysis of sources moving in subsonic conditions the Retarded Time formulation is the most widely exploited, but recently the classical retarded time algorithm, [35, 13], has been abandoned by some researchers, [89]-[91], in favour of the more efficient Advanced Time algorithm. The efficiency and capabilities of noise prediction tools based on the retarded time formulation has been demonstrated for long time, but these characteristics, as stated earlier, are limited to subsonic conditions $M_r < 1$ by the Doppler Singularity.

For the prediction of noise from sources which do not fall within these flow conditions three different approaches are available in literature: Collapsing Sphere, Emission

Surface and *non-compact* Advanced time algorithms. The Collapsing Sphere, [88, 42], was the first to be implemented, but the high computational time and moderate accuracy of the noise predictions obtained using this algorithm, [80], make it less competitive with respect to the two other approaches.

The Emission Surface algorithms from Brenter, [44], and Ianniello, [47, 48], when used for subsonic sources are still computationally more demanding with respect to classical retarded time algorithms. However, the noise predictions for transonic source using the Emission surface representation are in good agreement with experiments. For instance, the noise prediction of the UH-1H rotor blade in HSI condition obtained by Brentner, are in good agreement with the experimental campaign conducted by Purcell, [32]. Furthermore, the results obtained by Ianniello are in very good agreement with this experimental campaign even for the most difficult case with $M_T = 0.95$, this will be shown in Section 6.3.

The third approach, based on *non-compact* Advanced Time algorithms, does not require the complex algorithm for the construction of integration surfaces as for the previous two methods, but it requires complex calculations for the integrands and the interpolation of unequally spaced observer time history into equally distributed intervals. The noise predictions obtained via this algorithm are in good agreement with the experiments but they are less accurate if compared to the predictions obtained by Ianniello.

The detailed analysis of the current status of rotor noise prediction helps to highlight some of the existing gaps in this research field. It is clear that both rotor noise predictions for subsonic and supersonic sources are at a very advanced level, but it is also clear that no research effort has been invested to explore the possibility of developing one algorithm which could work efficiently in both subsonic and supersonic regimes. The main reasons are the high efficiency of retarded time algorithms in subsonic regimes and the complex algorithms which are required for the construction of the integration surfaces in supersonic flow conditions.

To the knowledge of the author there has been limited research and a relatively limited progress towards more efficient methods for the solution of the retarded time equation, especially during supersonic conditions when multiple roots are present for a single observer time instant. The difficulties in the solution of the retarded time equation for rotating sources, in case of supersonic motion, has been reported by many researchers,[47, 80], and more recently by Lyrintzis in a review of integral methods for aeroacoustics, [92], but no study on this particular matter have been

published.

An investigation of the methods for solving the retarded time equation will bring more efficient algorithms for the construction of supersonic emission surfaces. Furthermore, a detailed analysis of the behaviour of supersonically rotating sources could lead to the definition of simpler methods to obtain Emission Surfaces. In fact, as stated, above the noise prediction tools based on this formulation are those which gives the most accurate noise prediction for transonic sources and in the presence of strong shock delocalization, i.e. $M_T = 0.9$ and above.

3.3 Summary and conclusions

In the first part of this chapter the main noise sources of helicopter rotor noise have been presented. It is clear that the two most important noise sources are BVI and HSI noise. The former is more important in specific maneuvers such as low speed descent, while the latter is generated when helicopters are moving in high speed forward flight.

In the second part the latest approaches for noise prediction have been introduced. From this discussion, the hybrid approaches resulted as the most suited for practical noise analyses while, given the computational cost, Direct Noise Computation can be used only for cases at small Re_l.

The hybrid approaches using the Ffowcs Williams - Hawkings equation in time domain, are the most exploited for helicopter rotor noise analysis and they have been discussed in the last part of the Chapter. They were divided in methods suited for sources in subsonic motion and methods of sources in supersonic motion. The latter methods are the main focus of this study and it is clear from the analysis that only few algorithms are available for the analysis of sources in transonic/supersonic regimes.

Chapter 4

Development of Numerical Approaches

The integral equations, on which the noise prediction formulations are based, have been presented in Chapter 3, along with the different integral forms and the corresponding integrands. In particular, for the retarded time formulation the general mathematical form of the integrals was obtained in the Chapter 3. For a generic source of strength $Q(\mathbf{y}, \tau)$, function of the source position and time, the integral has the following expression:

$$4\pi\Phi(\mathbf{x}, t) = \int_{f=0} \left[\frac{Q(\mathbf{y}, \tau)}{r^{\alpha_1} |1 - M_r|^{\alpha_2}} \right]_{ret} \mathrm{d}S \tag{4.1}$$

α_1, α_2 are integers which depend on the kind of source, i.e. thickness, loading or quadrupole. The integrals for the Emission Surface formulation have the form:

$$4\pi\Phi(\mathbf{x}, t) = \int_{\Sigma} \left[\frac{Q(\mathbf{y}, \tau)}{r^{\alpha_1} |1 - \Lambda|} \right]_{ret} \mathrm{d}\Sigma \tag{4.2}$$

where $\Lambda = |\nabla F| = \sqrt{1 - 2M_n \cos\theta + {M_n}^2}$. The integrands must be evaluated over the integration surface which is defined by the specific integral representation used. When the retarded time representation is exploited, the physical surface S, on which the pressure and velocity distribution are available, will be used as the integration domain. Otherwise in the cases of Emission Surface or the Collapsing Sphere approaches the control surface S will be used as input in order to calculate the corresponding integration domains. The subscript "ret" in the equations indicated that the integrands must be evaluated at the retarded time $\tau = t - r/c_0$. Hence,

the solution of the retarded time equation is necessary in all the formulations. It is useful to describe the steps which compose the base of a noise prediction algorithm, independently from the specific formulation adopted.

- For the time t_i and panel δS_i, defined by the points $(S_{Pi}, i = 1, P_p)$ (where S_{Pi} are the number of points chosen to represent every single panel), find the corresponding retarded times τ_{Pi}. (In case of ES formulation calculate the emission positions $\mathbf{y}(\tau)_{Pi}$ which form the discretisation of the corresponding emission surface panel $\delta\Sigma_i$)

- Calculate the surface area and aeroacoustic integrals over the panel δS_i (or $\delta\Sigma_i$)

- Repeat the calculations until $t_i \leq T_E$

- Repeat the process for the total number of panels N_p in which the surface is discretised

The main difference between the two formulations is that in Retarded Time the integration domain is the physical control surface S used during the CFD calculations, adopting the ES representation, Σ is the surface generated by the motion of S. More precisely Σ is the emission surface of S and must be recalculated for every observer time instant and position. The interpretation of the above scheme is straight forward, keeping in mind that $(\mathbf{x}, t)$ must be fixed during each step, the complete computation is implemented in three loops. The inner loop evaluates the contribution of all the source δS_i or $\delta\Sigma_i$ in which the control surface is discretised, for a given $(\mathbf{x}_k, t_j)$, then there is a loop to compute the time history of the sources for a fixed observer $\mathbf{x}_k$ and finally, when many observer positions are required, the process must be iterated for all the $\mathbf{x}_k$.

4.1 Retarded time equation

The first requirement in any noise prediction code, independently on the implemented formulation, is the solution of the retarded time equation $g(\tau, t, r/c) = 0$ or $\tau = t - r/c$. In the following paragraphs will be discussed the behaviour of the function $g = 0$ and a novel method for finding the $g = 0$ roots.

For the CS and ES formulations, the construction of the integration domain, which consist of curves in the CS formulation and emission surfaces Σ in the ES representation, can be performed only after the roots of the retarded time equation have been obtained. This is due to the fact that in these formulations both integrands and the domains are function of the retarded time τ, while in the Retarded Time formulation only the integrands depend on τ. For these reasons is clear the necessity of including a fast and efficient root finder algorithm in a noise prediction framework.

Several well known and widely spread root finder algorithms are described in the literature. Considering their efficiency, the Newton-Raphson and the Brent's algorithms are the best exploited methods to accomplish this task,[93]. These techniques are included in many computational tools and exploited in a wide variety of applications, whenever it is required to find the roots of a given function. In the specific case of the retarded time equation the use of one of these methods can identify the roots quite efficiently in subsonic conditions but in supersonic regime, where the retarded time equation has multiple roots for a given observer time instant, the aforementioned methods can easily fail. These two root finder algorithms require the bracketing and initial approximation of each root in order to start the search. Such procedures, and especially the bracketing, will take a considerable part of the computational time, and given the characteristics of the retarded time equation and the presence of local minima and maxima, the solution cannot be guaranteed.

In order to better understand the issues involved in the solution of the retarded time equation, it is helpful to describe the kinematics of the helicopter's main rotor.

4.1.1 Main Rotor Kinematics

The aerodynamic design of the helicopter's main rotor is extremely complex since the first machines were introduced. Today, as described in [94], there are four main types of rotor hubs in use, which vary with the number and position of their hinges. These have been introduced in order to add more degrees of freedom to the blade motion and hence, decrease the aerodynamic loading on the rotor shaft and controls. In particular, the *fully articulated hub* design has two hinges plus a bearing:

flapping hinge allows the blades movement normal to the rotor disk, i.e. the blades can flap up and down depending on the aerodynamic loading

lead/lag hinge adds the in plane movement for the blades which is driven by the drag

pitch bearing allows the blades to feather and is used to control the blades' pitch. This can be operated on all the blades collectively, i.e. collective pitch, changing the magnitude of the rotor's thrust, or cyclically with respect to the blade azimuth, changing the phasing of the aerodynamic loads

The fully articulated rotor is the most complex design considering the number of components and the assembly procedure. Other hub design configurations are the *teetering rotor*, the *hingeless rotor* and the *bearingless rotor*. The teetering rotor has two blades which are hinged on the shaft, i.e. does not use any independent flap or lead/lag hinge. As a consequence, the blades will move like a teetering board, when one flaps up the other will flap down, and hence the name of this rotor configuration.

The hingeless rotor design eliminates the need of flap and lead/lag hinges by using an advanced and sophisticated aeroelastic design of the blades. The hinges are virtual and obtained by flexures in the blade. In this hub design the pitch bearing for the control of the blades is still in use. On the other hand, in the bearingless hub design all hinges and the bearing are eliminated and included in the bending flexing and twisting of the blade structure.

From the discussion above is clear that, for any type of helicopter rotor, the degrees of freedom of the rotor's blades comprise at least flapping, feathering and, for exception of the teetering design, the lead/lagging motion. This means that the motion of a reference frame connected to the main rotor blades with respect to a fixed observer on the ground must include at least all the above degrees of freedom in addition to rotation and translation with respect to the ground fixed reference frame. When considering fuselage and tail rotor the number of intermediate reference frames, which must be taken into account, is much higher. In the current analyses though, the main rotor is assumed as stand alone.

Then, in order to calculate the motion of a point attached to the rotor blades with respect to the absolute ground observer frame, or viceversa, it is necessary to consider at least five intermediate reference frame. It should be noted here that both aerodynamic and aeroacoustic analysis of helicopter rotors must take into account all the aforementioned reference frames, in order to evaluate correctly the blades motion, [35] and [13]. Another reason is that the normal and tangent vectors to the rotor blade surfaces can be easily obtained in a blade fixed frame and, in this

reference frame, they are independent of time.

The reasons above identify the need for an efficient method to describe in the same reference frame (RF) all the variables and vectors which are required for aerodynamics or aeroacoustics calculations, whether the chosen RF is a ground fixed frame or a blade fixed frame. In order to obtain a general expression for the required frame transformations it is better to start from a simple case involving only two reference frames.

Given two generic frames, F_1 and F_2 with the same origin $\mathbf{O_1} = \mathbf{O_2}$ but rotating with respect to each other at an angle α_{21} around the axis x_1, the transformation matrix from F_1 to F_2 is:

$$\begin{pmatrix} x_2 \\ y_2 \\ z_2 \end{pmatrix} = \begin{bmatrix} 1 & 0 & 0 \\ 0 & \sin\alpha_{21} & \cos\alpha_{21} \\ 0 & -\cos\alpha_{21} & \sin\alpha_{21} \end{bmatrix} \begin{pmatrix} x_1 \\ y_1 \\ z_1 \end{pmatrix} \tag{4.3}$$

Eq.4.3 ca be written in a compact form using the following notation:

$$T_{21} = \begin{bmatrix} 1 & 0 & 0 \\ 0 & \sin\alpha_{21} & \cos\alpha_{21} \\ 0 & -\cos\alpha_{21} & \sin\alpha_{21} \end{bmatrix} \tag{4.4}$$

Considering now the particular case of helicopter blades, the above operation must be repeated for the 3 reference frames of flapping, lead/lagging and pitching motion. After these 3 transformations the point motion is known in the frame which is rotating and translating with respect to the rotor shaft. Hence two more transformations are necessary to be implemented in order to obtain the motion with respect to a ground fixed frame, a total of 5 reference frame transformations. An additional rotation is usually required to consider the orientation of the rotor shaft with respect to the ground frame.

Figure 4.1 clarifies the meaning of these latter three frames, the observer frame OF, the GF which is the reference frame fixed to the ground but with the Z axis oriented as the rotor shaft, i.e. rotated at an angle α_s with respect to the ground. The frame MF is oriented in the same fashion as the previous one but is translated with a velocity $\mathbf{V_H}$ and with the origin on the rotor shaft. Finally the rotating frame RF is connected to the MF and rotates with a rotational speed Ω around z_{MF}. The angular, or azimuth, position of RF with respect to MF is $\psi = \psi_0 + \Omega\tau$, where ψ_0 is the initial azimuth position. This is the position with x_{RF} pointing towards

the tail rotor and y_{RF} always fixed to the quarter chord line of the blade number 1. From the RF it is possible to obtain the absolute motion of a blade fixed point using the further three frame transformations which account for the flapping, lead/lagging and pitching motions.

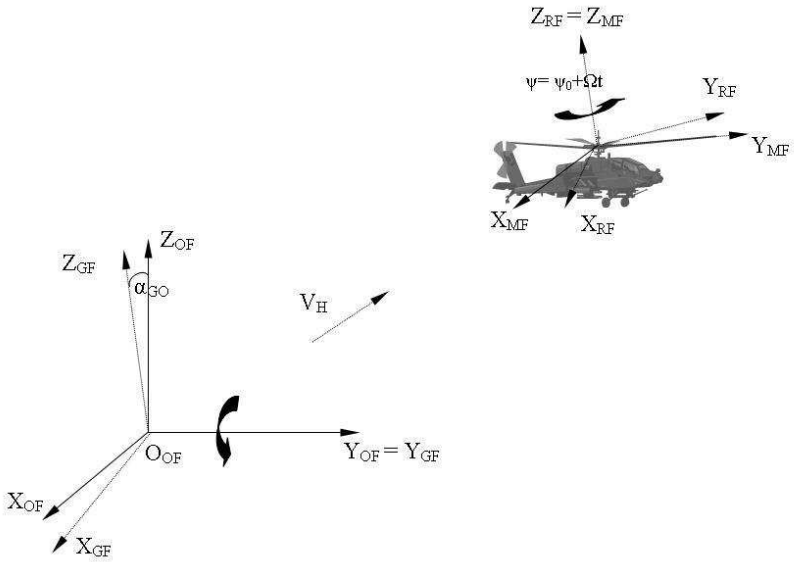

Figure 4.1: Reference frames form Observer to Rotating frame.

Based on the above discussion it is now possible to write the complete equation for the calculation of the radiation vector $\mathbf{r} = \mathbf{x} - \mathbf{y}$ which connects the observer $\mathbf{x}$ to the source point $\mathbf{y}$, fixed with the blade surface:

$$\begin{aligned}\mathbf{r} = &[[T_{GO}]\mathbf{x_{OB}} + \mathbf{V_{OB}}t] \\ &- [([T_{GM}][T_{MR}][T_{RF}][T_{FL}][T_{LB}])\,\mathbf{y_B} + \mathbf{H} + \mathbf{V_h}\tau]\end{aligned} \tag{4.5}$$

where $\mathbf{H} = ([T_{RF}][T_{FL}][T_{LB}])\,\mathbf{fl_h} + ([T_{FL}][T_{LB}])\,\mathbf{ll_h} + ([T_{LB}])\,\mathbf{pt_h}$ accounts for the movements of $\mathbf{fl_h}$, $\mathbf{ll_h}$ and $\mathbf{pt_h}$. These are respectively the offsets for flapping hinge, lead-lagging hinge and pitching hinge. The subscripts OG, GM, MR, RF, FL, LB represent the transformations from Observer to Ground, Ground to Moving, Moving to Rotating, Rotating to Flapping, Flapping to Lead/lagging, Lead/lagging to Blade frame respectively.

It is reminded that the vector $\mathbf{r}$ defined above is a function of $\mathbf{r}((x_0), t, \mathbf{y}, \tau)$ and $\mathbf{x} = \mathbf{x}(\mathbf{x}_0, t)$ and $\mathbf{y} = \mathbf{y}(\mathbf{y}_0, \tau)$. All the matrixes written above in compact form are functions of t and τ. In order to better understand this dependance it is useful to analyse in more detail one of these transformation matrixes.

Defining the flapping angle as $\beta = \beta(\psi)$, this can be represented in the most general case of forward flight as an infinite Fourier series of ψ as:

$$\beta(\psi) = \beta_0 + \beta_{1c}\cos\psi + \beta_{1s}\sin\psi + \beta_{2c}\cos 2\psi + \beta_{2s}\sin 2\psi + \dots \tag{4.6}$$

so that the transformation matrix between the flapping and the rotating reference frame will be, considering that the flapping motion is around the $x_{RF} = x_{FF}$ axis:

$$T_{FR} = \begin{bmatrix} 1 & 0 & 0 \\ 0 & \sin\beta(\psi) & \cos\beta(\psi) \\ 0 & -\cos\beta(\psi) & \sin\beta(\psi) \end{bmatrix} \tag{4.7}$$

This is valid for all the other matrices involving a rotational transformation. The flapping angle β, the lead/lag angle ζ and the pitch angle θ are included in the current software by means of Fourier series truncated at the second harmonic, as illustrated above for β. This approximation is considered sufficiently accurate for noise prediction, [35]. In helicopter aerodynamic analysis the angles connected to the motion of the main rotor are always described via the Fourier series coefficients both during experimental and computational campaigns. It is an efficient approximation to include the strong dependency of these angles on the azimuth position $\psi(\tau)$, and thus indirectly on τ.

The details of the calculation of these coefficients are outside the scope of the current thesis since the procedure is more relevant to aerodynamic analyses, where the forces and moments depend on the aforementioned angles and viceversa. In order to obtain the required Fourier series coefficients that describe the kinematics of the helicopter, the complex equations of the forces and moments must be resolved. This procedure is called rotor trim and for a given helicopter gross weight, centre of gravity and forward speed the trim solution must evaluate: the rotor controls, collective pitch θ_0, cyclic pitches θ_{1c} and θ_{1s}; the rotor disk orientation described by $\beta_0, \beta_{1c}, \beta_{1s}$; and the vehicle orientation.

This complex coupling of aerodynamic and aeroelasticity, which governs helicopter rotor aeromechanics, has led researchers to develop the so called comprehensive tools. These tools are capable of resolving the helicopter trim using iterative coupling between structural and aerodynamic equations. A very detailed discussion on helicopter rotor trim, design and more in general helicopter's aerodynamics can be found in Leishman, [94].

4.1.2 Retarded time behaviour

The definition of the radiation vector $\mathbf{r}$ has been introduced above for a source which is fixed to the helicopter main rotor blades. Without loosing any generality it is possible to analyse here the behaviour of the retarded time solutions for a source fixed to the rotating frame RF, hence neglecting the flapping, led/lagging and pitching motions. The same analysis in effect could be easily extended to include these motions by just adding the further three transformation matrices required. The equation of $\mathbf{r}$ for a source fixed to RF becomes, in the ground frame GF:

$$\mathbf{r} = [[T_{GO}]\mathbf{x_{OB}} + \mathbf{V_{OB}}t] - [([T_{GM}][T_{MR}])\,\mathbf{y_B} + \mathbf{V_H}\tau] \tag{4.8}$$

The retarded time equation was defined in 3.25 but it is useful to write it again along with the definition of $r = |\mathbf{r}|$:

$$\tau = t - \frac{|\mathbf{r}|}{c} \tag{4.9}$$

$$\mathbf{x} = [[T_{GO}]\mathbf{x_{OB}} + \mathbf{V_{OB}}t] \tag{4.10}$$

$$\mathbf{y} = [([T_{GM}][T_{MR}])\,\mathbf{y_B} + \mathbf{V_H}\tau] \tag{4.11}$$

$$\tag{4.12}$$

$$\begin{aligned} |\mathbf{r}| &= \sqrt{\mathbf{r}^T\mathbf{r}} \\ &= \sqrt{\mathbf{x}^T\mathbf{x} + \mathbf{y}^T\mathbf{y} - 2\mathbf{x}^T\mathbf{y}} \end{aligned} \tag{4.13}$$

It is now evident that even for this simplified analysis the retarded time equation, because of the definition of $\mathbf{r}$, is an implicit function of τ and cannot be resolved analytically. In fact, the motion of the source $\mathbf{y}$ is complex and involves transcendental functions. On the other hand, even if the equation is implicit in t, the motion of the observer $\mathbf{x}$ is always simpler to evaluate with respect to the rotating source. The observer could be fixed or moving with a constant velocity, i.e. a linear function of t, so that the roots of g for fixed τ can be easily found. The Forward Time Algorithms exploit this characteristic of the retarded time equation by fixing τ and calculating the time t when the signal reaches the observer, i.e. propagating the signal forward in time at an instant $t > \tau$.

In case of retarded time algorithms, it is necessary to analyse the behaviour of τ and its derivatives with respect to t under several different conditions of motion, in order to devise a more efficient root finder process. It should be noted that the solution

of this equation, given a source point $\mathbf{y_B}$ and an observer point $\mathbf{x_{OB}}$, represents the intersection between the spherical waves centred in $\mathbf{x_{OB}}$ whose radius is varying as $r = (t - \tau)$, and the curve in space described by the motion of the source point $\mathbf{y_B}$ for the same t and τ.

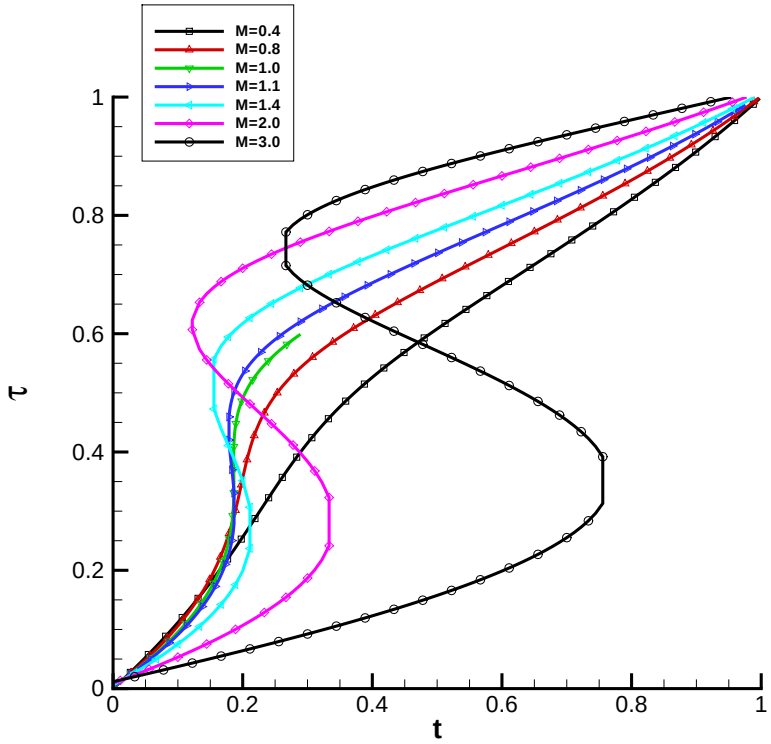

Figure 4.2: Influence of Mach number on t, τ behaviour, t and τ non-dimensionalised over the period $T = \frac{2\pi}{\Omega}$

The radiation distance r is covered by the pressure signal in the time r/c and hence the existence of single or multiple roots of τ depends on the speed at which the source moves along the radiation vector. More precisely, this speed is defined as $\mathbf{v_s} \cdot \hat{\mathbf{r}}$ or in terms of Mach number as $M_r = \mathbf{v_s} \cdot \hat{\mathbf{r}}/c$. The same variable is found when calculating the derivative of the retarded time equation $g = 0$ with respect to τ at constant $\mathbf{y_B}$:

$$\begin{aligned} g(t, \tau, r) &= \tau - t + \frac{r}{c} \\ \frac{\partial g(t, \tau, r)}{\partial \tau} &= 1 + \frac{1}{c} \frac{\partial r}{\partial y_i} \frac{\partial y_i}{\partial \tau} \\ &= 1 - \frac{1}{c} \left(\frac{\mathbf{r}}{r} \cdot \mathbf{v_s} \right) \\ &= 1 - M_r \end{aligned} \tag{4.14}$$

where it was used the relation $\frac{\partial r}{\partial y_i} = -\mathbf{r}/r = -\hat{\mathbf{r}}$ derived from the definition of $\mathbf{r}$ and the subscript s indicates the source. y_i is the i^{th}component of $\mathbf{y}(\mathbf{y_B}, \tau)$. It must be highlighted that, when $g = 0$, t is directly connected to τ. In fact, considering the function $g(t, \tau, r) = 0$, and calculating its derivatives in t and τ for constant $\mathbf{x_{OB}}$ and $\mathbf{y_B}$, the following relation is obtained:

$$\begin{aligned} \frac{\partial g(t,\tau,r)}{\partial \tau}\mathrm{d}\tau + \frac{\partial g(t,\tau,r)}{\partial t}\mathrm{d}t = 0 \\ (1 + \frac{1}{c}\frac{\partial r}{\partial y_i}\frac{\partial y_i}{\partial \tau})\mathrm{d}\tau - (1)\mathrm{d}t = 0 \\ \mathrm{d}t = (1 - M_r)\mathrm{d}\tau \end{aligned} \tag{4.15}$$

From equation 4.15 is clear that the use of equally spaced $\Delta\tau$ intervals, as in the case of forward time algorithms, will yield to unequally spaced observer time history, and hence interpolation is required. Eq.4.15 is equivalent to:

$$\frac{\partial \tau}{\partial t} = \frac{1}{(1 - M_r)} \tag{4.16}$$

From equations 4.16 and 4.15 is clear that the sign of $1 - M_r$, expressed as partial derivative of g with respect to τ, will always be positive when the point source $\mathbf{y_B}$ is moving with subsonic motion $|\mathbf{M}| < 1$, i.e. the function is monotonically increasing and there will be only one root τ for every observer time instant t. This is visible in figure 4.2 for the lines with $M < 1$.

The source's Mach number M depends on the rotational speed Ω, the distance of the source from the rotation point (in $\mathbf{y_R} = 0$), i.e. $|\mathbf{y_B}|$, and the sound speed c (and hence the fluid temperature). By increasing the Mach number of the source, which in the current case is done by increasing Ω, it is possible to observe the behaviour of τ versus the corresponding t. In particular, the steepness of the curve increases, until $M = 1$, and in transonic conditions a part of the curve is perpendicular to the t axis.

Along the trajectory described by the point source there will be only one position for which the condition $M_r = 1$ is satisfied. In particular, considering that for the chosen motion of the source $\mathbf{y_B}$ the trajectory is represented by a circumference of radius $|\mathbf{y_B}|$, the condition $M_r = 1$ is verified when the radiation vector $\mathbf{r}$ is tangent to this path. When the source point passes from this specific position, along its trajectory, is moving toward the observer with the same speed, i.e. the speed of sound c, of its acoustic signal.

The analysis of the second partial derivative of the function g with respect to τ will help to clarify this condition:

$$\begin{aligned}\frac{\partial^2 g}{\partial \tau^2} &= \frac{\partial 1 - M_r}{\partial \tau} \\ &= -\frac{1}{c}\left(\frac{\partial \mathbf{v_s}}{\partial \tau}\cdot\hat{\mathbf{r}} + \mathbf{v_s}\cdot\frac{\partial \hat{\mathbf{r}}}{\partial \tau}\right) \\ &= -\frac{\partial \mathbf{v_s}}{\partial \tau}\cdot\hat{\mathbf{r}}\end{aligned} \tag{4.17}$$

where the $\frac{\partial \hat{\mathbf{r}}}{\partial \tau} = 0$ always.

From the expression of $\frac{\partial^2 g}{\partial \tau^2}$ it is clearly visible that for a rotating point source, $\frac{\partial^2 g}{\partial \tau^2} = 0$ in the same position, along the trajectory of the source, where $\frac{\partial g}{\partial \tau} = 0$. This happens because the acceleration vector $\frac{\partial \mathbf{v_s}}{\partial \tau}$ is normal to the velocity vector which in that point is parallel to $\hat{\mathbf{r}}$. Thus, the dot product in Eq.4.17 is 0. The combination of these two conditions, i.e. first and second derivative equal to 0, means that function g has a cusp and that there is a caustic in the emission surface.

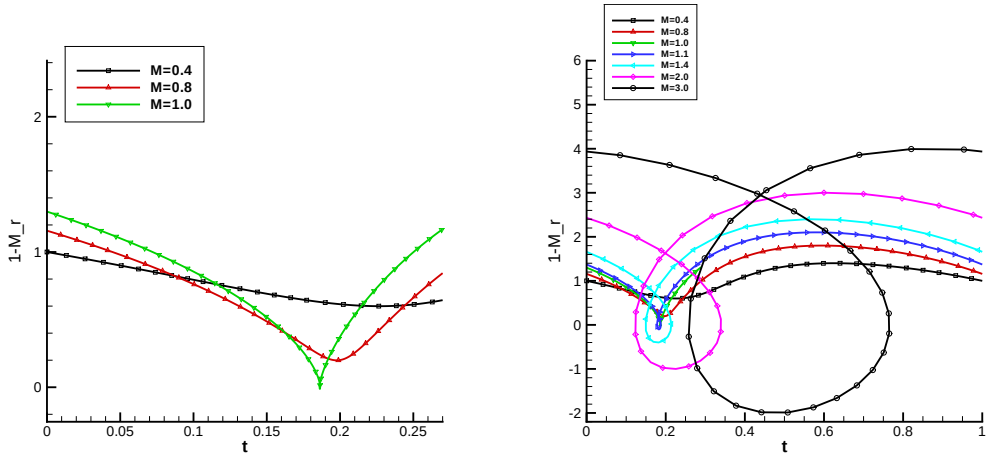

(a) ***Close up of sources with*** $M \leq 1.0$ **(b)** ***Sources with*** $0.4 \leq M \leq 3.0$

Figure 4.3: Behaviour of $1 - M_r$ by varying source rotational speed Ω

When the source Mach number is $M > 1$ the equation $g(t, \tau, r) = 0$ will have multiple roots of τ for a given observer time instant t. This is shown as an S shape in the curves $\tau(t)$ obtained as solutions of $g = 0$. The observer time equation $t(\tau) = \tau^{-1}(t)$ has in this cases two points of local minima or maxima, i.e. two points in which $\frac{\partial t}{\partial \tau} = 0$ or $\frac{\partial g}{\partial \tau} = 0$.

The meaning of the multiple positions of the emission point can be clarified analysing the point source kinematics and physics. There will be three segments of the source

point trajectory from which the emitted acoustic signals will reach the observer at the same time instant. The multiple roots segments of the source point trajectory can be found in proximity of the point where the radiation vector is tangent to $\mathbf{y_B}$ path. It is obvious that at the tangent point M_r will be exactly $M_r = |\mathbf{M}|$. This means that the two points in which $\frac{\partial t}{\partial \tau} = \frac{\partial g}{\partial \tau} = 0$, i.e. $M_r = 1$, can be found via the following equation:

$$(1 - M_r) = (1 - |\mathbf{M}| cos\theta_{rM}) = 0 \tag{4.18}$$

$$\Longrightarrow cos\theta_{rM} = \frac{1}{|\mathbf{M}|} \tag{4.19}$$

The solution of equation 4.18 can be calculated in terms of azimuth values ψ. The two roots of this equation are at a symmetric positions with respect to the tangent point ψ_{tn}. The azimuthal distance of the two roots from ψ_{tn} tends to increase with the increase of M and will reach a value $\Delta\psi$ as close to 90° as much M tends to ∞. In Figure, 4.2, the function $\tau(t)$ when $g = 0$ is plotted for several different values of Mach number M which varies in the range $M = 0.4$ up to $M = 3.0$. The curves show exactly the behaviours described above. Some more insight on the retarded time equation can be gained by looking at the plots of $\frac{\partial g}{\partial \tau}$ and $\frac{\partial^2 g}{\partial \tau^2}$, in Figures 4.3 and 4.4 for Mach numbers varying in the same range as the previous figure. It is clearly visible that the first partial derivative, $1 - M_r$ decreases reaching 0 when $M = 1$ and the cusp is visible. For further increases in M the curves reach the negative quadrant and the existence of multiple roots is obvious.

The analysis in this section was focused on the motion of a single source point. Next follows a discussion on the root finder algorithm developed during this research. After having defined this algorithm, on which is based the construction of the emission surfaces, it will be presented the Σ surface corresponding to the motion of a single panel. The analysis of a simple panel, which is the basic element of surface discretisation, could lead to interesting insights and further clarify the physical behaviour of noise generation from supersonically rotating surfaces. In literature can be found only another study which shows some details on the generation of emission surfaces, [48].

4.1.3 Root finder algorithm

As discussed in the research methodology, Section 2.4, the noise prediction tool developed during the current research is build in a step-by-step fashion, hence, the

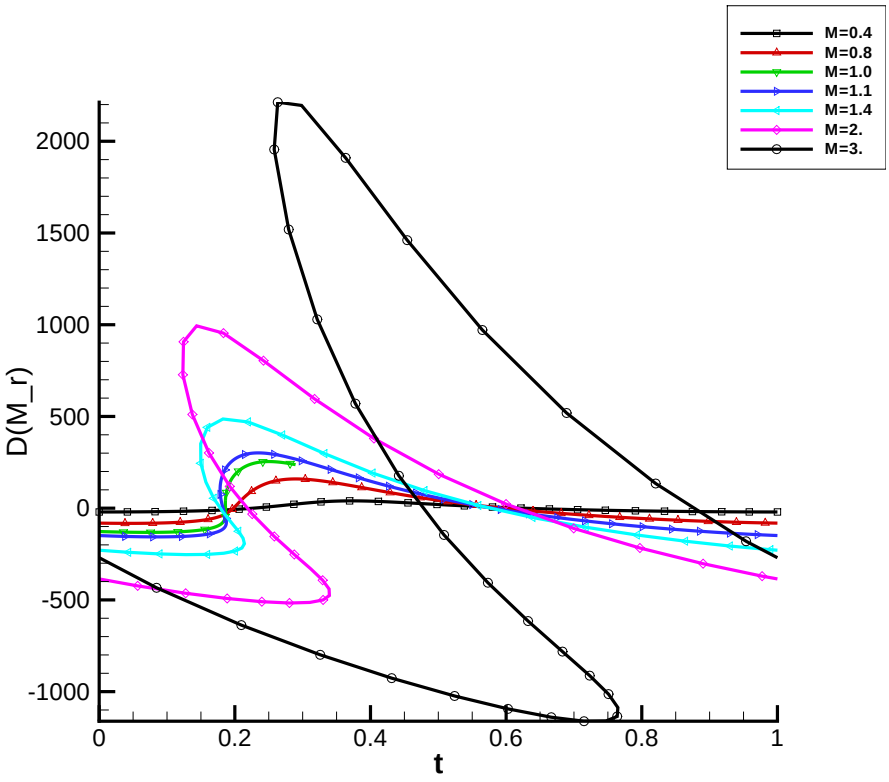

Figure 4.4: Influence of Mach number on $\frac{\partial^2 g}{\partial \tau^2}$

aforementioned root finder algorithms have been included in the initial version of the software. The novel numerical approach to finding the roots of $g = 0$ was then obtained after a detailed investigation based on the knowledge of the problem, on the kinematics of the helicopter rotors and on the observed behaviour of the roots of $g = 0$ in various flow conditions. Some of the ideas at the base of the development of the current algorithm have been introduced above. In the following paragraphs will be shown how the aforementioned analysis leads to the final version of the root finder algorithm implemented during this research.

The analysis of the function $g = 0$, equivalent to $\tau(t, r/c)$, presented above, highlighted the importance of $\frac{\partial g}{\partial \tau}$, as an indicator for the behaviour of τ. For this reason the Newton algorithm was considered as the optimum starting point for the proposed root finder method, which could be considered a modified version of the Newton method.

It is now necessary to show the issues which affect the classical algorithms making them inefficient or not suited for particular conditions, such as supersonic source motion.

The main issue arising in the search of the $g = 0$ roots is the appearance, during the analysis of supersonically moving sources, of multiple roots τ corresponding to the same instant t, whenever $M_r > 1$ along the source's path. It is possible to find these multiple roots by mean of the classical version of Newton's and Brent's algorithms, but in order to do so the roots must be first bracketed. Given an interval $[\tau_1, \tau_2]$, where supposedly the multiple roots are located, the bracketing algorithm will divide the input interval in a user set N_{si} number of sub intervals. The function f under analysis will then be evaluated on the extremes of each sub interval. The process is iterated until is found the sub interval in which f has two opposite signs. It appears that the process described can be quite inefficient.

Assuming that the function g could have up to three multiple roots, the bracketing process must be repeated until the three sub-intervals containing the roots are found. Though, for the function g, the existence of multiple roots is confined only in a small part of the observer time history, while in the most of the observer time axis there will be only one single root. Hence, it is evident that even when g has single τ roots, i.e. during the majority of observer time history, the root bracketing algorithm will inefficiently seek for the other two roots sweeping all the defined N_{si} and thus increasing the computational time. It should be reminded that the root bracketing process must be repeated for every observer time t along the overall observer time

interval $[t_s, t_e]$ defined in the calculation.

The loop described above takes into account only one source point, and hence it must be repeated for all the source points which define the integration domain of interest. This means that the highlighted inefficient behaviour must be repeated for the whole time history $[t_s, t_e]$ and for all the source points under analysis. This process will add many unnecessary steps to the overall computational time.

Unfortunately the root bracketing process is a fundamental step for both Newton's and Brent's algorithms and cannot be avoided. The only possible answer to this issue is to define a root finder method which does not require this time consuming procedure. In order to do so it is helpful to understand how the two aforementioned root finder algorithms work and why they require root bracketing.

It should be noted, once again, that the focus in the analysis which follows is on those cases where g shows a non-monotonic behaviour, i.e. for $M > 1$. For functions $f(x)$ that are non-monotone the two algorithms under analysis can encounter additional difficulties, [93], around local minima and maxima, $\frac{\mathrm{d}f}{\mathrm{d}x} = 0$, and inflection points, $\frac{\mathrm{d}^2 f}{\mathrm{d}x^2} = 0$.

It is well known that the Newton-Raphson method is based on a linear approximation of the function under analysis via a Taylor series expansion truncated at the first order. The method has quadratic convergence and, near the roots will converge very fast, but when the evaluation point is far from a root or close to critical points the method loses its high convergence properties and becomes linear. In the worst cases the algorithm could reach a stall situation, i.e. the evaluation point starts oscillating around the function inflection point and the method cannot reach convergence. It is obvious that the closest to the root will be the first evaluation point, the faster and more certain the method will converge. Hence, the root bracketing process will play an important role in this task both for the Newton's method convergence and to minimize the likelihood of failure in the root search. While for monotonic functions this improvement could be considered optional, in case of non-monotonic functions the root bracketing step is indispensable. The Newton method alone will otherwise fail to provide all the required roots for such functions.

Brents method combines bisection, and inverse quadratic interpolation to obtain the root of a function $f(x)$, within a defined accuracy, inside the neighbourhood of a zero crossing interval. Inverse quadratic interpolation uses three prior points $[x_i, f(x_i)]$ to fit an inverse quadratic function, i.e. x as a quadratic function of $f(x)$, whose value at $f(x) = 0$ is considered the next estimate of the root x. The

algorithm includes also an internal root bracketing which is used in order to prevent the search from jumping outside the brackets of the input interval. Even for the Brent's algorithm it is required a pre-step of a root bracketing algorithm in order to concentrate the search in smaller domains. Furthermore, the Brent's method alone is not suited to compute multiple roots. Only in combination with a root bracketing algorithm, which establishes the multiple roots' intervals, Brent's method can find multiple roots, working separately in each sub-interval.

From the discussion above it can be observed that the linear behaviour of the two methods when the evaluation point is far from the root is the main reason for which the pre-step procedure of root bracketing is required. Another reason is the fact that the Newton's algorithm is better suited for monotonic functions and the Brent's algorithm cannot provide the multiple roots without a previous search of the sub-interval in which these roots exist. A possible solution then, can be to consider a method which is not linear, i.e. which implements an higher order approximation of the function under analysis.

In helicopter rotor aeromechanic analysis, described in the previous section, the motion of the main rotor blades can be defined via transformation matrices between the different reference frames involved. Furthermore the angles, flapping, lead/lagging and pitching are generally represented via Fourier series of the azimuth $\psi = \psi(\tau)$. For these reasons the calculations of $\frac{\partial g}{\partial \tau}$ can be obtained analytically. Thus, Newton's method is the best candidate as a starting point for the improved root finder method developed in this research.

In the Newton-Raphson algorithm, the generic function $f(x)$ is calculated in the point x_i as a Taylor series approximation truncated to the first order, i.e. a straight line tangent to the function f in the point x. Adopting a similar idea, in the proposed algorithm the Taylor series expansion of the function $f(x)$ is truncated instead at the third order. The function is thus approximated as a third order curve which is tangent to f in x. This enhances the accuracy of the approximation which will remain close to the actual function for larger intervals, with respect to the first order series.

Starting from a Taylor series expansion of $g(t, \tau, r)$ around the point τ and keeping constant the other variables:

$$\begin{aligned} g(t, \tau + \Delta\tau, r) = g(t, \tau, r) + \frac{\partial g}{\partial \tau} * \Delta\tau + \\ + \frac{1}{2!}\frac{\partial^2 g}{\partial \tau^2} * \Delta\tau^2 + \frac{1}{3!}\frac{\partial^3 g}{\partial \tau^3} * \Delta\tau^3 + \dots \end{aligned} \tag{4.20}$$

and imposing that the $\Delta\tau$ increment will bring $g \rightarrow 0$ the following polynomial equation is obtained:

$$\frac{1}{3!}\frac{\partial^3 g}{\partial \tau^3} * \Delta\tau^3 + \frac{1}{2!}\frac{\partial^2 g}{\partial \tau^2} * \Delta\tau^2 \frac{\partial g}{\partial \tau} * \Delta\tau + g(t, \tau, r) = 0 \tag{4.21}$$

whose roots will provide three values of $\Delta\tau$ and hence of $\tau^* = \tau + \Delta\tau$ where $g(t, \tau^*, r) = 0$.

In addition, by approximating the function with a 3^{rd} order polynomial, three $\Delta\tau$ are obtained instead of one. The smallest of the three roots of the approximating Taylor series will be, most of the times, under the set tolerance already in the first evaluation. This reduces dramatically the computational time required to solve the whole problem. The gain in computational time remains positive even when considering the additional time required by the calculation of the second and third derivatives of the function.

The solution of the third order polynomial while Newton's algorithm equation is just linear, is another operation which could affect the efficiency and efficacy of the proposed method. If computed efficiently, this process will not increase the computational cost. In the proposed algorithm, the solution of the third order polynomial is obtained by implementing a fast analytical method capable of providing the three roots with a limited number of operations. This analytical method is based on an approach similar to the classical solution of the second order polynomials and was recently proposed by Nickalls, [95]. A description of this solution follows in the paragraphs below.

Considering a generic third order polynomial $y(x)$

$$y = ax^3 + bx^2 + cx + d \tag{4.22}$$

The solution of the cubic equation 4.22 is based on the same ideas as the Cardano solution but introduces the following parameters:

$$\delta = \frac{b^2 - 3ac}{9a^2} \tag{4.23}$$

$$h = 2a\delta^3 \tag{4.24}$$

$$\lambda = 3\delta^2 \tag{4.25}$$

$$x_N = \frac{-b}{3a} \tag{4.26}$$

$$y_N = ax_N^3 + bx_N^2 + cx_N + d \tag{4.27}$$

These parameters are characteristic of the particular polynomial and are used to first to define the expected root patterns, e.g. one real and 2 complex roots or three real roots etc., and then to evaluate the roots. Essentially, these parameters reveal how the solution is connected to the curve's geometry. The Nickalls' method can evaluate the roots of a generic third order polynomial more efficiently than the classical third order Cardano method.

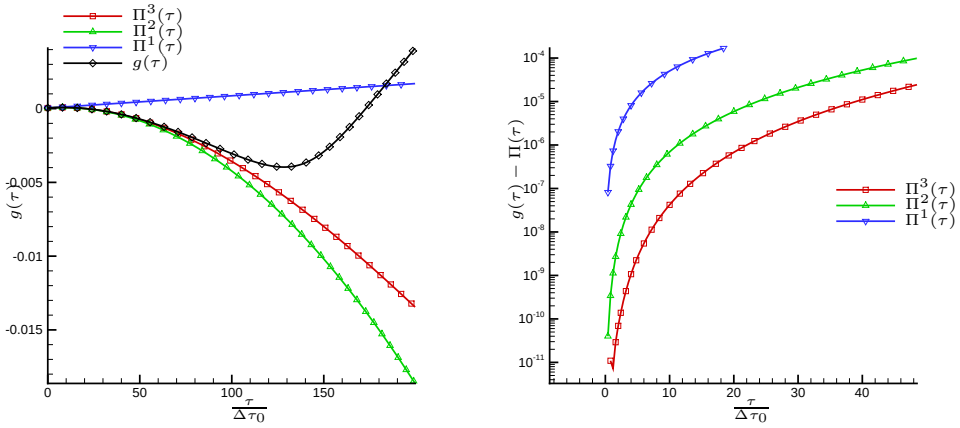

(a) $g(\tau)$ ***and approx polynomials*** $\Pi(\tau)$ **(b)** ***Errors of*** $\Pi(\tau)$

Figure 4.5: Function $g(\tau)$ and approximating polynomials $\Pi(\tau)$ along with the relative errors. ($\Pi^3(\tau)$ is the 3rd order polynomial, $\Delta\tau_0 = \frac{2\pi}{\Omega * 360}$)

The third order polynomial approximation enables to find τ^* even if the evaluation point τ is not very close to the root. This is a great advantage compared to the classical Newton's method which requires close proximity to the root in order to accelerate the convergence. In Figure 4.5 is evident that the approximation errors between the $\Pi(\tau)$ and $g(\tau)$ is, on average, 2 or 3 orders of magnitude smaller with respect to the linear method. In most of the cases, using Π^3, the approximate root of g is already below the set tolerance in the first evaluation. For those cases when this does not happen, it is possible to converge under the limit tolerance by including just one iteration of the linear Newton's method.

Furthermore the three $\Delta\tau$ roots of the polynomial can be ordered by increasing magnitude. The first, smallest, $\Delta\tau$ represents the actual increment required to reach the closest root of the function under analysis. In the cases when g has multiple roots, the second $\Delta\tau$ represents a fairly good estimate of the second closest multiple root of g.

4.1.4 Improved Retarded Time Algorithm

The classic retarded time algorithms are based on the following steps:

- define a starting observer time t_s and a constant positive time increment Δt;
- find for $t_s + i * \Delta t, i = 0, N_t$ the time τ for which $g(t, \tau, r) = 0$, and if $M > 1$ search for 3 roots;
- if $t = t_e$ stop.

The main issue with this particular approach is that the search for multiple roots, when $M > 1$, will be performed in any case whether or not they exist, wasting a lot of computational time in those intervals where only one single root is available. The behaviour of the retarded time τ for several different Mach numbers, fig.4.2, was highlighted in the previous section. In the cases of supersonic motion it is clearly visible the existence of an observer time range where, increasing τ the observer time t first increases then decreases and then finally increases again. Thus, for a positive increment of τ the corresponding increment in t is not always positive.

This observation suggests an approach for the solution of the retarded time equation. The definition of the Δt sign should not be constant and hard-coded in the algorithm but should lean on the behaviour of the retarded time function. An improvement in the efficiency of the standard retarded time algorithm can be obtained by using an increment Δt which is not always positive but can also be negative or zero when required.

It is possible to do this by adding one more step to the base algorithm described above. During this step the algorithm, given the approximating polynomial in the point $g(t, \tau^*, r)$, verifies whether a new approximating polynomial computed in $g(t + \Delta t, \tau^*, r)$ can be solved. Then, the adjustments on Δt sign are made based on the results from this query. The sign must change in order to sweep the $\tau(t)$ curve along the positive direction of τ. The value $\Delta t = 0$ instead is necessary to take into account those instants when g derivative, i.e. $1 - M_r$, is 0. Δt will change sign just after these instants.

Exploiting the aforementioned idea it is possible to reduce the multiple roots search to a single root search. The other roots will be obtained by sweeping τ along its "S" shaped curve, i.e. varying Δt. Furthermore it is not necessary to know the number of roots, and hence emission surface branches, a priori. The right number of roots

in the $[t_s, t_e]$ will be obtained by the sweeping process. All these features make the improved algorithm more efficient and better suited to handle both subsonic and supersonic motions.

Thus, the solution of the Retarded time equation is much faster when compared to the first order Newton-Raphson method, up to 5 times faster for high subsonic and near transonic conditions. The proposed approach has also the capability of finding multiple roots in supersonic condition without requiring the expensive roots bracketing process. This latter feature makes the algorithm efficient and less prone to failing the search.

4.2 Emission Surface construction

In the previous section was discussed the novel root finder method developed during this research. It is now necessary to define an algorithm which is capable to construct the ES of supersonically rotating sources exploiting the aforementioned method. Since the proposed root finder algorithm is designed as a retarded time approach, it is obvious that the emission surface reconstruction will be based on such approach and not on an "Advanced Time" or "Forward Time" method, [44].

In this latter process, as proposed by Brentener [44], the source time τ is set and the corresponding observer time t is calculated for each of the discrete source points. The observer time and source positions are then stored at each defined source time. The discrete data become a three-dimensional arrayindices (i, j, k) where i and j indexes describe the surface spatially while k represents the source time. The Emission surface Σ is obtained by calculating the isosurfaces of constant observer time t in the $3D$ computational space described by the matrix (i, j, k). This isosurfaces are, by definition, distinct representations of the Σ surface for a given t.

With this position the construction of Σ, proposed in [44], becomes equivalent to the problem of isosurfaces reconstruction in computer graphics. Thus, the accuracy of the results will depend on the accuracy of the isosurfaces reconstruction which is a sophisticated interpolation process to be performed both in space and in time.

On the other hand, by applying a retarded time algorithm, the retarded time equation will be solved for every point source, belonging to the starting physical surface, and considering fixed the observer time t. The corresponding single or multiple retarded positions of the original source point are then obtained. These are elements

of the final emission surface domain at the chosen time instant t.

The emission surface, using the retarded time approach, is the direct intersection between the spherical waves and the volume described by the motion of every single discretisation panel. This intersection is represented by the solution of the retarded time and retarded positions. Since the variables are calculated at an equally spaced time history, with predefined time step size, there is no need to perform the complex space and time interpolation as in [44]. Hence, for the ES construction developed during this thesis the accuracy will depend on the accuracy of the retarded time equation solver, i.e. the root finder method.

The computational time required for the direct solution of each panel emission surface could appear higher than in the forward time approach. It must be reminded though that in the latter case the effort is shifted from the solution of the retarded time to the sophisticated space and time interpolation required. Furthermore, the efficiency of the process, in the case of retarded time surface reconstruction, is heavily dependant on the efficiency of solution process of $g = 0$.

Such approaches have been considered computationally expensive because the standard root finder techniques are not well suited in the presence of multiple roots, when $M > 1$. In the current research, the overall noise prediction tool efficiency has been enhanced by exploiting the improved and more efficient root finder method described above.

The behaviour of the retarded time roots of a single source point has been clearly analysed above. In the next subsection the focus is shifted on the behaviour of a finite panel source, the basic element upon which the emission surface is build. Furthermore the analysis of the motion and behaviour of one single panel will help to highlight other key features of supersonically moving sources. It then follows a description of the Emission surface discretisation and surface integrals evaluation.

4.2.1 Single panel analysis

In figure 4.6, the (t, τ) plots for the 4 vertices of a quadrilateral panel are shown. Following the curve of point 1, along the positive observer time line, it is visible the existence of only one single root for $t < t^1_{m1}$, even if $M = 1.4$. The single root, at $t = t^1_{m1}$ is followed by the appearance of a second root, but this configuration is only existing for the specific time instant t^1_{m1} and for $t > t^1_{m1}$ there will be a third source.

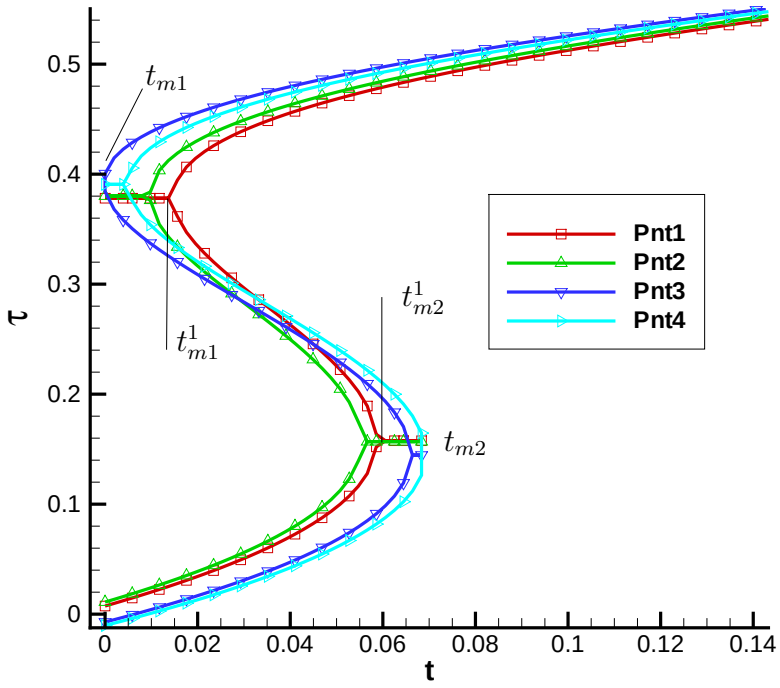

Figure 4.6: t, τ curves for a single panel with 4 points.$M = 1.4$

The appearance of this last root could be explained by assuming that the second root which appeared in $t = t^1_{m1}$ has now split into 2 different emission points: one which is moving towards the positive τ and t directions, hence by definition positive $\psi(\tau)$; and the other one moving toward negative τ direction, i.e. counter rotating with respect to the previous one.

The second root of the equation effectively rotates in opposite direction with respect to the other 2 roots, as indicated by the negative slope of the (t, τ) curve, i.e. the derivative of τ and hence ψ. To summarise, following the $\tau(t)$ curve of the panel point 1 the acoustic waves in $t < t^1_{m1}$ and $t > t^1_{m2}$ are radiated only by one emission point. On the other hand, three emission sources exist inside the interval $t_{m1} < t < t_{m2}$. It is important to highlight the existence of 2 critical points along the vertex retarded time history: $t = t^1_{m1}$ in which two coincident sources will appear in the same retarded position and $t = t^1_{m2}$ where two of the three sources will collide to occupy the same emission point and then disappear.

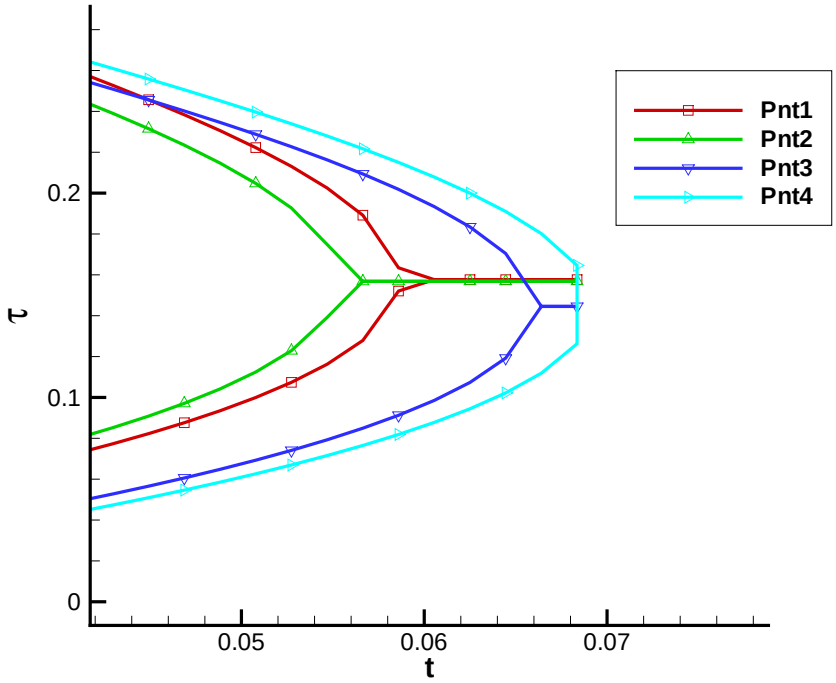

Figure 4.7: Close up of t, τ curves for a 4 points panel with $M = 1.4$

The analysis above is accurate for the single source point analysed, but for a discrete source panel a slightly different behaviour will appear. Observing the t, τ plots, fig.4.6, solution of the panel emission surface Σ_p, it is evident that the intervals in

which the multiple retarded sources appear or disappear are not the same for all the source points describing the panel, i.e. the intervals $([t^j_{m1}, t^j_{m2}], j = 1, 5)$ will be different. In this case it is possible to define the interval $[t_{m1}, t_{m2}]$, which is the union $\bigcup_{j=1}^{4}([t^j_{m1}, t^j_{m2}])$ of all the single intervals of each discretisation point.

During $[t_{m1}, t_{m2}]$ the multiple emission panels will appear and disappear as single points, i.e. two emission panels will appear in a single point when $t = t_{m1}$ and collide to a single point at the extreme $t = t_{m2}$ of the interval defined above. In Figure 4.7 it is evident that the discrete points will not have the second and third roots outside their own $[t^j_{m1}, t^j_{m2}]$, i.e. the second and third emission panels do not always preserve the same number of points of the corresponding source panel. In the figure in fact the lines at constant τ are fictitious, i.e. they have been introduced in order to preserve the panel integrity.

Based on the results of this analysis, it is clear that the emission surface construction algorithm must be capable of handling this apperance/disapperance phenomenon of the discrete vertices. By defining a method which takes into account the described behaviour, it is possible to obtain smooth emission surfaces without holes and hence, the accuracy of the numerical integrals is increased.

The main reason for the improved accuracy is that the differences between the overlapping intervals (t^j_{m1}, t^j_{m2}) is strongly dependent on the dimensions of the starting panel, i.e. on the number of points used for the discretisation of the input surface S. For finer discretisations the difference between each t^j_{m1} (or t^j_{m2}) will be lower. In Figure 4.8 are shown three panels with different dimensions demonstrating the previous statement. The blue lines indicate the base panel δS_1 while the black lines represent a panel of size $\delta S_2 = \delta S_1/4$ and the panel described by the red lines has area $\delta S_3 = \delta S_1/16$.

The differences between the τ curves of the panel's points will tend to 0 as $\delta S_i \to 0$, becoming a single source point. Thus, taking into account the described phenomenon, means accounting for the finite extension of the δS_i panels, improving the accuracy and the efficiency of the prediction tool. All the existing emission surface algorithms require mesh refinement procedures for most of the CFD input grids. The proposed algorithm will require less mesh adaptation steps because it allows the consideration of larger panel dimensions with respect to standard methods. In Figures 4.9 and 4.10 are shown the differences between two discretisations of the same quadrilateral panel, one with $2x2$ points and the other with 8×8 points. It is interesting to observe that by taking into account the phenomena described above,

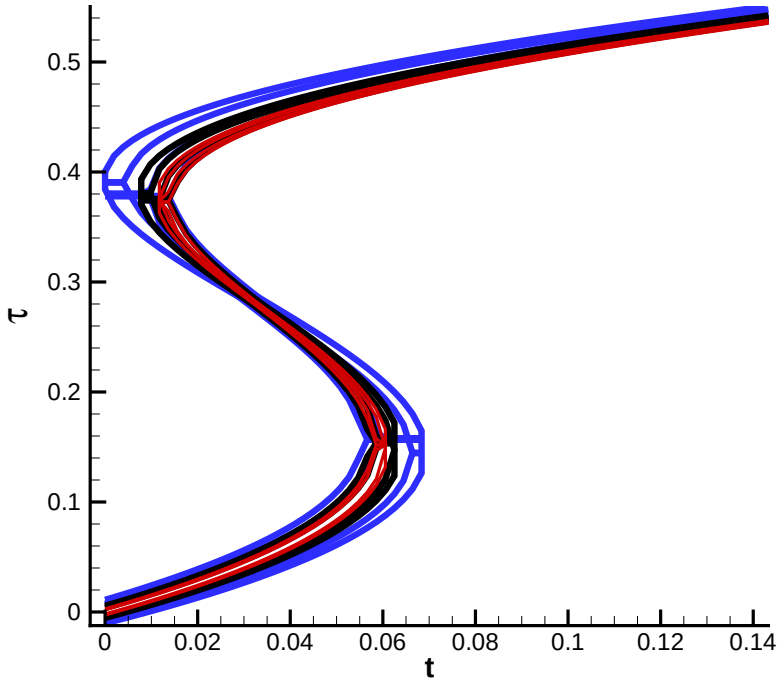

Figure 4.8: Effect of the panel size on the panel t, τ curves. (Blue lines reference size δS_1 , black lines panel size $\delta S_1/4$, red lines $\delta S_1/16$)

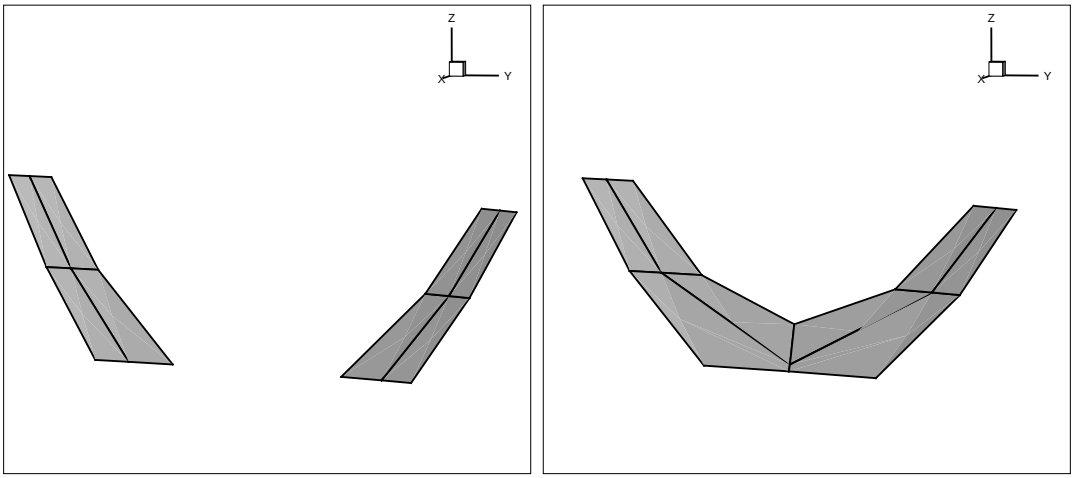

(a) *Panel* 2×2, t_1 *before collision* **(b) *Panel* 2×2, $t_1 + \Delta t$, *after collision***

Figure 4.9: Emission panels 2×2 corresponding to roots 1 and 2 during collision

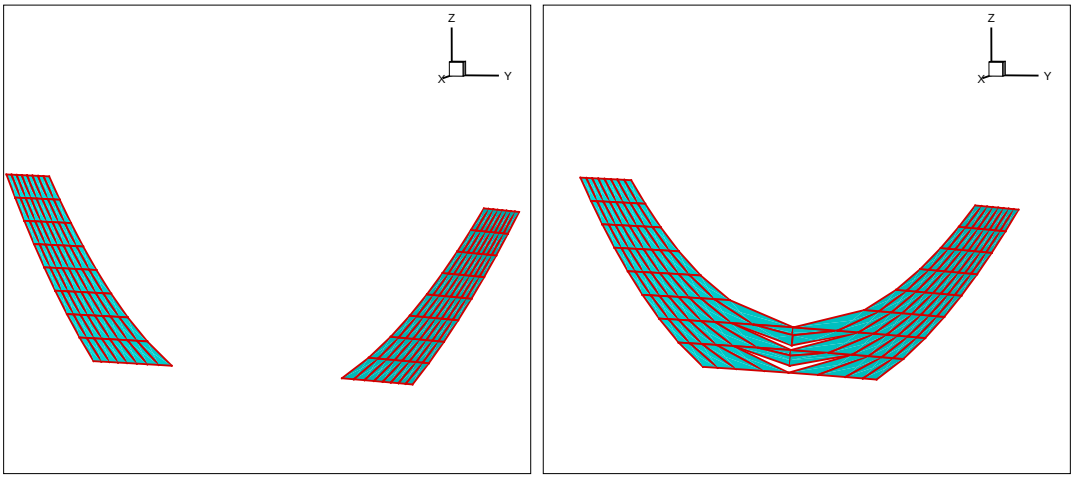

(a) *Panel* 8×8, t_1 *before collision* **(b) *Panel* 8×8, $t_1 + \Delta t$, *after collision***

Figure 4.10: Emission panels 8×8 corresponding to roots 1 and 2 during collision

the panel surface in Figure 4.9 does not show any holes during the collision of the two emission surfaces. On the other hand, even though the results in Figure 4.10 are obtained with a much larger number of discretisation points, some voids are visible between the panels. This is because the algorithm used to obtain Fig.4.10 does not take into account the finite behaviour of the discretisation panels discussed above, and does not use any interpolation or refinement in order to smooth, [47], the emission surface.

4.3 Integrals evaluation

After the description of the approaches developed for the calculation of the retarded time roots and of the corresponding retarded sources position, it is necessary to describe the integration methods used in the noise prediction tool. It must be highlighted that all aeroacoustic formulations require the evaluation of surface integrals and, for those methods which take into account the quadrupole term, also volume integrals must be computed.

A generic integration algorithm requires the surface S to be discretised in N_S panels δS_i, and the integrals are evaluated on every single δS_i and then summed. The task can be accomplished using different panel representations, i.e. using different number of points P_p which describe the panel. It is obvious that the more points are used to discretise a panel the more accurate the results obtained for both emission surface construction and noise prediction will be. The issue with this assumption is that it does not take into account computational time but only accuracy. It is better in fact to restore a balance between these two requirements, i.e. to try and have the higher accuracy possible with the lower number of points used.

Observing the physical control surface panel, in this case discretised with 5 points, in figure 4.11 and its corresponding emission surface it is clear that the a simple four points discretisation would be inadequate for an emission surface description. This is because even if the original panel could be modelled by a simple bilinear representation, it is not possible to describe the corresponding emission surface panel via a bilinear equation without loosing accuracy. The description of one panel should be obtained then using a number of points $P_p > 4$.

It should be noted that the more points are added to the panel model the more complex will be the emission surface which is possible to represent within one single panel. This allows larger dimensions for the source panels, which means less grid points and faster calculations. It must be taken into account that increasing the number of points per panel will dramatically increase the computational time for each panel, so a compromise between accuracy and efficiency should be considered also in the choice of P_p.

Brentner and Farassat in their reviews of helicopter rotor noise prediction methods,[96] and [80], identified the importance of using high order integration schemes, in order to have an efficient and robust method to resolve the aeroacoustic integral equations. Thus, a description of the integral methods which have been implemented in

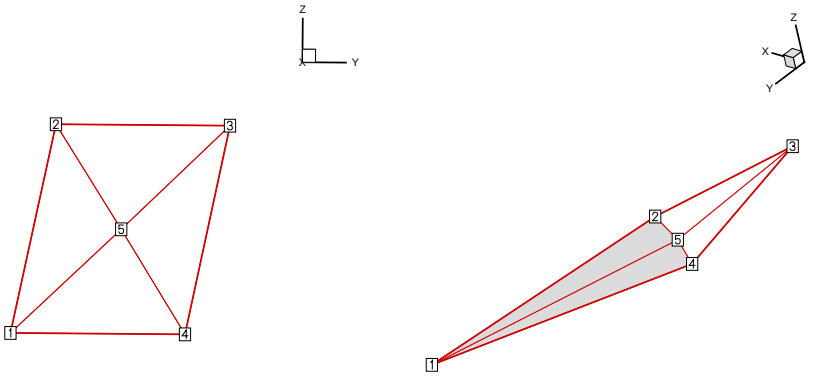

(a) ***Starting panel*** **(b)** ***Emission surface panel***

Figure 4.11: Starting and emission surface panels. $M = 1.4$

the computational tool must follow.

Many different quadrature algorithms are available. During this research three integration methods have been investigated and implemented, the Midpoint quadrature, the Simpson's method and the Gauss Legendre integration. These are in fact the most widely used and renowned integration approaches.

4.3.1 Isoparametric representation

Most integration methods could benefit from a very general panel description, which is independent from the actual panel shape or dimensions. For instance in the use of integration techniques such as Gauss-Legendre the coefficients and integration coordinates, as will be described later, are easily calculated for elements which extend from $-1, 1$ in both x and y directions.

It is useful then to describe the panels in local coordinates which vary in the interval $-1, 1$ and which are always 2 dimensional, i.e. a coordinate transformation is required from the physical space (x, y, z) to the 2D (ξ, η) space local to the panel, which is called *Reference Plane*. The (ξ, η) coordinates are called *Natural Coordinates*. The transformation between the starting coordinates of the panel , which in general are in the $\mathbf{R}^3(x, y, z)$, to the Natural coordinates requires two steps.

First the panel tangent plane and normal must be defined, using respectively the two panel's diagonals $\hat{\xi} = \overline{\mathbf{P_3P_1}}/P_3P_1, \hat{\eta} = \overline{\mathbf{P_4P_2}}/P_4P_2$ and their products $\hat{\zeta} = (\overline{\mathbf{P_3P_1}} \wedge \overline{\mathbf{P_4P_2}})/|\overline{\mathbf{P_3P_1}} \wedge \overline{\mathbf{P_4P_2}}|$, so that vertexes P_i can be described in terms of

$\hat{\xi}, \hat{\eta}, \hat{\zeta}$, and then a mapping of P_i into the ranges $-1, 1$.

In a panel can be defined actually three kinds of nodes:

- function nodes, used to store Field values;
- mapping nodes which are used to determine the element geometry with the mapping process defined above;
- nodes used for both purposes.

Elements with the same number of function and mapping nodes are called isoparametric, [97]. When an element is described using more function nodes than mapping nodes is called subparametric element, and elements with more mapping nodes than function nodes are called superparametric. The panel representations used during this thesis are only the isoparametric or iso-P elements.

Two widely used higher order quadrilateral isoparametric elements are the 8 and 9 points elements. During the development of the noise prediction tool the 9 and the 5 points quadrilateral have been implemented and tested. The former was used as a benchmark test for its high accuracy while the latter was introduced to explore the effects of adding one point, and testing whether it would enhance the accuracy of the discretisation.

The mapping described here can be generalised. The mapping nodes determine the element geometry by defining a mapping from a master element with a standard shape and position to the actual element. In order to explain more clearly the meaning of isoparametric elements it is necessary to start from the description of a simple monodimensional cell, that is a segment, with natural coordinate system such as its vertexes are -1 and 1.

Given a displacement function $u = u(\xi)$, which varies linearly inside the element, described as $u = a_1 + a_2\xi$, the two coefficients can be easily found by imposing that $u(\xi = -1) = u_1$ and $u(\xi = 1) = u_2$. This leads to the equation for u:

$$u(\xi) = u_1 \frac{(1-\xi)}{2} + u_2 \frac{(1+\xi)}{2} \tag{4.28}$$

That is:

$$u(\xi) = \sum_{k=1}^{P_p} u_k \Phi_k \tag{4.29}$$

With the above relations it is then possible to obtain the shape functions for the linear isoparametric element:

$$\Phi_1 = \frac{(1-\xi)}{2} \tag{4.30}$$

$$\Phi_2 = \frac{(1+\xi)}{2} \tag{4.31}$$

which must respect the following condition:

$$\sum_{k=1}^{P_p} \Phi_k \;\; = \;\; 1 \tag{4.32}$$

A generic point along the segment $x_1 \leq x \leq x_2$ is represented by:

$$x = x_1\Phi_1 + x_2\Phi_2 = \sum_{k=1}^{P_p} x_k\Phi_k \tag{4.33}$$

These three relations, eqq.4.32,4.33,4.29, can be put into a matrix form:

$$\begin{pmatrix} 1 \\ x \\ u \end{pmatrix} \;\; = \;\; \begin{pmatrix} 1 & 1 \\ x_1 & x_2 \\ u_1 & u_2 \end{pmatrix} \begin{pmatrix} \Phi_1 \\ \Phi_2 \end{pmatrix} \tag{4.34}$$

Applying the same steps for the $2D$ quadrilateral element represented by $P_p = 4$ points the following matrix is obtained:

$$\begin{pmatrix} 1 \\ x \\ y \\ u \\ v \end{pmatrix} \;\; = \;\; \begin{pmatrix} 1 & 1 & 1 & 1 \\ x_1 & x_2 & x_3 & x_4 \\ y_1 & y_2 & y_3 & y_4 \\ u_1 & u_2 & u_3 & u_4 \\ v_1 & v_2 & v_3 & v_4 \end{pmatrix} \begin{pmatrix} \Phi_1 \\ \Phi_2 \\ \Phi_3 \\ \Phi_4 \end{pmatrix} \tag{4.35}$$

Where the shape functions Φ_i can be calculated assuming a bilinear function $\Phi_i = c_i(1+\xi_i\xi)((1+\eta_i\eta))$ and ξ_i, η_i are the natural coordinates of the point P_i. The coefficients c_i can be found by imposing that Φ_i must be equal to 1 at the point i

plus the condition $\sum_{k=1}^{P_p} \Phi_k = 1$. This brings to the following shape functions:

$$\begin{pmatrix} \Phi_1 \\ \Phi_2 \\ \Phi_3 \\ \Phi_4 \end{pmatrix} = \begin{pmatrix} \frac{1}{4}(1-\xi)(1-\eta) \\ \frac{1}{4}(1+\xi)(1-\eta) \\ \frac{1}{4}(1+\xi)(1+\eta) \\ \frac{1}{4}(1-\xi)(1+\eta) \end{pmatrix} \tag{4.36}$$

Only the shape function for the 5 nodes panel will be presented here:

$$\Phi_i = \frac{1}{4}(1+\xi_i\xi)(1+\eta_i\eta) - \frac{1}{4}(1-\xi^2)(1-\eta^2) \tag{4.37}$$

where $(i = 1, 4)$ and

$$\Phi_5 = (1-\xi^2)(1-\eta^2) \tag{4.38}$$

It is clear now, from these equations, that the mapping nodes of the master element are mapped to the nodes of the actual element. All the other points are mapped by using the mapping nodes' shape functions for interpolation, e.g. in the case of the $1D$ segment a generic point x is found as $x = \sum_{k=1}^{P_p} x_k \Phi_k$. Using the iso-P representation all the scalar and vector fields can be modelled using the element's shape functions, for instance the pressure $P(x, y, z)$ can be written, knowing the pressure $P(x_i, y_i, z_i)$ on the element's points, after the isoparametric mapping, as:

$$P(\xi, \eta) = \sum_{k=1}^{P_p} P_k \Phi_k \tag{4.39}$$

And the same procedure is valid for each component of a vector field.

4.3.2 Mid-point quadrature

Using the midpoint quadrature, the discretised version of the generic retarded-time integral, defined in eq.4.1, can be written as follows:

$$4\pi\Phi(\mathbf{x}, t) \approx \sum_{i=1}^{N_p} \left[\frac{Q(\mathbf{y_c}, t - r_c/c_0)}{r_c^{\alpha_1} |1 - M_r|_c^{\alpha_2}} \right]_{ret} A_{S_i} \tag{4.40}$$

Where the integrand is evaluated at the centre of each panel, $\mathbf{y_c}$, and at the retarded time $\tau_c = t - r_c/c_0$ at this point. Because the source strength, Q, is evaluated at τ_c which, in general, is not one of the input data time instants, temporal interpolations

are required.

Mid-point quadrature is the most exploited method for integrals evaluations, especially when the integrand inputs are available only in the centre of the panel. The method is very fast, and it consists of applying the simple geometrical rule for which the area of a quadrilateral is give by the vector product:

$$\mathbf{A_{S_i}} = \mathbf{P_1P_2} \times \mathbf{P_1P_3} \tag{4.41}$$

which represents the normal vector to the panel surface with a magnitude equal to the panel area:

$$A_{S_i} = \sqrt{\mathbf{A_{S_i}} \cdot \mathbf{A_{S_i}}} \tag{4.42}$$

An improved version of the mid-point quadrature can be obtained if the two diagonals of the panel are used, in the vector product, instead of the two edges. By doing this in fact the formula will be accurate even for highly skewed and non symmetrical panels. The accuracy is improved because in the standard method the use of 2 edges does not take into account the position of the fourth point of the panel, which is included when using the diagonals.

4.3.3 Simpson's quadrature

The accuracy of the midpoint algorithm is second order, since the integrand quantities are approximated with a constant distribution at the centre of the panel. By replacing the single point evaluation of the integrand at the panel centre with multi-point methods the accuracy of the variables distribution can be improved:

$$4\pi\Phi(\mathbf{x},t) \approx \sum_{i=1}^{N_p}\sum_{k=1}^{N_{Sim}} \left[a_k \frac{Q(\mathbf{y_k}, t - r_k/c0)}{r_k^{\alpha_1}|1 - M_r|_k^{\alpha_2}}\right]_{ret} |J_k| A_{S_i} \tag{4.43}$$

where a_k and $|J_k|$ are the quadrature weight coefficient and determinant of the Jacobian of the transformation, respectively, for the k^{th} point in the panel quadrature algorithm. In particular for the Simpson's quadrature approximation, the general numeric discrete formula of the integral is:

$$\sum_{i=1}^{N_p}\sum_{k=1}^{N_{Sim}} \left[a_k \frac{Q(\mathbf{y_k}, t - r_k/c0)}{r_k^{\alpha_1}|1 - M_r|_k^{\alpha_2}}\right]_{ret} \frac{1}{\sum_k = 1_{Sim}^N a_k} |J_k| A_{S_i} \tag{4.44}$$

where t is one observer time instant, and, for $N_{Sim} = 9$:

- $\mathbf{y_1} \dots \mathbf{y_4}$ are the vertexes of the Quadrilateral Panel
- $\mathbf{y_5} \dots \mathbf{y_8}$ are the edges midpoints
- $\mathbf{y_9}$ is the panel centre

The corresponding coefficients a_i are: $a_1, \dots, a_4 = 1$,$a_5, \dots, a_8 = 4$,$a_9 = 16$. It is then clear that, while for the midpoint quadrature is required only the value at the panel central point, for the Simpson's quadrature $N_{Sim} = 9$ on the same panel, are required the source information on 9 points. Hence, the Simpson's quadrature is more accurate but also more computationally expensive.

4.3.4 Gauss-Legendre quadrature

Gauss-Legendre quadrature is the method of choice when high accuracy is required in the integrals evaluation. In fact, with this method high accuracy can be reached with a relatively low number of points compared to the aforementioned quadrature algorithms. It is useful to introduce this method first in a one dimensional example. Given a function $y = f(x)$ in which $-1 \leqslant x \leqslant 1$, it is possible to evaluate its integral $\int_{-1}^{1} yudx$ more accurately than the Simpson's rule. The basic idea is to use 2 function evaluations as in the Simpson's rule, but by choosing the evaluation point in a sophisticated manner. The 2 point Gauss rule is based on the following idea:

$$\int_{-1}^{1} f(x)\mathrm{d}x \;=\; w_1 f(x_1) + w_2 f(x_2) \tag{4.45}$$

The approximating formula can be made exact for a cubic polynomial $\Pi(x) = a_3x^3 + a_2x^2 + a_1x + a_0$ by exploiting the four coefficients w_1, w_2, x_1, x_2. To compute the coefficients it is required the solution of 4 equations obtained by imposing the following conditions on the integral:

$$f(x) = 1 \quad \int_{-1}^{1} 1\mathrm{d}x = 2 \quad w_1 + w_2 = 1 \tag{4.46}$$

$$f(x) = x \quad \int_{-1}^{1} x\mathrm{d}x = 0 \quad w_1x_1 + w_2x_2 = 0 \tag{4.47}$$

$$f(x) = x^2 \quad \int_{-1}^{1} x^2\mathrm{d}x = \tfrac{2}{3} \quad w_1x_1^2 + w_2x_2^2 = \frac{2}{3} \tag{4.48}$$

$$f(x) = x^3 \quad \int_{-1}^{1} x^3\mathrm{d}x = 0 \quad w_1x_1^3 + w_2x_2^3 = 0 \tag{4.49}$$

The solution of this system leads to the values of Gauss-Legendre two point rule:

$$w_1 = w_2 = 1 \qquad -x_1 = x_2 = \tfrac{1}{\sqrt{3}} \tag{4.50}$$

$$\int_{-1}^{1} f(x)\mathrm{d}x = \int_{-1}^{1} f(-\tfrac{1}{\sqrt{3}}) + f(\tfrac{1}{\sqrt{3}})\mathrm{d}x \tag{4.51}$$

Using the same procedure, with a chosen number of point N in the interval, it is possible to obtain the weight and abscissas for the N_{th} point G-L rule. The general N-point rule is:

$$\int_{-1}^{1} f(x)\mathrm{d}x = G_N(f) = \sum_{k=1}^{N} w_{N,k} f(x_{N,k}) \tag{4.52}$$

and the accuracy for the rule is of order of $2N-1$, i.e. the approximation is exact for a polynomial of order $2N-1$. The main issue with the formula is that the weights w_i and positions x_i are known only for standard elements which extends in the range $-1, 1$. This can be solved using the isoparametric representation described before. In particular for a generic segment x_i, x_{i+1} the Gauss-Legendre rule can be written, exploiting and iso-P segment, as:

$$\int_{x_i}^{x_{i+1}} F(x)\mathrm{d}x = \int_{-1}^{1} F[x(\xi)]J\mathrm{d}\xi = G_N(f) = \sum_{k=1}^{N} w_{N,k} F[x(\xi_{N,k})]J_{N,k} \tag{4.53}$$

The Jacobian J for the $1D$ linear element it is equal to:

$$J = \left\| \frac{\partial x}{\partial \xi} \right\| \tag{4.54}$$

From the properties of the iso-P elements $x = \sum_{i=1}^{Nod} x_i S_i$, which gives the value of $\frac{\partial x}{\partial \xi}$:

$$\frac{\partial x}{\partial \xi} = \sum_{i=1}^{Nod} x_i \frac{\partial}{\partial \xi} S_i(\xi) \tag{4.55}$$

The extension to more than one dimension is straight forward. In particular, for a

panel δS_i, the generic $2D$ Gauss rule of order $(2N_\xi - 1) \times (2N_\eta - 1)$ is:

$$\int_{S_i} F(x,y)\mathrm{d}S_i = \int_{-1}^{1}\int_{-1}^{1} F(\xi,\eta)|J|\mathrm{d}\xi\mathrm{d}\eta = \sum_{k_\eta=1}^{N_\eta}\sum_{k_\xi=1}^{N_\xi} w_{N_\xi,k_\xi} w_{N_\eta,k_\eta} |J_{N_\xi,N_\eta}| F(\xi_{N_\xi,k_\xi}, \eta_{N_\eta,k_\eta}) \tag{4.56}$$

It has to be noted that, in eq.4.56, the Jacobian, the weights and the abscissas for each element depend on the choice of the number of points N_ξ, N_η in Gauss-Legendre (G-L) rule along the ξ and η directions.

It is clear that the G-L quadrature is very accurate, but even in this case the iso-P mapping, the calculation of weights and abscissas and the evaluation of the integrands over the N_G points make this algorithm much more computationally expensive than the midpoint quadrature. An adaptive multi-point quadrature would be the optimum choice, this could be done using the midpoint quadrature approximation in non-sensitive regions, i.e. the zones with low gradients, while exploiting a multi-point rule only over the sensitive regions of the control surface.

The highest efficiency and accuracy quadrature can be realized with a solution-adaptive multi-point quadrature scheme. With this scheme the number of quadrature points used for a panel depends on some characteristics of the solution. In particular the solution adaptive method proposed by Brentner et al., [80], defines the number of quadrature points N_q over each panel using the following relation:

$$N_q(M_r, A_{S_i}) \propto \frac{A_{S_i}}{|1 - M_r|_i} \tag{4.57}$$

That is N_q is directly proportional to the area of the panel, i.e. larger panel will require more points. And inversely proportional to $1 - M_r$ over the panel, i.e. near transonic panels, whose radiation much number is closer to one, will require more points. Such schemes can provide high accuracy and minimise the computational effort.

4.3.5 Integrals for Emission panels

The quadrature methods described above are certainly applicable for retarded time formulations but in the case of Emission Surface their requirements of multiple evaluation of the integrands yields a high computational cost. In this case a better

option would be to use the midpoint quadrature. A further improvement to the diagonals midpoint quadrature has been developed during this research, by considering a 5th point on the panel. This point is used to describe the centre of the panel and with its introduction it is possible to divide the panel surface in 4 triangles namely $Tr_1 = P_1P_2P_5, Tr_2 = P_2P_3P_5, Tr_3 = P_3P_4P_5, Tr_4 = P_4P_1P_5$.

The triangles can then be used to calculate the overall panel area by means of the simple vector product of the triangle edges:

$$Tr_{1_{S_i}} = \frac{|\mathbf{P_5P_1} \wedge \mathbf{P_5P_2}|}{2} \tag{4.58}$$

And the total panel area A_{S_i} will then be:

$$A_{S_i} = \sum_{k=1}^{4} Tr_{k_{S_i}} \tag{4.59}$$

In this way, the accuracy of the midpoint quadrature is improved since the emission panel it is not anymore considered to lay on one plane. In fact, in figure 4.11 is visible that the emission surface panel does not lay on one plane. The interesting characteristic of this scheme is that it requires only the calculation of one more point with respect to the classical midpoint algorithm, but can handle much more complex emission surface representations.

4.4 Summary and conclusions

In this Chapter, a detailed analysis of the numerical models implemented and developed during this study have been presented. The helicopter rotor kinematics and the behaviour of the retarded time equation roots have been analysed in detail. From these analyses some ideas for the development of a "tailored" root finder algorithm and emission surface construction are suggested.

A particular focus is given to the development of a novel root finder algorithm which is based on the Newton's method. More precisely in the proposed algorithm the function is approximated via a 3^{rd} order Taylor series as opposed to the 1^{st} order Taylor series of the Newton's method. The corresponding polynomial is then solved via the Nickalls method. This is a solution of the 3^{rd} order polynomials similar to the Cardano solution.

Using the aforementioned root finder algorithm and from the considerations on both kinematics and retarded time equation the Emission Surface construction approach is developed. The approach is tested on the case of a rotating panel. Finally, the quadrature methods implemented in the noise prediction tool are discussed.

Chapter 5

Verification and Validation

Any new computational tool must undergo through the verification and validation processes. The verification process is required in order to establish that the code solves the implemented equations correctly, Roache [98]. The validation process, instead, is required to demonstrate whether the code solves the right equations. In the current Chapter both steps are applied to the noise prediction tool developed during this research.

The algorithm described in Chapter 4 can be divided into four components: root finder algorithm, quadrature, kinematics and emission surface reconstruction. Each component of the tool will be tested separately in order to identify that the equations have been implemented correctly and the algorithm is capable of providing a correct solution for each of these parts.

The verification and validation should be ideally carried out by comparing the results to analytical solutions of the governing equations. In this way the numerical errors are directly obtained through the comparison between the two solutions. Such analytical solutions though, are available only for some specific cases which do not allow testing the full capabilities of the code. In the present analysis, the core of the testing process for the aeroacoustic prediction is based on the analytical solutions of the 3D monopole, dipole and quadrupole sources.

The analytical expressions of these sources can be obtained from the solution of the Helmholtz equation in spherical coordinates, as will be described later. The solution though is easily available only for stationary sources and observer positions. This is useful to test the quadrature algorithms and the differences between the predictions of Farassat Formulations 1, eq.3.38, and 1A, eq.3.40,3.41. However, it should be

noted that for stationary sources and observers the retarded time formulation and Emission surface formulation coincide.

On the other hand, the root finder algorithms, kinematics and emission surface construction will be tested for moving sources both in subsonic and transonic-supersonic regimes. The next section presents a comparison of the root finder algorithms for the solution of the retarded time equation.

5.1 Comparison of Root finder algorithms

The importance of a fast and efficient method to obtain the roots of the retarded time equation has been highlighted in the previous Chapter. The proposed novel root finder method, is described in Section 4.1.3. In the following subsections the root finder algorithm is compared with the classical Newton's and Brent's algorithms in order to verify the relative efficiency and computational cost. Given the different behaviour of the retarded time roots in subsonic and supersonic regimes, the analysis will consider both regimes.

A rotating point source, or panel, represents an optimum case for comparing the performance of each of the different root finder methods. Considering a point P_1 which is in a Reference Frame RF rotating with respect to the ground fixed frame, the kinematics of P_1 can be described with the equation:

$$\mathbf{r} \;=\; (\mathbf{x_{OB}} - ([T_{GR}])\,\mathbf{y_{P_1}}) \tag{5.1}$$

Which is obtained by assuming $\mathbf{V_H} = \mathbf{V_{OB}} = \mathbf{0}$ in eq.4.8 and by considering only the rotational motion of P_1.

Although the above equation is much simpler with respect to the complete eq.4.5, it is still not possible to obtain an analytical solution for $g(t, \tau, r) = 0$.. For this reason, the results from the different root finder algorithms must be compared with the numerical solution obtained via a forward time approach.

The forward time equation, $t(\tau)$ can easily be solved numerically, and in the case of a stationary observer it is also possible to obtain an analytical solution for $t(\tau_{g=0})$. Hence, the forward or "advanced" time numerical solution, could be considered equivalent to the analytical solution of $\tau(t)$, through the solution of the inverse problem $t(\tau)$.

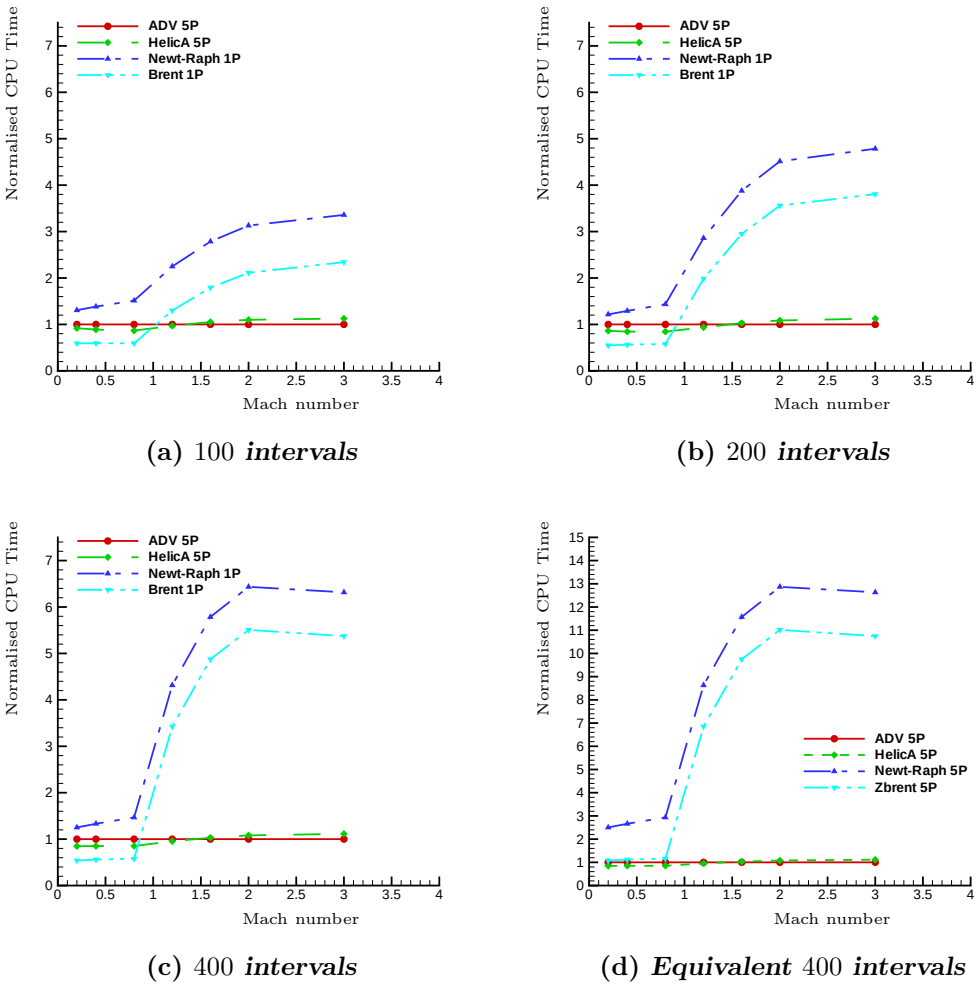

(a) 100 ***intervals*** **(b)** 200 ***intervals***

(c) 400 ***intervals*** **(d)** ***Equivalent*** 400 ***intervals***

Figure 5.1: Comparison of CPU times with different root finder algorithms, figures are shown with different number of intervals for the bracketing step required by Brent and Newton methods (the time is normalised dividing by the CPU time of the "ADVanced" time solution; 1P and 5P indicates the number of points per panel. Equivalent indicates that all the codes solve 5P per panel)

Fig.5.1 illustrates the computational cost for each approach considered for the solution of rotating panels. The Mach number is evaluated at the centre of the panel and the computational time is normalised dividing by the computational time of the Advanced Time solution. The variation in Mach number is obtained by increasing the rotational speed ω. The number of intervals which is specified in Figure 5.1 represents the number of sub-intervals used in the bracketing step. This step is a requirement of the two classic methods, and while in subsonic conditions only 2 sub-intervals are used for both methods, during supersonic regime the number of interval must be 2 orders of magnitude larger.

The computational time, plotted in Fig.5.1, refers to the solution of 500 panels. This is necessary in order to capture the average solution time for each algorithm. By considering 500 configurations the solution time will not be dependent on the particular panel geometry or observer position.

Observing the plots in subsonic regime, it is clear that all the algorithms require a similar computational time. Under these conditions, the Brent's algorithm provides the faster solution, but it should be highlighted that both Newton and Brent's methods consider only the panel centre in the solution. This is reported in the legend of Fig.5.1 with 1P, i.e. 1 point per panel. On the other hand the "Advanced Time" and the HelicA algorithms were executed considering 5P points per panel, the centre and the four panel vertices.

In Fig.5.1(d) the Newton's and Brent's algorithms were executed resolving the same number of points per panel as the other two methods. In this case it is clear that also in subsonic regime the novel root finder algorithm performs faster than the classical methods. The computational time for this latter approach is comparable to the Advanced Time algorithm.

A more complex challenge arises when the sources are in supersonic motion, due to the existence of multiple retarded times τ and positions $\mathbf{y}(\tau)$ corresponding to a single point source $\mathbf{y}_0$ and observer time t. This increased complexity is visible in Fig.5.1, where a steep gradient and a sudden increase in computational time is evident in the curves representing the two classical methods for $M \approx 1$. This is due to the increase in the number of bracketing sub-intervals which is required in order to find all the multiple roots for a given observer time. The computational time increases proportional to the number of sub-intervals considered.

When a low number of sub-intervals is used during the bracketing step, the solutions obtained with the Newton's and Brent's algorithms do not capture the multiple τ

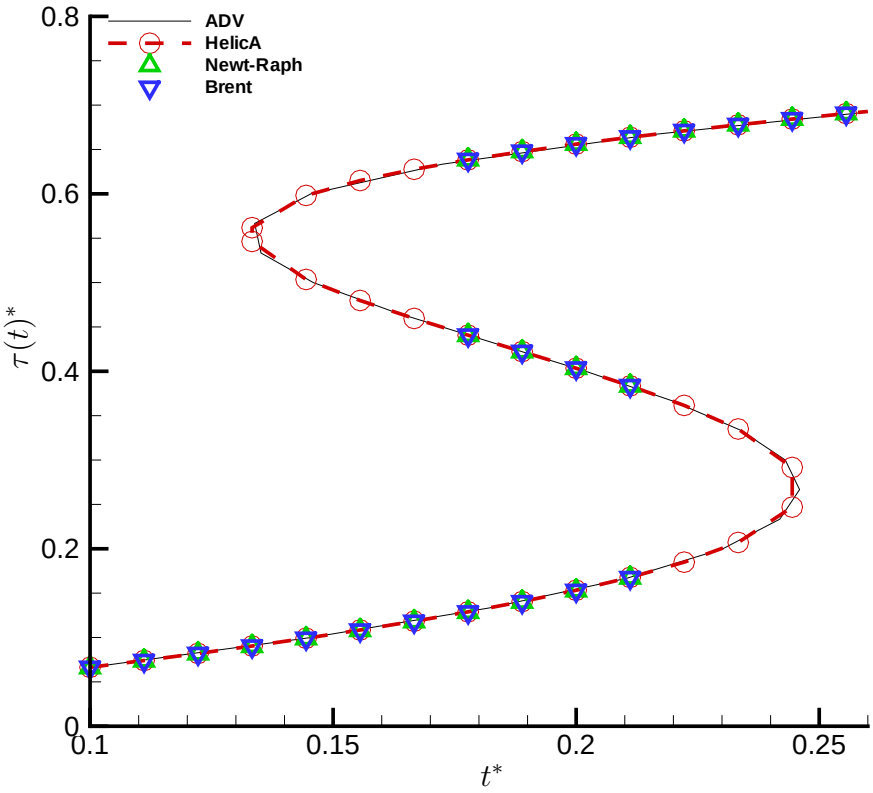

Figure 5.2: Solution of $\tau(t)$ via different root finder algorithms, $M = 1.6$ (non dimensional $t^* = (t - t_0)/T$ and $\tau^* = (\tau - \tau_0)/T$)

roots for all the different Mach numbers. Hence, increasing the number of sub-intervals in the bracketing step has a positive effect on the search of multiple roots. In Fig. 5.1, only the calculations performed with 400 sub-intervals could provide the multiple roots for all the supersonic conditions.

On the other hand the Advanced Time and the root finder algorithm proposed in the present study do not show a strong dependance on the Mach number. The computational time required by the latter method remains almost constant and around 10 to 20% higher with respect to the time required by the Advanced Time algorithm.

Considering a direct comparison between the HelicA root finder and the two classical methods, is evident the much higher computational time that is required by the latter two approaches, , more than 5 times. Furthermore, in Fig.5.2 is clear that both Newton's and Brent's algorithms do not capture the full range of multiple roots

τ, while the proposed algorithm follows closely the Advanced Time prediction. The two classical algorithms fail to identify the roots close to the local minimum and maximum of the inverse function $t(\tau)$, where the roots become so much close to each other that they fall in the same sub-interval of the bracketing step. A possible solution to this problem could be to deploy an even finer sub-interval bracketing step, which in this case was executed with a value of 400 sub-intervals.

5.2 Comparison with analytical solutions

The monopole, dipole and quadrupole sources are generated respectively by the fluctuations of mass fluxes, forces and stresses in an unsteady flow field. These sources can be considered as the basic components of a more general and complex aerodynamic source. Only 3D linear monopole, dipole and quadrupole sources are considered in the present Chapter. A source is considered linear when the particle displacement of the fluid near the source is $d << \lambda$, where λ is the wavelength of the propagating fluid properties fluctuations, i.e. the source is compact with respect to λ. A more precise definition of compact source can be obtained by considering the typical time scale τ of the flow under analysis, or the frequency Ω and length scale L in the problem.

$$He = \frac{L}{c_0 \tau} \tag{5.2}$$

Also $He = \frac{\Omega L}{c_0} = \frac{2\pi L}{\lambda} = kL$. The dimensionless number He is called the Helmholtz number and for compact sources it is easy to demonstrate that $He << 1$.

The analytical solutions of 3D monopole, dipole or quadrupole sources have been used in the present research to verify and validate the numerical errors induced by the spatial and temporal discretisation and by the integration algorithms. A 3D monopole can be identified with a pulsating sphere as the small sphere in Fig.5.3. In this Figure, the Control Surface is shown, which in this case is a large sphere of radius r_s containing the sources. The small pulsating sphere produces a volume flux in the near-field and a sound pressure wave in the far-field, which are uniform in all directions. More precisely, a pulsating sphere can be called monopole only if it is compact and hence can be approximated as a point source, i.e. a monopole.

The pressure fluctuations generated by a small pulsating sphere can be represented

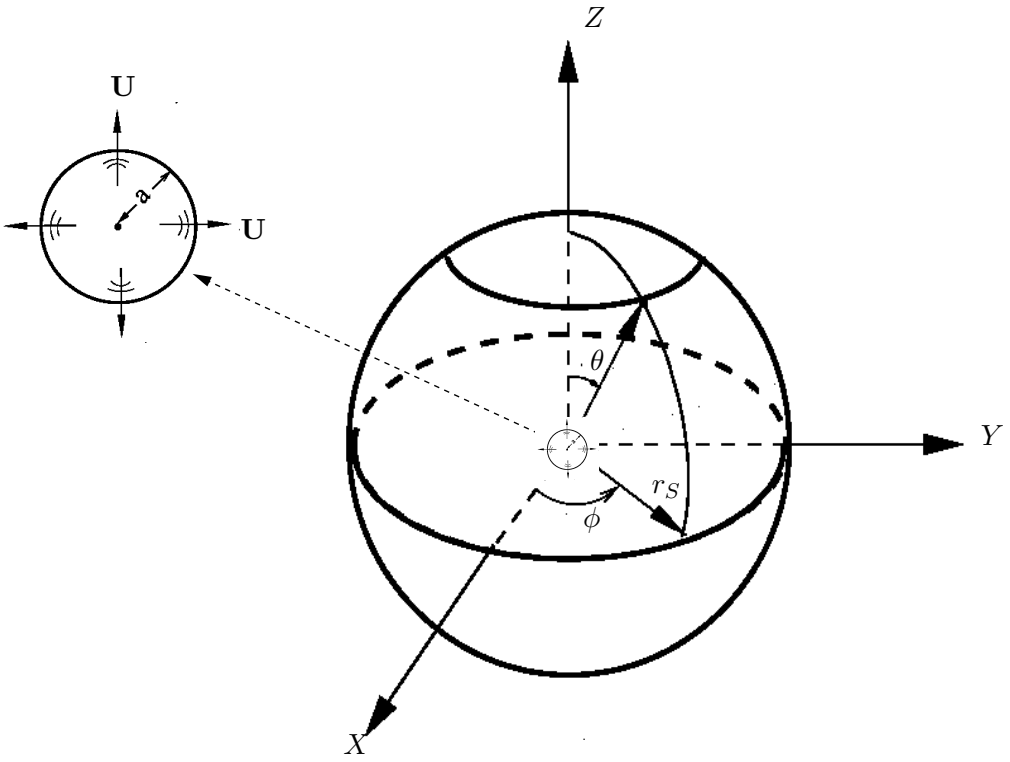

Figure 5.3: Monopole source and Control Surface

by an harmonic spherical wave,

$$\hat{p} = A\frac{e^{j(\omega t - kr)}}{r} \tag{5.3}$$

which is a solution for the Helmholtz equation in spherical coordinates:

$$\frac{\partial^2 r\hat{p}}{\partial r^2} + k^2\hat{p} = 0 \tag{5.4}$$

and $\hat{u_r}$ from the Euler equation is:

$$\hat{u_r} = -\frac{1}{j\omega\rho}\frac{\partial\hat{p}}{\partial r} \tag{5.5}$$

After some considerations on the sphere dimensions and position, the analytical equations for the pressure fluctuations induced by a pulsating sphere is:

$$\hat{p} = \frac{j\rho\omega Q e^{j(\omega t - k(r-a))}}{4\pi r(1+jka)} \tag{5.6}$$

and $\hat{u_r}$ is easily found by Eq.5.5. Where $Q = 4\pi a^2 U$, a is the radius of the pulsating sphere and ω and k are respectively the angular velocity and the wave number of

the fluctuations.

It is evident from Eq.5.6 that, for a very small sphere $He = ka << 1$, the pressure fluctuation $\hat{p}$ becomes

$$\hat{p} = \frac{j\rho\omega Q e^{j(\omega t - kr)}}{4\pi r} \tag{5.7}$$

which is the expression for a monopole with volume velocity $Qe^{j\omega t}$.

Once the concept of monopole and its model are defined, it is easy to model the other two sources, dipoles and quadrupoles, by considering respectively two or four monopoles. More precisely, it is possible to approximate a dipolar point source or 3D dipole by considering two closely positioned compact oscillating spheres, with opposite fluctuation phases. The axis of the dipole is defined as the line connecting the centres of the two nearby monopoles.

Proceeding in a similar fashion, a combination of two very closely positioned compact dipolar sources forms a 3D quadrupole. Given the number of combined monopoles or dipoles, more degrees of freedom are available. It is possible to obtain different quadrupoles altering the spatial disposition of the basic components. It is common to classify the quadrupoles in two types: lateral and longitudinal quadrupoles.

In the longitudinal quadrupole the separation between the combined dipoles is along the direction of their axes, i.e. the four monopoles are aligned. The separation between the two dipoles, for a lateral quadrupole, is perpendicular to the axis of the dipoles. This latter type of quadrupole source will be considered during the verification process.

The FW-H integral formulations satisfy non-reflecting outgoing far-field boundary conditions, so that the numerical errors in algorithms implementing such kind of integral formulations are mainly caused by the spatial and temporal discretisations. These errors should converge to zero as the spatial and temporal resolutions tend to infinity. In the present analysis, the spatial and temporal discretisation errors are decoupled using the following procedures.

The integrand terms in the FW-H formulations, eqq.3.38,3.40 and eqq.3.41, 3.51, depend both on retarded time τ and observer position $\mathbf{x}$. In order to avoid the time discretisation errors all the integrands time histories and time derivative are calculated analytically at each panel position. In this way the input information on the control surface is continuous in time, and the surface integrations are affected

only by the spatial discretisation and numerical quadrature errors.

The average error, ε_{av} is defined as follows and is used as a comparison measure:

$$\varepsilon_{av} = \frac{\sum_{i=1}^{Nt}\sum_{j=1}^{Nx}|(P(\mathbf{x}_j,t_i)-P_A(\mathbf{x}_j,t_i))|}{\sum_{i=1}^{Nt}\sum_{j=1}^{Nx}|P_A(\mathbf{x}_j,t_i)|} \tag{5.8}$$

where $P(\mathbf{x}_j,t_i)$ and $P_A(\mathbf{x}_j,t_i)$ represent respectively the numerical and analytical solutions of sound pressure at the observer position, $\mathbf{x}_j$, and at the observer time, t_i . Nx and Nt are respectively the total number of the observation points and times. It is clear that ε_{av} is the error averaged over all the observer positions and all the observation times.

Once the spatial discretisation error, which is labelled as ε^s_{av}, is quantified, the calculations are performed using discrete time histories for the integrands and their derivatives. The integrand time histories are calculated via the analytical solution for several discrete retarded time values and stored in an array. During the calculations the required integrand values for a given retarded time τ, are interpolated from the discrete array and the derivatives are calculated numerically.

In this way, the total discretisation error ε_{av}, i.e. spatial and temporal, is obtained and the temporal discretisation error, ε^t_{av}, can be calculated as $\varepsilon^t_{av} = \varepsilon_{av} - \varepsilon^s_{av}$.

A parametric study was undertaken to understand the behaviour of the prediction tool for different discretisation levels. The values of the parameters chosen for the analytical sources are :

a [m]	d [m]	U_n $[\frac{m}{s}]$	r_s [m]	ω $[\frac{rad}{s}]$	c_0 $[\frac{m}{s}]$	ρ $[\frac{kg}{m^3}]$
0.005	0.025	35.0	0.6	3π	340	1.1825

Table 5.1: Initial parameter values of the analytical sources

The source is surrounded by a control surface of radius r_s, over which the FW-H integrals are evaluated. The pressure and velocity values over this control surface are obtained from the analytical solution. The Mach number $M_n = U_n/c_0$, at which the pulsating spheres contract and expand, is $M_n \approx 0.1$. The parameters a, d, ω are respectively the radius of the pulsating spheres, the distance between the centres of 2 pulsating spheres and the angular velocity at which the spheres pulsate. The chosen observer positions were distributed evenly along a circle surrounding the source, with a resolution of 4°, i.e. 90 points per circle, and at a distance of $r_{ob} = 40m$ from the source position.

Three parameters were varied during the study: r_s, ω and the number of points used to discretise the control surface. More precisely the following values have been considered: $(r_s = 0.6, 1.2, 2.4, 4.8)$ and $(\omega/(2\pi) = 3, 5, 15, 30, 60, 120, 240, 360)$. These values of ω still preserve the linearity of the source since the maximum $He \approx 0.005 << 1$

In order to discretise the control surface, 4 different grid resolutions have been chosen. The number of nodes used are $(I_{max} \times J_{max}) = (16 \times 14), (24 \times 22), (48 \times 46), (88 \times 86)$, which are evenly distributed along the sphere. The computational grid was created analytically using a mapping between polar and rectangular coordinates and patching the singularity points, i.e. the two vertices on top and bottom of the sphere, with two "spherical rectangles". This kind of discretisation is illustrated in Fig.5.4.

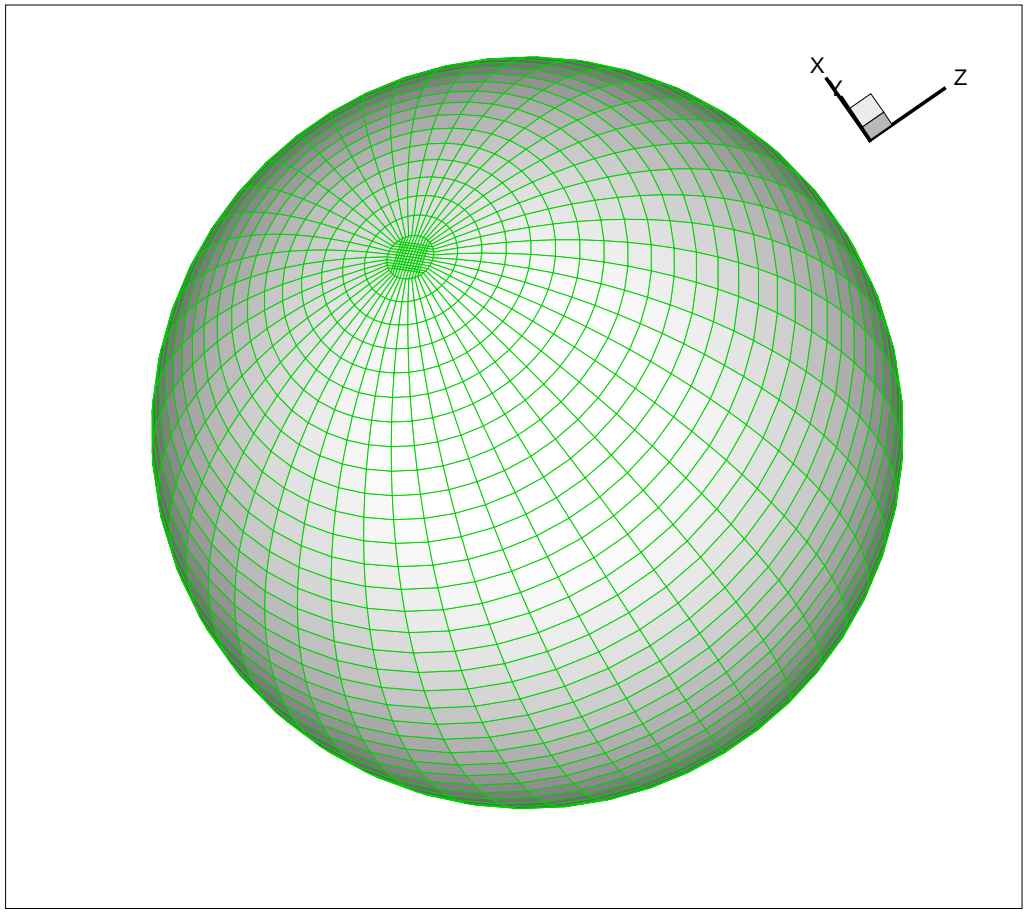

Figure 5.4: Discretisation of the Control surface

The following non-dimensional parameters were defined to classify the grid resolution. These are the largest panel's angle, $\Delta\theta_{max}$, which is proportional to level of

discretisation of the sphere and becomes large for coarse grids; the largest panel diagonal length, $\Delta L_{max} \propto \Delta\theta_{max} \cdot r_s$ which is divided by the characteristic wavelength of the source, λ_s; and the radius of the control surface, r_s/λ_s, which is nominated with the characteristic wavelength. It should be noted that only two of these three non-dimensional parameters are independent, since having set two of them the third one is also defined. The $\Delta\theta_{max}$ values which correspond to the number of nodes defined above are in order: $\Delta\theta_{max} = 25°, 16°, 8°, 4°$.

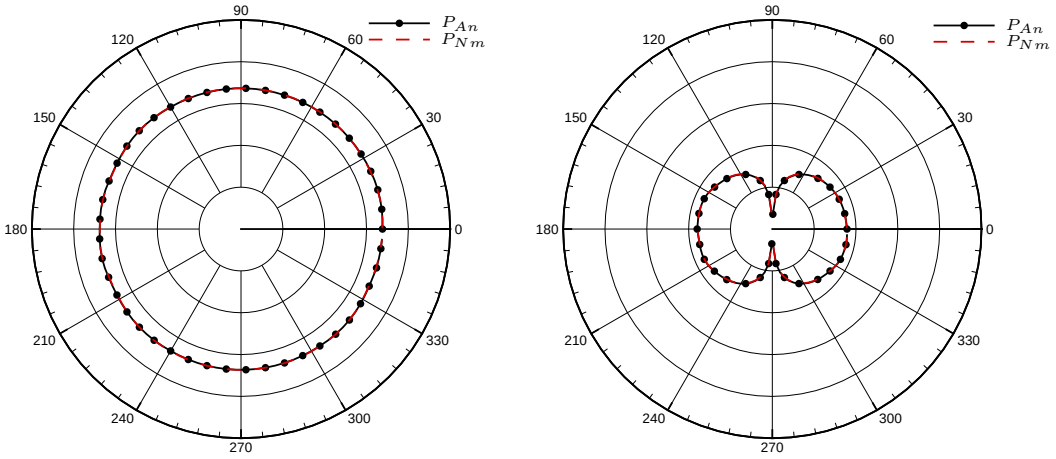

(a) *Monopole Directivity* **(b) *Dipole Directivity***

Figure 5.5: Sound pressure directivities of 3D monopole and dipole

The spatial discretisation errors for the numerical simulation of the 3D monopole, dipole and quadrupole sources are presented in Figures 5.5 to 5.10. The predictions were obtained exploiting all the quadrature methods described in the previous Chapter.

The prediction errors for a 3D monopole source are shown in Figures 5.6 and 5.7, where both the spatial discretisation errors behaviour with the aforementioned parameters and the polar error distribution are presented. Figures 5.6(a) and 5.7(a) show the results obtained via the midpoint quadrature based on the product of the panel's diagonals. Figures 5.6(b) and 5.7(b) are the prediction errors using the higher order Simpson's quadrature. The results obtained with the Gauss-Legendre quadrature illustrated in Figures 5.6(c) and 5.7(c).

In Figure 5.6, the discretisation errors for the different quadrature schemes are analysed in more detail. More precisely the relative error, ε^s_{av}, is plotted against ΔL_{max}, and for each line $\Delta\theta_{max}$ is constant. By decreasing ΔL_{max} with fixed $\Delta\theta_{max}$, the ε^s_{av} reduces continuously up to a minimum which is a function of $\Delta\theta_{max}$, directly

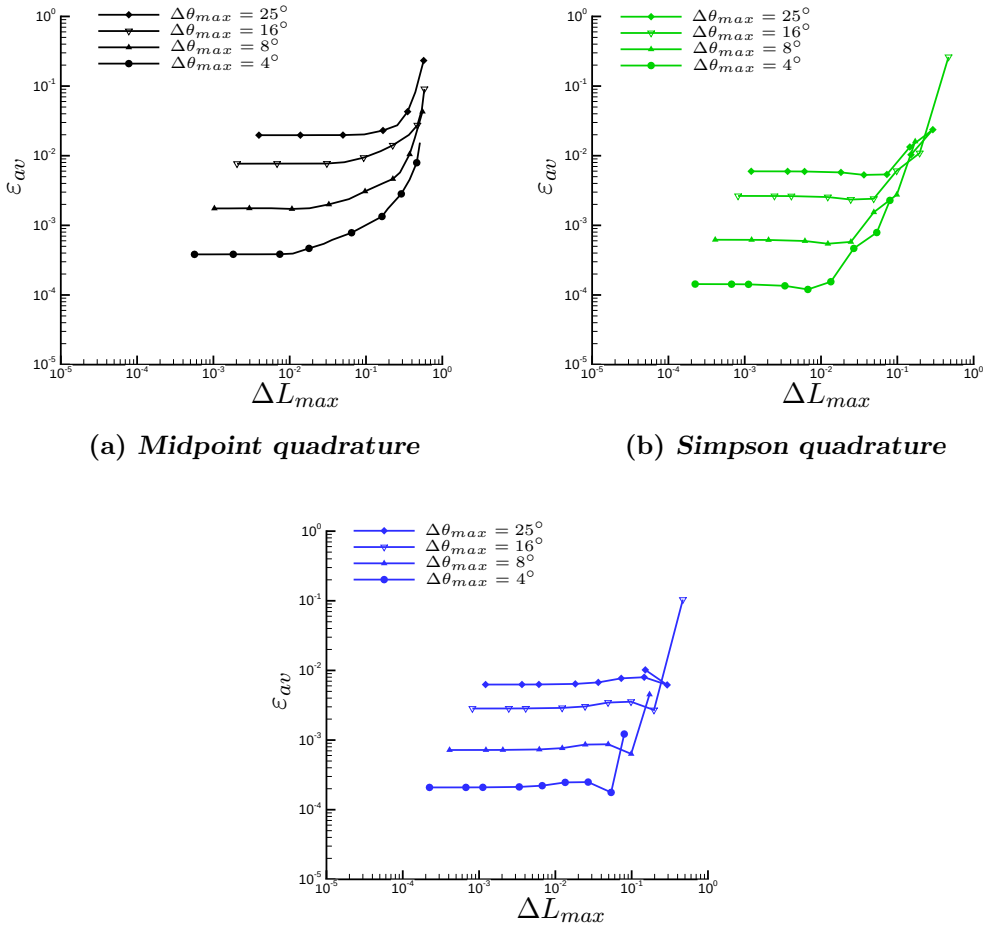

(a) *Midpoint quadrature* **(b) *Simpson quadrature***

(c) *Gauss-Legendre quadrature*

Figure 5.6: Monopole source: discretisation error ε_{av} using different quadrature schemes

proportional to $\Delta\theta_{max}$. This behaviour is shown for all the quadrature schemes, with the difference that the Simpson and G-L calculations converge more rapidly towards the minimum error and for larger values of ΔL_{max}.

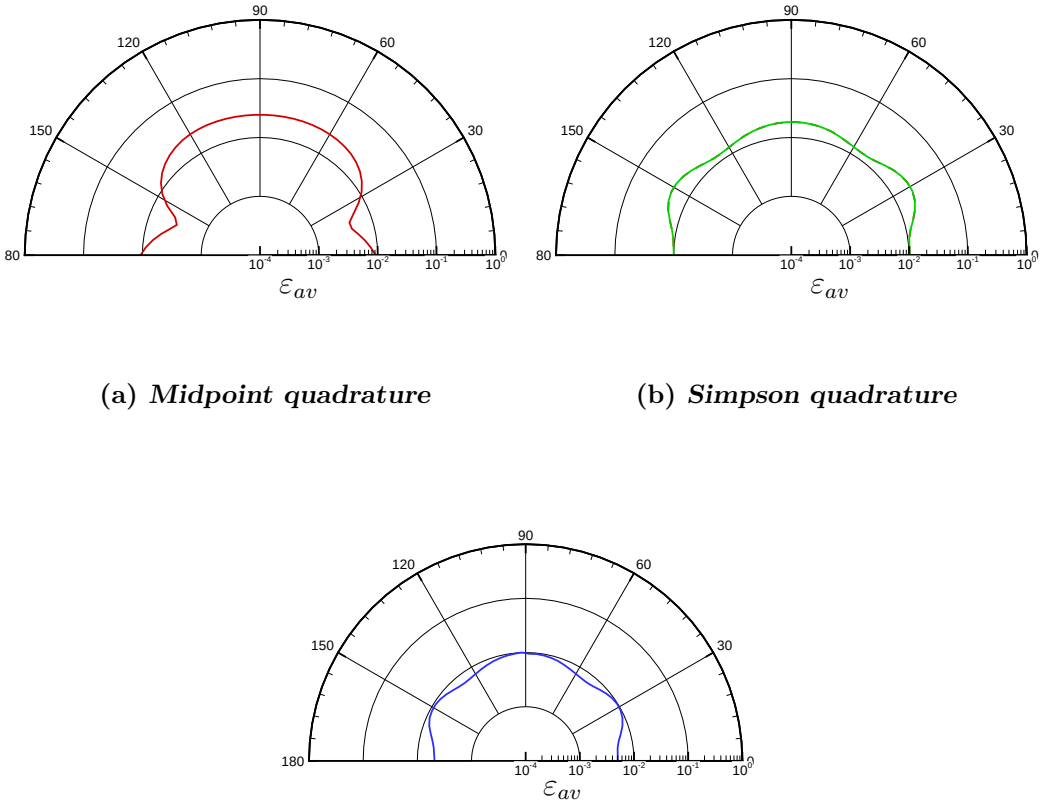

(a) *Midpoint quadrature* **(b) *Simpson quadrature***

(c) *Gauss-Legendre quadrature*

Figure 5.7: Monopole source: polar distribution of ε_{av} using different quadrature schemes

After ε^s_{av} reaches the aforementioned minimum it remains almost constant even if ΔL_{max} is further decreased. It is interesting to highlight the polar distribution of the error ε^s_{av} which in this case has been averaged only in time. The error for the Midpoint quadrature is very sensitive to the observer position. When the source radiation vector r is exactly parallel to the normal vector of one of the discretisation panels, and passes from the centre of this same panel, the Midpoint accuracy becomes higher than the accuracy of the more complex Simpson and GL quadratures for the same case.

This is visible in Figure 5.7, where in Fig.5.7(a) the distribution of the discretisation

error for the Midpoint quadrature is plotted as a polar directivity. Comparing this with Fig.5.7(b) and (c), it is clear that the minimum values of ε_{av}^{s} for the Midpoint are much lower than the errors in the other two schemes along certain position. Simpson and GL errors have a flat "directivity error". It is interesting to observe that the same behaviour in the "directivity error" is present when considering a dipole source, Fig.5.9. Here the Midpoint quadrature, Fig.5.9(a) shows a lower error with respect to the Simpson's quadrature, Fig.5.9(b), along the 30° and 150° directions.

It should be noted that the higher error around 90° direction is due to the topology of the dipole directivity, which has 0 magnitude in the regions close to 90°, Fig.5.5(b). A similar behaviour can be recognised in the "polar error" of the quadrupole source,5.10(b), which is high in the regions around $0-180°$ and $90-270°$. This can be explained by observing the quadrupole directivity, Fig.5.10(a).

From Figures 5.6(a) and 5.6(b), it is possible to draw the following conclusions: given a $\Delta\theta_{max}$ there is a limit value of ΔL_{max}, which defines the maximum accuracy that can be achieved by decreasing ΔL_{max}. A reduction of ΔL_{max} below this limit value does not improve the accuracy of the solution. This happens because the error, in these conditions, is dominated by the grid panel angular resolution, i.e. $\Delta\theta_{max}$.

In these Figures it is clear that both Midpoint and Simpson's quadrature are in very good agreement with the analytical solution. For a coarse spatial resolution, e.g. $\Delta\theta_{max} = 25°$, the errors ε_{av} are in the range of 1 to 3% for both quadrature schemes. When the spatial resolution is fine, e.g. $\Delta\theta_{max} = 4°$ then the ε_{av} becomes much smaller and reaches $\varepsilon_{av} \sim 0.05\%$ for the Midpoint quadrature and $\varepsilon_{av} \sim 0.01\%$ for Simpson's quadrature, at low ΔL_{max}. The error $\varepsilon < 3\%$, even for coarse surface meshes with $\Delta L_{max} \leq 5e-2$ and becomes $\varepsilon_{av} < 1\%$ for $\Delta L_{max} \leq 1e-2$. This is similar for all the quadrature methods analysed, i.e. Midpoint, Simpson and Gauss-Legendre quadratures, with the difference that the latter two methods reach $\varepsilon \leq 1\%$ at larger ΔL_{max}, more precisely for $\Delta L_{max} \leq 1e-1$.

Analysing the accuracy of the Midpoint quadrature scheme, in Figure 5.8, it is evident that the curves lay along the line with second order slope, which means that the theoretical accuracy of the method is preserved. On the other hand, moving at constant ΔL_{max}, in Fig. 5.6(b) and Fig. 5.6(c), between the four curves, it appears that with $\Delta\theta$ decreasing one order of magnitude the error ε_{av} decreases around 2 order of magnitude. Hence, the accuracy of Simpson and Gauss-Legendre schemes can only reach second order and not their theoretical higher order.

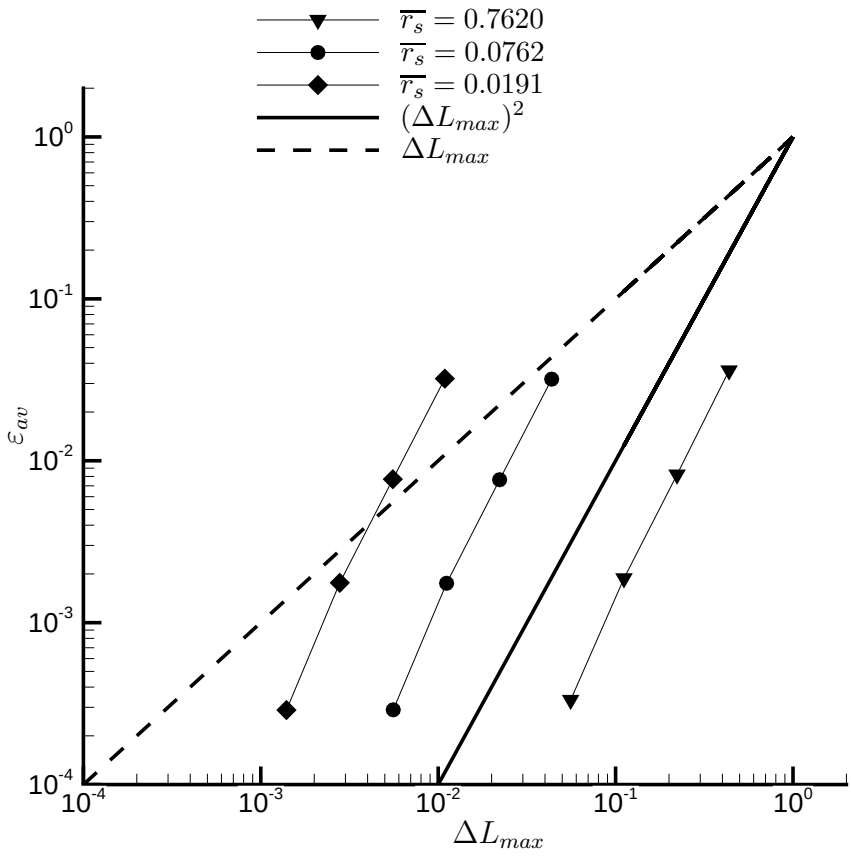

Figure 5.8: Accuracy of Midpoint quadrature

From the discussion above the use of Midpoint quadrature should be preferred when $\Delta L_{max} \leq 5e-2$. The Simpson and Gauss-Legendre quadratures improve the accuracy only slightly with respect to the Midpoint quadrature, but they require many more evaluation points per panel. In the present calculations 9 points per panel were used in both Simpson scheme and Gauss-Legendre schemes, which compared to the single point evaluation of the Midpoint scheme yield a large increase in computational time.

The analysis presented above suggests the use of the Midpoint quadrature, which allows to save computational time at the cost of a slightly lower accuracy with respect to the other two approaches. Using higher order quadratures requires a computational time between 1.5 and 2 times compared with the Midpoint method, while the accuracy of the higher order methods is comparable to the second order Midpoint scheme.

Finally it is interesting to compare the results obtained using the Farassat Formu-

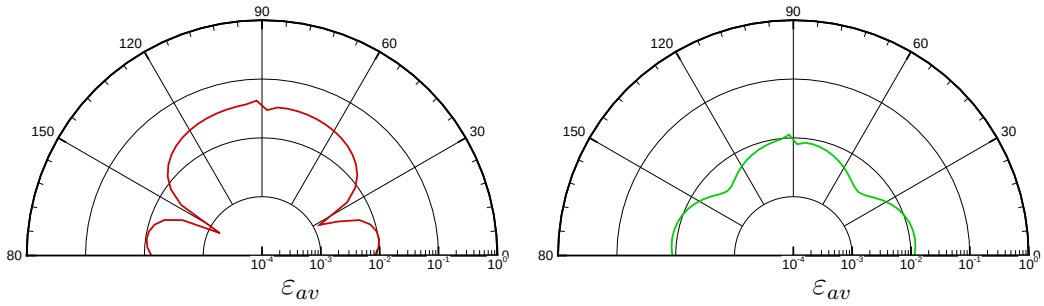

(a) *Midpoint quadrature* **(b) *Simpson quadrature***

Figure 5.9: Dipole source: polar distribution of ε_{av} using different quadrature schemes

lations 1, Eq.3.38, and 1A, Eqq.3.40,3.41. Fig.5.11 presents the errors between the predictions and the analytical results. The predictions in the figure were obtained using the two aforementioned formulations. From Fig.5.11 it is clear that the difference between the predictions can be neglected since it represent only a small fraction of the overall discretisation error.

The noise prediction algorithm and the implemented quadrature schemes are thus verified from the results presented in Figures 5.6-5.11, and following the discussion above, the following results in this Chapter are obtained using the Midpoint quadrature.

5.3 Emission Surface construction

In the previous Chapter, the correct solution of the retarded times and retarded positions was indicated, as the fundamental step for the construction of the Emission Surface. Another important part in this task is the correct implementation of the kinematics and the link to the retarded time roots of the problem. After having verified the correctness of the retarded time solution provided by the prediction tool, the direct computation of Emission Surfaces and their comparison with some cases available in literature will assist to test the surface construction and kinematics modules of the code. Furthermore, the examples of ES presented in the following subsections will help clarifying the meaning of these entities.

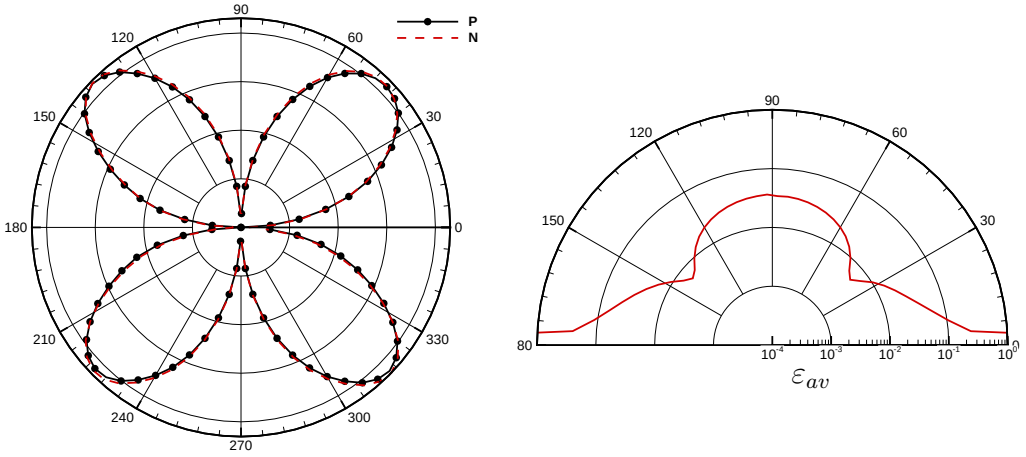

(a) *Quadrupole Directivities* **(b) *Quadrupole ε_{av} polar distribution***

Figure 5.10: Quadrupole source: directivities and ε_{av} polar distribution (Midpoint quadruature)

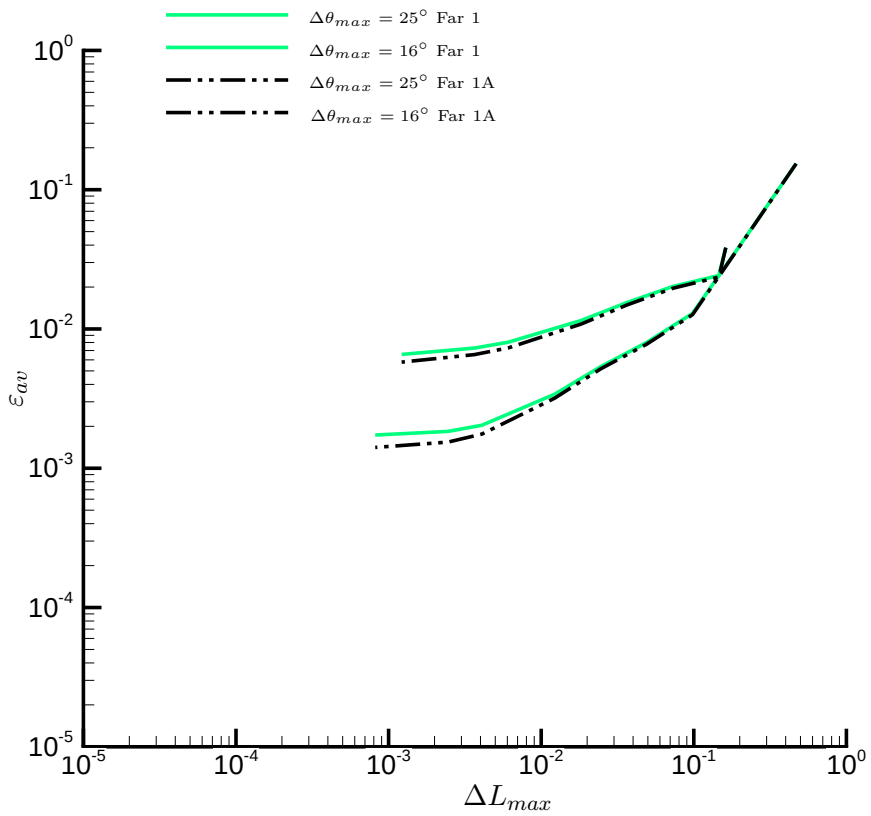

Figure 5.11: Error Comparisons between Farassat formulations 1 and 1A

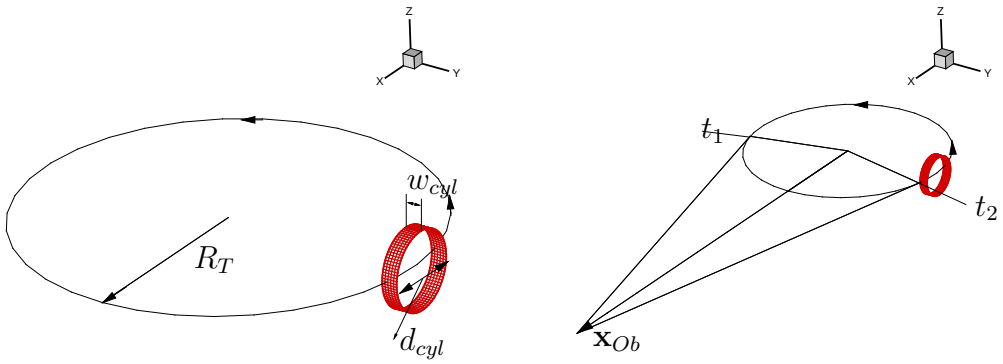

(a) ***Geometry*** **(b)** ***Observer position***

Figure 5.12: Geometry of Cylindrical strip and observer position

5.3.1 Cylindrical Strip

The first geometry considered during this analysis is a cylindrical strip where the axis is defined parallel to the plane of rotation (x, y) and it is rotating around z axis with a Mach number $M_T = 1.1$ calculated at the centre of the strip, i.e. the radial distance from the axis origin is $R_T = 1.1A_0/\Omega$. The geometry of the cylindrical strip and the observer position are illustrated in Figure 5.12. The diameter of the strip is $d_{cyl} = .44m$ and the width is $w_{cyl} = d_{cyl}/5$. The observer position is $\mathbf{x}_{ob} = (5, 0, 0)m$.

It is important to note the two lines indicated in Fig.5.12 with t_1 and t_2. These lines indicate the points in which the radiation vector connecting the centre of the strip and the observer in $\mathbf{x}_{Ob}$ is tangent to the path of the cylindrical strip. More precisely in the point t_2 the velocity vectors of the cylinder's points will have always $\mathbf{M}\cdot\hat{\mathbf{r}} < 0$ so that $|1 - M_r| > 1$. On the other hand in t_1 the condition is the opposite, since the velocity vectors are directed towards the observer. Here $M_r > 0$, thus $|1 - M_r| < 1$ and it is obvious that in t_1 there will be maximum value of M_r which in this case is $M_r = M_T = 1.1$. In the proximity of t_1 then there will be the two azimuth values for which $M_r = 1$. Within these positions will exist multiple sources for the same observer time instant.

In Fig. 5.13 is shown the emission surface generated by the motion of the cylinder at 6 different observer time instants. Observing Fig.5.13(a) it is evident the appearance of a second strip which is counter rotating with respect to the first one. This second cylindrical strip grows reaching the same dimension of the first one and then the

two strips arrive in contact, Fig.5.13(b). These two strips continue moving into each other and in Fig. 5.13(c) only one very large cylindrical strip is visible, which is the union of all the cylindrical strips locus of the multiple retarded positions corresponding to the roots of the retarded time equation.

This large cylindrical strip continues moving in the direction of rotation and the two sides of the strip come closer to each other. Again, in Fig.5.13(d), two strips are visible which are connected along a curve. The larger strip is the locus of the retarded positions corresponding to the first and second roots of the retarded time equation while the smaller is the locus of the positions corresponding to the third root. The two strips are divided and this is apparent in Fig.5.13(e). While the strips locus of the first and third roots are rotating in the positive direction, the strip corresponding to the second root is counter-rotating. In Fig.5.13(f) the cylindrical strip union of first and second roots is shrinking and will disappear, while the strip locus of the third root remains constant and moves further from the tangent point t_1.

The Emission Surface for a similar case, a cylinder strip rotating with $M_t = 1.1$, was calculated also by Ianniello [48]. Although in the paper was not specified any detail on the exact dimensions of the cylinder, it is still possible to have a qualitative comparison on the prediction of the ES. In Fig. 5.14 the ES prediction from [48] for similar observer time instants is shown. It is clear that the HelicA prediction tool correctly predicts the features and the geometry of the Emission Surface of a Cylindrical strip.

5.3.2 Blade Planform

The prediction tool is applied here to calculate the Emission Surface of a blade planform. The analysis of a blade planform with supersonically rotating tip, $M_T > 1$, is an interesting case which was studied for the first time by Wells, [99]. The geometry analysed by Wells consists of a rectangular blade extending from regions at very low Mach number, $M \approx 0.2$ at the blade root, to supersonic regions rotating with $M_T = 1.5$, at the planform tip.

The blade planform is the $1/7^{th}$ UH1H model scale rotor blade, with an aspect ratio of $AR = 13.71$. This blade is symmetrical with respect to the rotational plane. Thus it is possible to analyse only the upper or the lower part of the geometry. Figure 5.16 shows the corresponding Emission Surface for two different time instants. Two

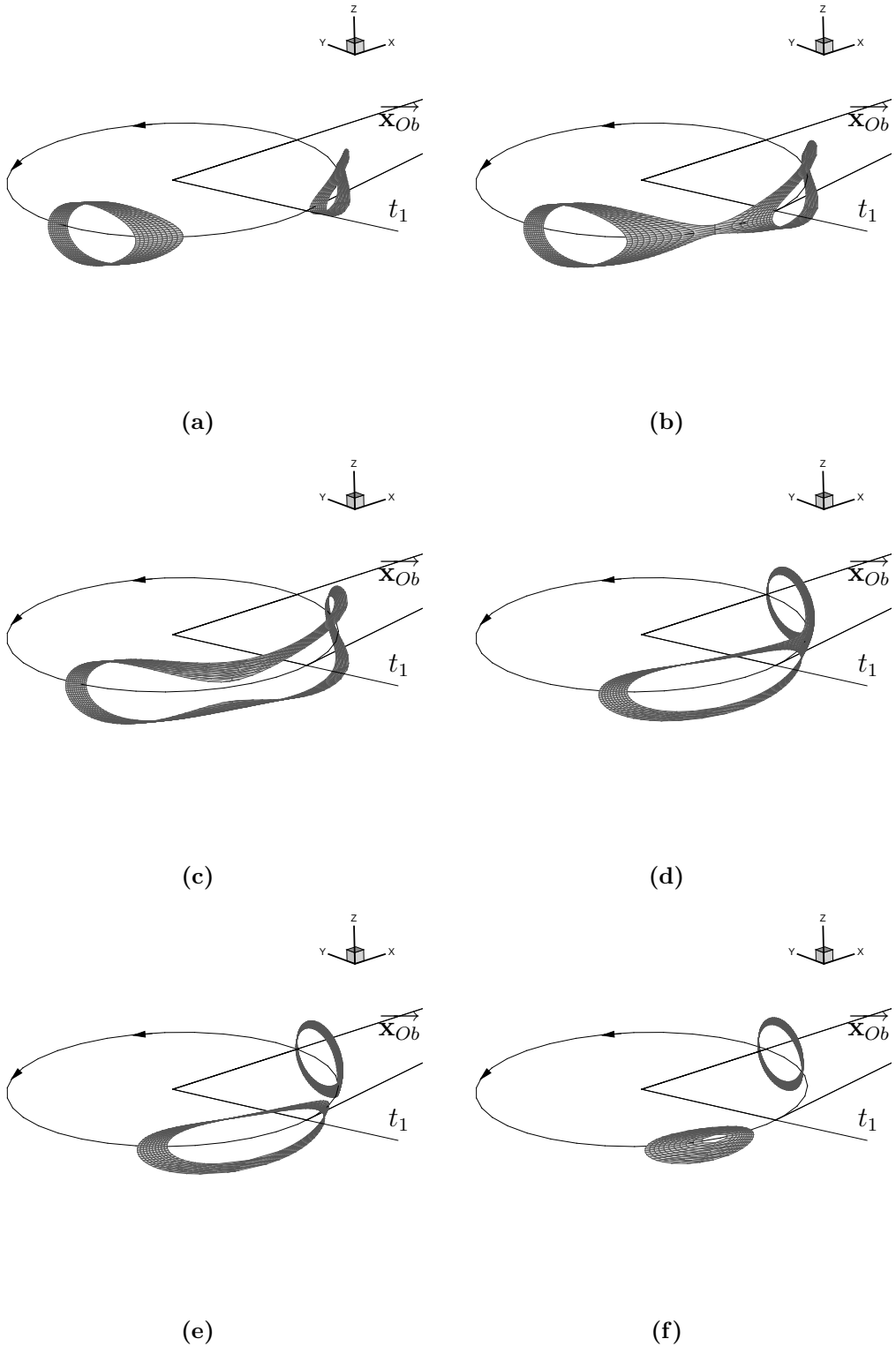

Figure 5.13: Emission Surface of Cylinder strip for different observer time instants showing the appearance and disappearance of the multiple surface branches corresponding to the multiple roots of τ

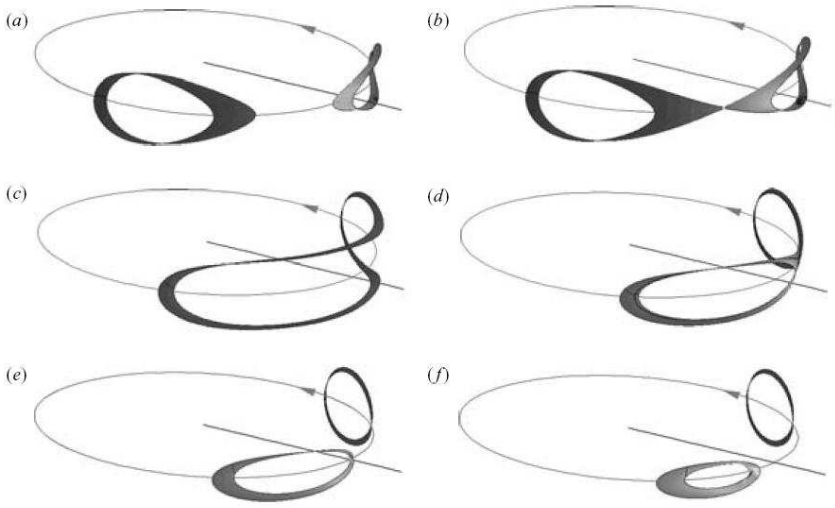

Figure 5.14: Emission Surface of Cylinder strip for different observer time instants as computed by Ianniello, [48]

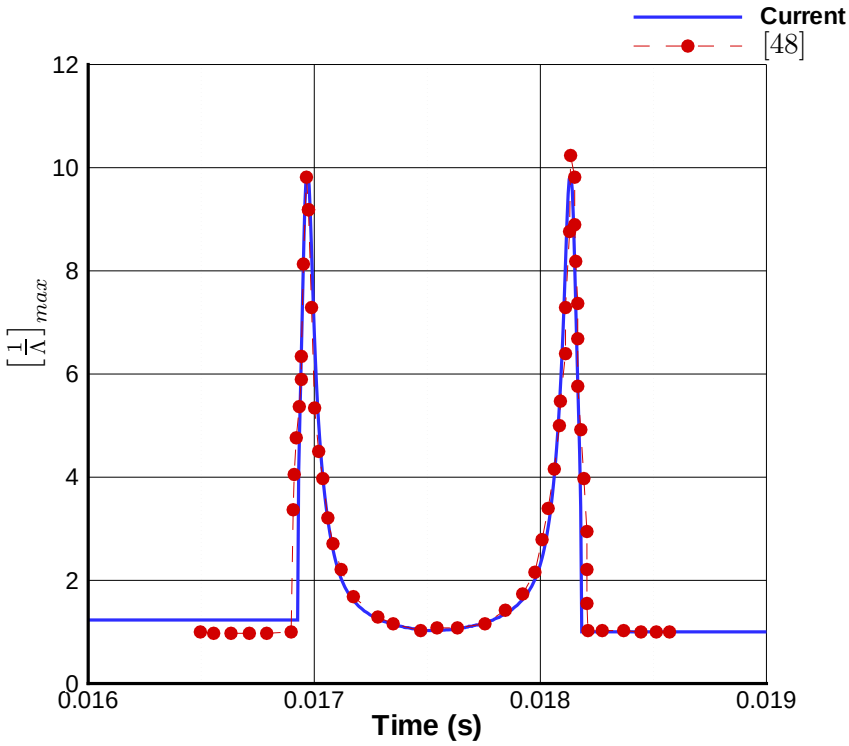

Figure 5.15: Time history of $[1/\Lambda]_{max}$ and comparison with the result in [48]

ES branches are present in Fig.5.16(a), which are curved towards the point at which $M_r = 1$. After few instants only one single ES is visible, Fig.5.16(b). It should be highlighted the large extension of the surface in Fig.5.16(b), where the initially rectangular blade reflects a shape similar to an anchor. The points close to the sonic circle have "escaped" from $M_r = 1$ forming the large "wings-like" extension in the surface.

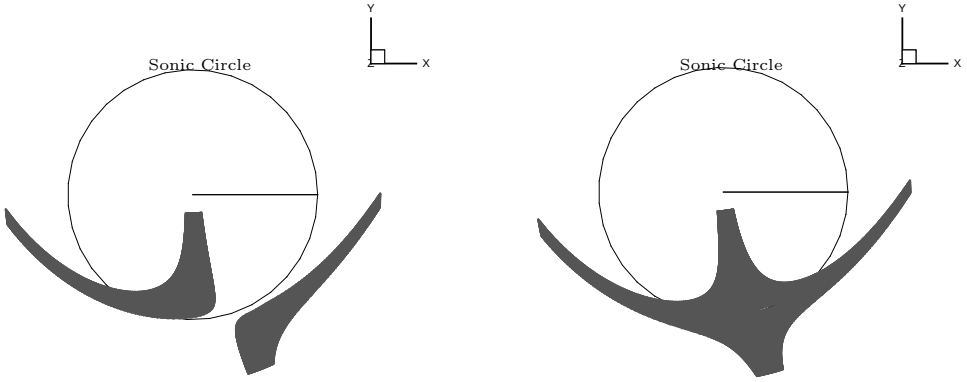

(a) **(b)**

Figure 5.16: Emission Surface of blade planform rotating at $M_t = 1.5$ for two different observer time instants

The same shape was predicted by Wells, [99] and later by Ianniello, [45]. More recently Ianniello, [47], explored and revealed the distribution $\Sigma(\tau)$, i.e. the time history of the area of the planform ES and its time derivative, for two different cases, one with Mach number range of $0.95 < M < 1.1$ and another case with $1.13 < M < 1.55$. In Fig.5.17 are shown both these quantities for the case $1.13 < M < 1.55$. The blade surface was discretised using an initial mesh of 40 chordwise by 70 spanwise nodes, which is then automatically refined by the code around the points with lower $1 - M_r$. From Fig.5.17 is clear that HelicA prediction is very close to the result presented in [47], which means that the shape and time history of the planform ES is correctly predicted. Some small differences are visible in the time derivative of Σ, Fig.5.17(b), which are connected with the smoothness of the ES. HelicA ES prediction is based on a panel by panel discretisation, which is very helpful in the case of non-structured surface meshes, as the ones provided by the Fluent CFD package. In contrast, the prediction tool, implemented by Ianniello, is based on a structured approach, i.e. considering all the points of the ES as forming one entity. In this latter case it is possible to apply, as described in [47], a smoothing step to interpolate the unevenly distributed grid on an evenly distributed ES mesh. To

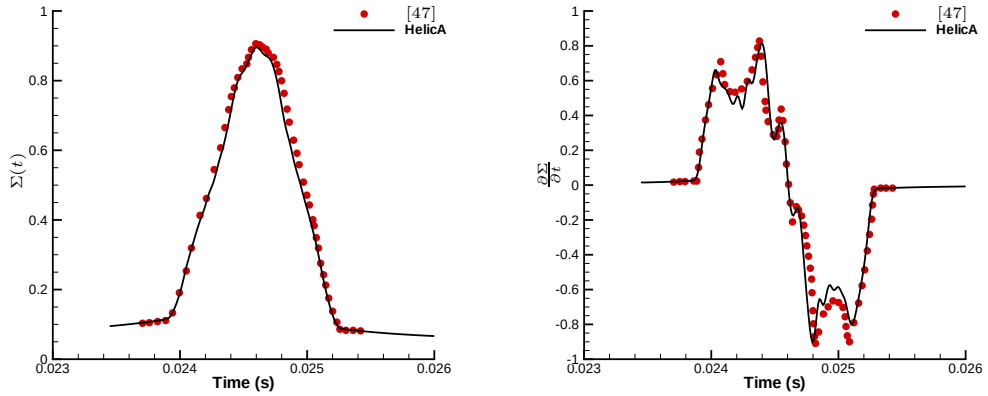

(a) **(b)**

Figure 5.17: Blade planform ES Area vs Time, comparisons with [47],, $M_T = 1.55$

the author's point of view it is this last step in [47] which produces the differences in Fig.5.17(b). Although the ES surface predicted with HelicA has a less smooth behaviour, it is clear that the prediction remains still very accurate and acceptable.

5.3.3 Panel normal to the rotation plane

Given the tendency of the Emission Surface points to escape from the $M_r = 1$ position, it is interesting to analyse the Emission Surface of a panel which is perpendicular to its rotational plane and has a finite extension, rotating in a transonic regime, with the panel overlapping the sonic circle. The panel shown in Fig.5.18(a) has an extension of $l_{pan} = 0.6m$ and is rotating at $M_t = 1.1$, with a radius of $R_T = 1.1(A_0/\Omega) = 1.1m$, since $A_0 = 340(m/s)$ and $\Omega = 340(1/s)$, which means that almost half the panel is in subsonic regime.

This case is very challenging for the ES construction algorithm because there is a point of the panel whose $\Lambda = 0$ and thus will present a discontinuity for the ES formulation. HelicA ES construction is still capable of computing the ES waveform but because of the Λ discontinuity the thickness noise for this case has a very large pulse. In Fig.5.18(f), which shows a view normal to the rotational plane, is visible a very similar shape to the one obtained in the blade planform analysis, Fig.5.16(b) points close to $M_r = 1$. More interesting is the view in Fig.5.18(c) and (d) were the multiple ES branches have appeared and are travelling toward each other. In the contact between the two branches a hole is clearly visible, exactly around $\Lambda = 0$.

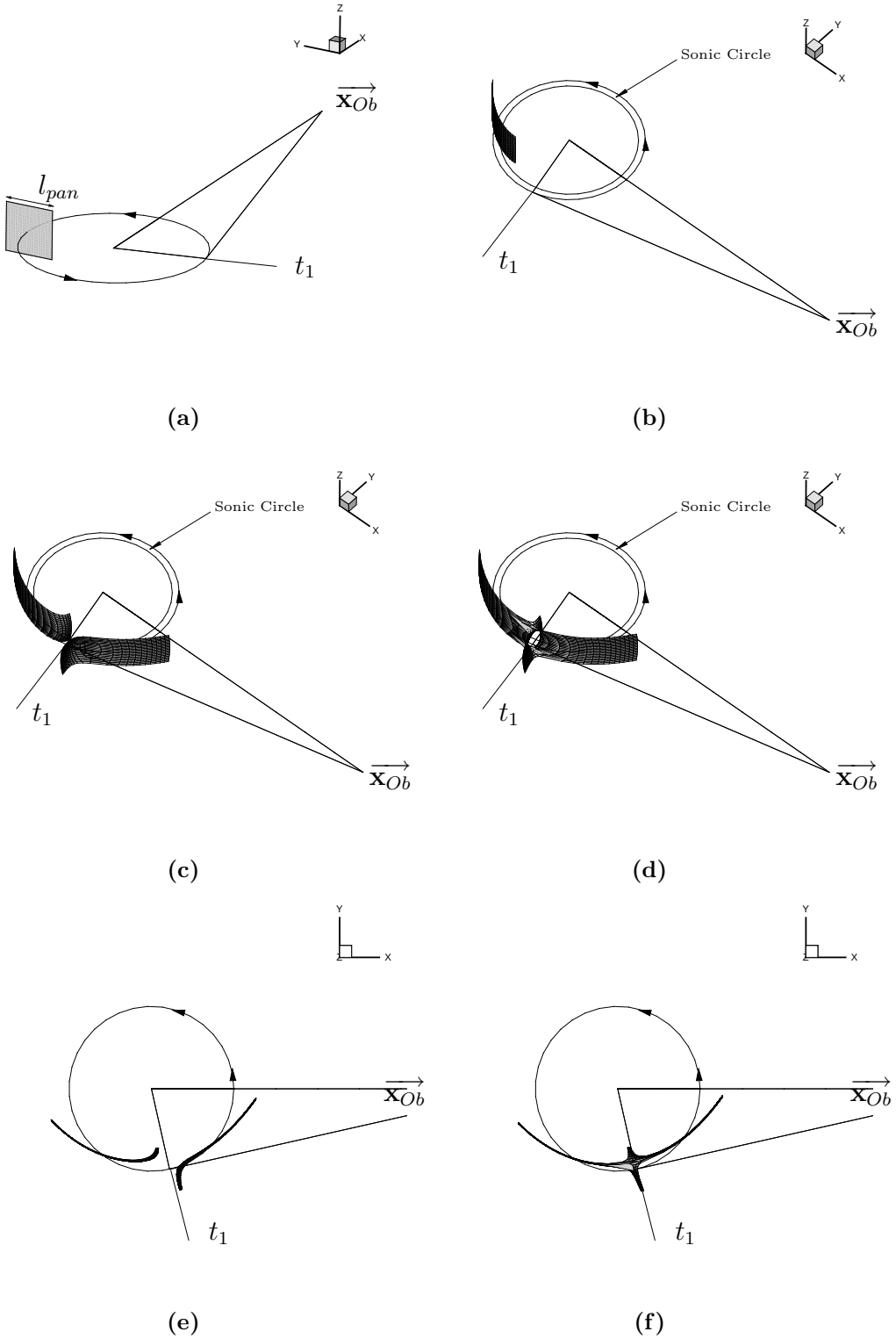

Figure 5.18: Emission Surface of a panel normal to the rotational plane

This is not a mistake in the prediction and it is due to the differences in the curvature of the ES branches locus of the first and third roots of the retarded time equation. The hole grows until the two branches are again separated.

5.3.4 Summary and conclusions

In this Chapter the verification and validation tests, for the noise prediction tool developed in this study, have been presented. First the root finder algorithm is applied to the solution of rotating sources with Mach numbers ranging from subsonic to supersonic conditions. From the comparison is clear that the proposed algorithm is faster than the Newton's and Brent's methods and that the required computational time is comparable to that of Advanced Time algorithms.

After these comparisons, the prediction tool is used for the analysis of $3D$ monopole dipole and quadrupole sources and the results are compared with analytical solutions. The analyses show that the accuracy of Midpoint quadrature is comparable to that of Simpson's and Gauss-Legendre methods in the cases of a discretisation with $\Delta L_{max} \leq 5e-2$. This suggests the use of the Midpoint method which is more efficient and has a similar accuracy to the other two methods when the aforementioned condition on ΔL_{max} is satisfied.

The calculations of the Emission Surfaces from three different geometries rotating at transonic/supersonic speed are then presented and compared with numerical results available in literature. These analyses demonstrate the capabilities, efficiency and accuracy of the noise prediction tool developed during this research.

Chapter 6

Subsonic and Transonic Studies of Noise Propagation around Aerofoils and Blades

As discussed in the Introduction and in Chapter 3, BVI and HSI noise are the two sources which contribute the most to the overall noise generation of an helicopter rotor. Thus, in this Chapter the prediction tool is applied to two cases comprising these noise sources: the HELISHAPE experiment for a rotor in BVI conditions, [17],[19]; and the transonic noise experiment on the $1/7^{th}$ UH1H model scale rotor in delocalised conditions, [32].

Before the analysis of the more complex $3D$ BVI problem, a study on $2D$ aerofoil-vortex interaction is presented. This study is useful to discuss the problem from a simpler point of view. Furthermore, the following $2D$ analysis allows to illustrate the phenomenon of spurious noise generation due to the passage of the vortex through the control porous surface. This problem is known to affect all the prediction codes based on porous surface formulations and can alter the quality of noise prediction as found for jet-noise calculations, [100].

In Table 6.1 are summarised all the methods used to obtain the predictions presented in the following sections. The cases show a variety of Re numbers, ranging between $6E5$ and $2E6$ and Mach numbers, between 0.5 and 0.95. The CFD solvers used during this research are all inviscid and more detail on each case will be given in the relevant sections.

Test Case	Re n.	Ma n.	CFD solver	Acoustic solver
2D-BVI Subsect.6.1.2.2	$\approx 6.0E5$	0.5	Euler Unst.	HelicA RET
2D-BVI Subsect. 6.1.2.3	$\approx 8.0E5$	0.8	Euler Unst.	HelicA RET
3D-BVI Sect. 6.2	$\approx 2.0E6$	≈ 0.6	BEM	HelicA RET HelicA ADV HelicA ES
HSI Sect. 6.3	$\approx 2.0E6$	$0.85 - 0.95$	Euler Rot.RF	HelicA RET HelicA ES

Table 6.1: Summary of methods used for the calculations

6.1 Aerofoil-Vortex Interaction

Various semi-empirical vortex models are exploited in aerodynamics applications. Yet, researchers are still focusing on the optimisation of the existing models or on creating novel models with increased capabilities for capturing the complex vortical structures of the vortices observed during experiments.

Semi-empirical vortex models are required during both experimental campaigns and computational analyses. Bagai and Leishman, [101], proposed the use of density gradient methods which combined with semi-empirical vortex models allow to obtain analytic results for the contrast variation of two dimensional compressible vortices. The mathematical results are strongly dependant on the particular choice of the vortex model.

On the computational side, extensive use of potential codes combined with wake simulation and semi empirical vortex models have enhanced the accuracy of aerodynamic predictions for fixed and rotary wing aircrafts. In particular, during the last two decades, the introduction of comprehensive codes has greatly improved aerodynamics and aeroacoustics predictions for helicopter rotors. In fact, these tools are capable of resolving the coupling of aeroelasticity and aerodynamics, which drives the complex aeromechanics of helicopter rotors.

Currently, most of the comprehensive codes implement free wake simulation as opposed to the less accurate prescribed wake. While the latter method makes assumptions on the rotor wake geometry, the free wake simulation computes the complete wake geometry by means of time marching algorithms which update the wake shape and position at every time step.

Although comprehensive tools which exploit the free wake analysis have higher accuracy, they can still present instabilities when the wake panels approach the body

surface control points. The instabilities are mainly caused by the unrealistic modelling of the Blade Vortex Interaction (BVI) physics where a zero-thickness wake is used. These instabilities can be avoided using thick vortices with semi-empirical models for the vortex core, i.e. a non-zero thickness wake. Such a wake model is essential during vortex body interaction because the local fluid flow around the impact region is determined by the spatial distribution of vorticity. Furthermore, the use of finite thickness vortex cores allows the calculations of Blade Wake Interaction phenomena such as the interactions between two close blade trailing vortices.

Hence, semi-empirical vortex models play a major role in order to obtain a more accurate and realistic modelling of a close interaction between wake and body. In fact, in recent years more sophisticated wake simulation and blade tip vortex models have been implemented in comprehensive codes with the aim of further improving the overall predictions [102]. On the other hand, the numerical solution of 3D unsteady NavierStokes equations using a mesh fine enough to allow the resolution of the blade tip vortices is not yet feasible. Therefore, in many engineering aerodynamic computations free-wake simulation with algebraic semi-empirical vortex models are used.

It is important to highlight that the particular choice of wake simulation and vortex model exploited in the aerodynamic calculations influences the quality of the computed predictions. In the case of aeroacoustic modelling of the noise generation a possibly stronger influence was identified by Baghwat et al. [103]. Vortex models differ not only with respect to the tangential and axial velocity distributions but also in the density and pressure field which they produce. Such differences could be considered to have negligible influence on aerodynamic calculations, however they will certainly have an effect on aeroacoustic predictions.

Vatistas et al., [104], pointed out the lack of knowledge about noise generated by the deforming vortices during vortex body interactions. They presented the different effects produced by two semi-empirical vortex models, the Taylor vortex and the Vatistas n=2 vortex, applied to two theoretical types of vortex body interaction: vortex impinging on a flat plate and on a circular cylinder.

The aim of this analysis is to identify the effects of different vortex models on both aerodynamic and aeroacoustic calculations of vortex body interactions. In fact, helicopter rotor BVI is a particular and interesting case of vortex body interaction because it is the most loud source, among helicopter's rotor noise sources, during specific maneuvers such as approach.

Furthermore, the noise produced by helicopter rotors during BVI depends on the strength of the blade tip vortices, the vortex core size, the interaction angles and vertical separation between the vortex and the blade, labelled as miss distance. BVI noise is therefore among all the helicopter rotor noise sources the one which is most influenced by the particular choice of rotor wake simulation and tip vortices models.

Given the importance of BVI noise, in this analysis the attention is focused on the effect of different vortex models on a two dimensional version of this phenomenon: aerofoil-vortex interaction. This is in fact a representative case which has similar characteristics with respect to the three dimensional BVI phenomenon and has a simple two dimensional geometry.

The comparisons will focus on the differences induced by the vortex models. This will improve the understanding of the vortex models influence, on the density and pressure distribution, during noise generation phenomena due to vortex-body interactions.

6.1.1 Vortex Models

Several semi-empirical models have been developed, first by Rankine,[105], Lamb and Oseen, [106], then by Taylor, [107] and more recently by Vatistas, [108], who proposed a family of self similar vortices comprising some of the previous existing models.

The most exploited vortex profiles in aerodynamic predictions are certainly the Scully model, the Lamb-Oseen, and the Rankine vortex profile. Baghawt and Leishman, [103], demonstrated that the Lamb-Oseen model can be closely approximated using the self similar vortex family of Vatistas with $n = 2$. In the present study this latter vortex model will be considered in place of the Lamb-Oseen model, and the different effects of all the aforementioned models will be analysed.

Until here the models have only been mentioned with no details on their representation. Thus, it follows a description of the analytical formulae for the velocity, density and pressure profiles of each vortex core model considered in this study.

A generic vortex model is given as a tangential velocity distribution which is only function of the distance from the vortex core centre, which can be written in polar

coordinates as:

$$v_\theta = v_\theta(r, \Gamma, R_c) \tag{6.1}$$

$$v_r = 0 \tag{6.2}$$

Where Γ represents the total circulation of the vortex, defined as $\Gamma = \int \Omega \mathrm{d}r\mathrm{d}\theta$ (Ω is the vorticity) and R_c is the vortex core radius. With the assumption, Eq.(6.1), that the velocity profile is only a function of r, it is possible to obtain an expression for the pressure field induced by the vortex from the momentum equations in polar coordinates:

$$\frac{\partial p}{\partial r} = \rho \frac{v_\theta^2}{r} \tag{6.3}$$

$$\frac{\partial p}{\partial \theta} = 0 \tag{6.4}$$

which means that $p = p(r)$. Considering a compressible fluid in isoentropic conditions, the pressure field is connected to the density field by means of the following relation:

$$\frac{p}{\rho^\gamma} = \frac{p_\infty}{\rho_\infty^\gamma} \tag{6.5}$$

The above relation leads to the definition of the constant parameter $k_0 = \frac{p_\infty}{\rho_\infty^\gamma}$, and can be used in eq.(6.3) to obtain the following differential equation for ρ:

$$\frac{1}{\rho}\frac{\mathrm{d}\rho}{\mathrm{d}r} = \frac{\rho_\infty}{\gamma p_\infty}\frac{v_\theta^2}{r} \tag{6.6}$$

Eq.(6.5) and (6.6) can be used to obtain the pressure and density filed for every semi-empirical vortex model.

The Taylor vortex model, a compact vortex, has been proposed by Taylor, [107], and used by many authors including Vatistas et al., [104] and Colonius et al., [109]. The tangential velocity distribution of the Taylor vortex has the following expression:

$$v_\theta = v_{\theta max}\frac{r}{R_c}e^{\left(\frac{1-\left(\frac{r}{R_c}\right)^2}{2}\right)} \tag{6.7}$$

where $v_{\theta max}$ is the maximum tangential velocity and R_c is the radius of the vortex core, corresponding to the maximum tangential velocity.

Integrating Eq.(6.6) and substituting Eq.6.7, the density and pressure distributions for the Taylor vortex are given by:

$$\rho(r) = \rho_\infty \left[1 - \frac{v_{\theta max}^2}{k_0}\frac{\gamma-1}{2}e^{\left(1-\left(\frac{r}{R_c}\right)^2\right)}\right]^{\frac{1}{\gamma-1}} \tag{6.8}$$

$$p(r) = k_0\rho^\gamma \tag{6.9}$$

Scully et al., [110], defined a vortex velocity profile in the following form:

$$v_\theta = V_\Gamma \frac{\overline{r}}{(1+\overline{r}^2)} \tag{6.10}$$

where $\overline{r} = \frac{r}{R_c}$ and $V_\Gamma = \frac{\Gamma}{2\pi R_c}$.

It is possible, by defining $\zeta = \frac{V_\Gamma^2}{2k_0}$, to write the density and pressure field for the Scully vortex in a compact form:

$$\rho(r) = \rho_\infty \left[1 - \zeta\left((\gamma-1)\frac{1}{1+\overline{r}^2}\right)\right]^{\frac{1}{\gamma-1}} \tag{6.11}$$

$$p(r) = k_0\rho^\gamma \tag{6.12}$$

Recently, Vatistas, [108], proposed a family of algebraic vortex velocity profiles, comprising some of the aforementioned models, which can be written in the form:

$$v_\theta = V_\Gamma \frac{\overline{r}}{(1+\overline{r}^2)^{\frac{1}{n}}} \tag{6.13}$$

The exponent n can vary from $n = 1$ to $n = \infty$. It is obvious that for $n = 1$ the profile coincides with the Scully model. As discussed above, the Vatistas vortex with $n = 2$ will be analysed in this paper.

The following assumptions are made in order to compare the effects of the different models on the numerical predictions:

- the same vortex core radius R_c is used for all the vortex models
- the same total circulation Γ is used in every model

Two test cases with are considered during the calculations, with $R_c = .018c$ and $R_c = .05c$ where c is the aerofoil chord. For the smaller R_c $\Gamma = .283$ while for the other case $\Gamma = .2$. It should be noted that fixing the two parameters of the model,

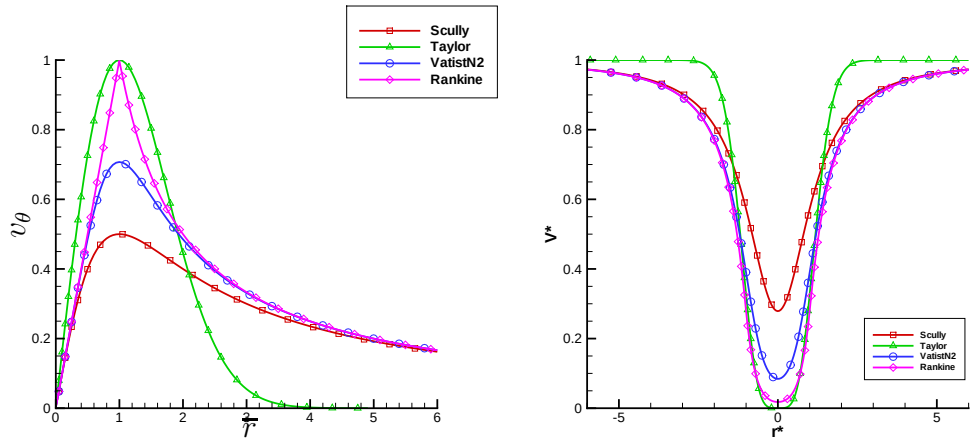

(a) *Velocity profiles* **(b) *Density profiles***

Figure 6.1: Vortex-induced profiles

R_c, Γ produces different maximum tangential velocities for each vortex model, this is visible in Fig.6.1(a). In this Figure the tangential velocities are non-dimensionalised using V_γ which is constant for a given set of R_c, Γ. The maximum tangential velocity for Taylor and Rankine vortices is equal to 1, while the maximum velocity for Vatistas vortex is equal to 0.74 and for Scully is 0.5. From the same Figure 6.1(a) is also clear that the Taylor vortex velocity profile influences only a very compact zone within the limit of $\overline{r} = 4$. The behaviour is similar also for pressure and density distributions where the peaks of Taylor and Rankine vortices are much higher compared to the other models.

6.1.2 Results and Discussion

6.1.2.1 Numerical method

Vortex body interaction is one of the most challenging problems for aerodynamic and aeroacoustic predictions. For instance, in the case of aerofoil-vortex interaction, different levels of numerical approximations, [111], [112], [113], have been adopted depending on the computational resources and flow discretisations. Several difficulties arise during numerical prediction of vortex body interaction. The main problem encountered is the numerical dissipation which characterises CFD codes. This severely affects the strength of the vortices, particularly in the flow regions where the grid resolution is low, e.g. far away from the aerofoil.

In the present study, the two-dimensional implicit Euler solver of the commercial software Fluent was exploited. The Euler solver is based on a cell centred finite volume method with Roe Flux-Difference Splitting (FDS) scheme for the convective fluxes. The governing equations are integrated in time using a second order implicit time-marching method with dual time stepping. The inner iterations of the dual time stepping were performed until residual convergence dropped by three orders of magnitude.

A second order upwind scheme was used for the spatial discretisation. In order to limit the numerical dissipation which is induced by large cells, three different mesh levels have been tested during this study. In effect, as discussed above, researchers have tried to resolve the dissipation problem by means of several different techniques such as Compressible Vorticity Confinement (CVC), [112] or Adaptive Algorithms, [111] and [113]. These efforts were aimed at defining a method which allows the use larger mesh cells, and hence less computational resources.

In the current study, the efficiency of the mesh distribution and the computational time of the CFD algorithm were not the main concern and it was decided to use a large number of nodes in order to preserve the vortex strength as long as possible. Three mesh levels have been considered with a number of nodes varying from 100 up to 210 thousand, and after a comparison of the preserved vortex strengths, the finer mesh was chosen for all the calculations. This latter mesh is shown in Fig.6.2, where the different blocks used can be observed. A very fine mesh is visible upstream of the aerofoil leading edge with an average resolution of 8 nodes per vortex core. The blocks are connected using non-conformal interfaces which allow the use of a different node distribution on each side of the faces connecting the different blocks.

6.1.2.2 Subcritical Head-on Interaction

Aerofoil-vortex interaction has been studied by various researchers. The experiment conducted by Lee and Bershader, [114], is a well documented example. During their experimental campaign the authors analysed a head-on parallel interaction with a $M_\infty = 0.5$ and non-dimensionalised values for $\Gamma = 0.283$ and $R_c = 0.018$. In the head-on case the miss distance between the aerofoil leading edge and the centre of the vortex core is 0.

This experiment is of particular significance since it was used as a reference case

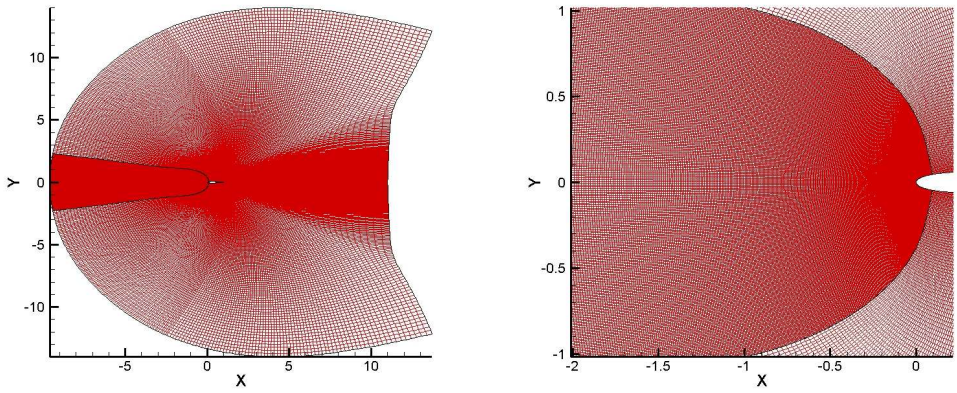

(a) *Overall* **(b) *Close up***

Figure 6.2: Mesh used during calculations

for previous computational analyses, [111],[112],[113]. All these numerical analyses were conducted by superimposing the Scully semi-empirical vortex model to a steady solution of the flow around the NACA 0012 aerofoil with the same flow conditions as in [114]. To the knowledge of the author, no numerical study so far exploited a vortex model other than the Scully model in this particular analysis.

The unsteady Euler calculations for this case have been performed adopting the numerical method described in the previous section with a physical time step size, non-dimensionalised by the time $t_c = c/U_\infty$, of $\delta t = 0.01$, i.e. 1/100th of the time that a signal travelling with the free stream velocity needs to cover one aerofoil chord length c. This means that the vortex, which is convected by the free stream velocity, was moving every time step of $\delta x_v = 0.01c$, approximately half the core radius, $\delta x_v \approx R_c/2$.

The comparisons of the pressure coefficient c_p time history with the experimental data in [114], are shown in Fig.6.3. The plots refer to the case of subcritical Head-on interaction with $M_\infty = 0.5$ and are calculated in the point $x = 0.02c$, i.e. 2% from the aerofoil leading edge (L.E.). It is interesting to see the effect of the time step size on the calculations, in Fig.6.3(a). By using a larger Δt, the c_p peak value over the upper surface of the aerofoil is underestimated of around 50%. The same effect can be found for the c_p distribution over the lower surface of the aerofoil.

In Fig.6.4 are presented the effects of the time step size and the order of temporal discretisation on the convected vortex strength. In this Figure it is shown the vorticity magnitude of the vortex, Ω, divided by the initial vorticity Ω_{Max} versus

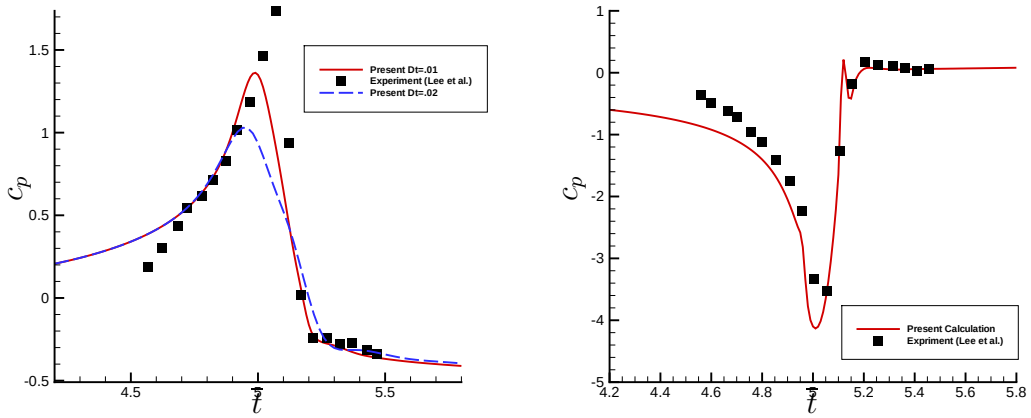

(a) c_p ***Upper surface*** **(b)** c_p ***Lower surface***

Figure 6.3: c_p time history at the point $x = 0.02c$ and comparison with the experiment of Lee et al., [114]

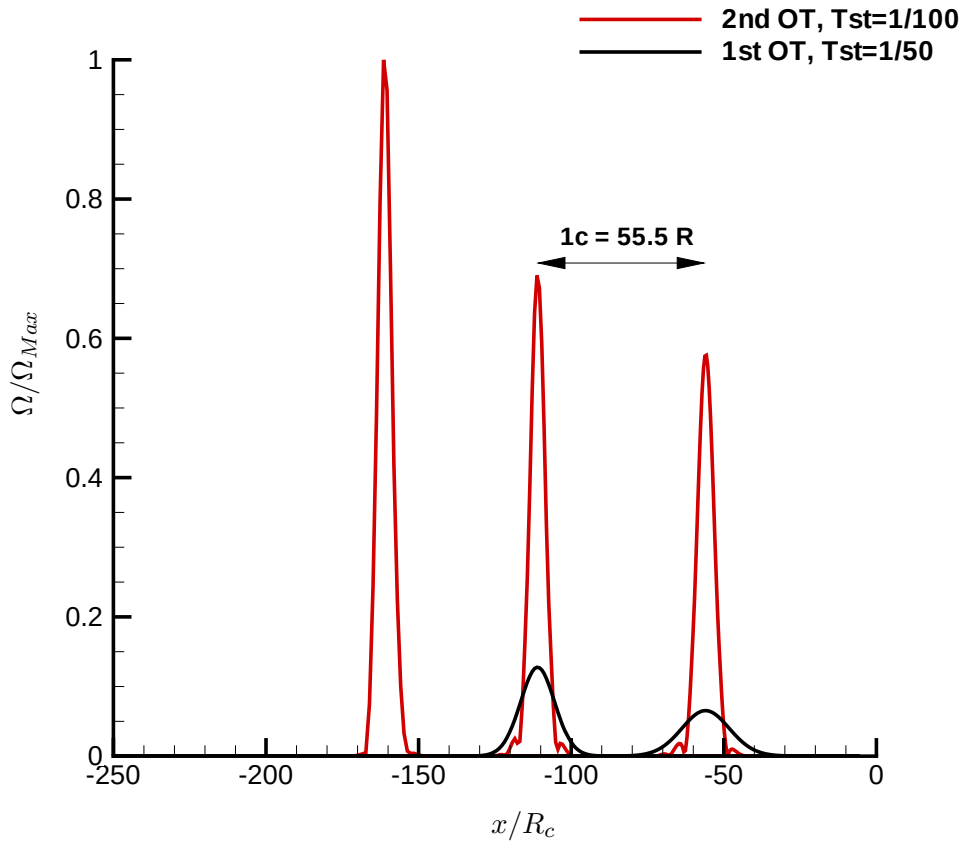

Figure 6.4: Effects of time discretisation on the Vorticity Magnitude

the vortex position normalised by the vortex radius x/R_c. It is clear that with the second order discretisation and $\delta t^* = 0.01$ the vorticity magnitude remains around $0.7\Omega_{Max}$ after the vortex is convected $55R_c$ upstream of the initial position and then Ω becomes $.6\Omega_{Max}$ after a total distance of $110R_c$ from the initial vortex position. On the other hand, by using, for the same spatial resolution, a first order temporal discretisation with $\delta t* = 0.05$, the vorticity strength is $0.15\Omega_{Max}$ after $55R_c$ and becomes $\leq 0.1\Omega_{Max}$ at $110R_c$ from the initial vortex position.

The differences in pressure fields induced by the Scully and Vatistas models are presented in Fig.6.5. In particular, this Figure shows four different positions of the vortex, starting from the point where the vortex was initially superimposed to the steady solution, 6.5(a). The contours in this case have been clipped to $20Pa$, i.e. the regions in red, such as the vortex core, have higher differences.

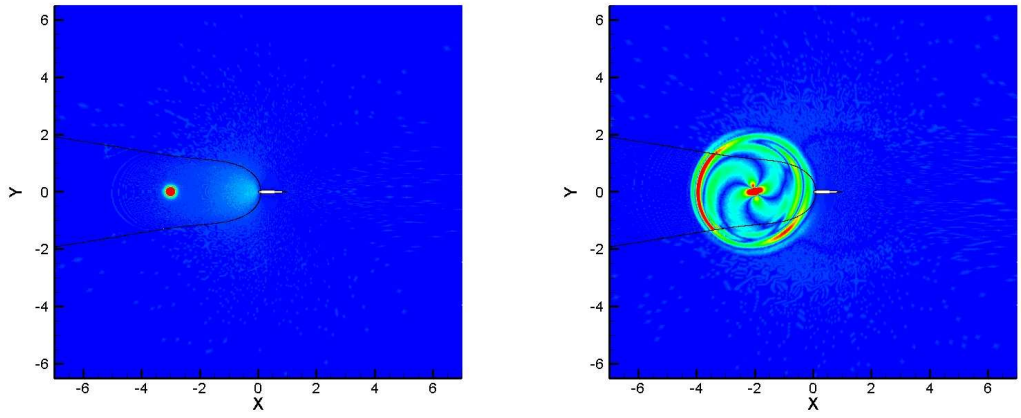

(a) $x_v = -3c$ **(b)** $x_v = -2c$

Figure 6.5: Difference in pressure field between Scully and Vatistas models, for two locations of the impinging vortex.(The contours are clipped [0-20]Pa)

From Fig.6.5(a) it is clear that the initial difference, when the two vortices are superimposed, is concentrated just on the vortex cores, with some scattering from the aerofoil leading edge. The vortex is then convected with $M_\infty = 0.5$ and when it reaches a distance of 2 chords from the leading edge, Fig.6.5(b), the pressure field difference, which is emitted by the centre of the vortex core at $M = 1$, has now a radius of 2 chords, i.e. $1/(M_\infty)$ times the distance travelled by the vortex. The ΔP field now reaches the aerofoil leading edge and the region in proximity of the aerofoil is altered by the presence of the solid body.

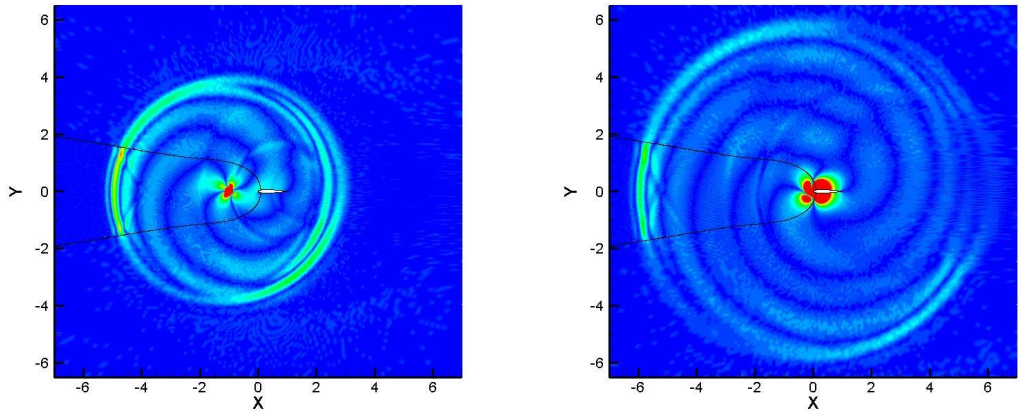

(a) $x_v = -1c$ **(b)** $x_v = 0c$

Figure 6.6: Difference in pressure field between Scully and Vatistas models, for two locations of the impinging vortex.(The contours are clipped [0-20]Pa)

Following the vortex further downstream at 1 chord distance from the L.E., Fig.6.6(a), the ΔP field has now a radius of 4 chords and the aerofoil is fully immersed. The side of the ΔP field containing the aerofoil is apparently quite different from the clean side. A part from the differences induced by the aerofoil solid surfaces, it is quite evident the presence of ΔP waves scattered from the aerofoil leading edge. These were generated when the ΔP disturbance reached for the first time the aerofoil's L.E. In Fig.6.6(a), the centre of the scattered ΔP can be found on the aerofoil's T.E. and the outer scattered wave has radius of 2 chords. This scattered wave tends to attenuate the ΔP difference between the two vortex models. The effect can be recognised by the darker colour circle centred in the aerofoil trailing edge (T.E), which coincide with the wave front of the scattered ΔP waves.

A very similar behaviour can be recognised in Fig.6.6(b), but in this case the vortex has reached the aerofoil L.E. and the ΔP field in proximity of the aerofoil surface has large magnitude, indicated by the dark red region enclosing the aerofoil. The wave front of the ΔP field extends now over a radius of 6 chords around the aerofoils L.E. The location of the vortex's centre is at the L.E.

Figures 6.5(b),6.6(a) and 6.6(b) clearly show four spirals staring from the vortex centre and extending up to the ΔP wave front. These are generated by the difference in tangential velocities between the vortex models and as a consequence of the rotational movement of the vortex. The lengths of the spirals depend on the differences of the vortex-induced velocity fields between the two models, as shown

in Fig.6.1(a).

Figure 6.7, shows the comparison between the pressure field induced by the Scully, Vatistas and Rankine models. The ΔP magnitudes are much higher than those presented in Fig.6.5, highlighted in the red colour regions, and the differences in ΔP between Rankine and Scully are much larger than those between Rankine-Vatistas. This could be expected considering the formulations of the equations of the models, 6.13. The behaviour of the ΔP is similar to the one described in the previous paragraph and the spirals are more intense in the Scully Rankine comparison. Furthermore, the spirals are longer in this last case since the difference between the maximum tangential velocities between Rankine and Scully models are larger than those between the Rankine and Vatistas models.

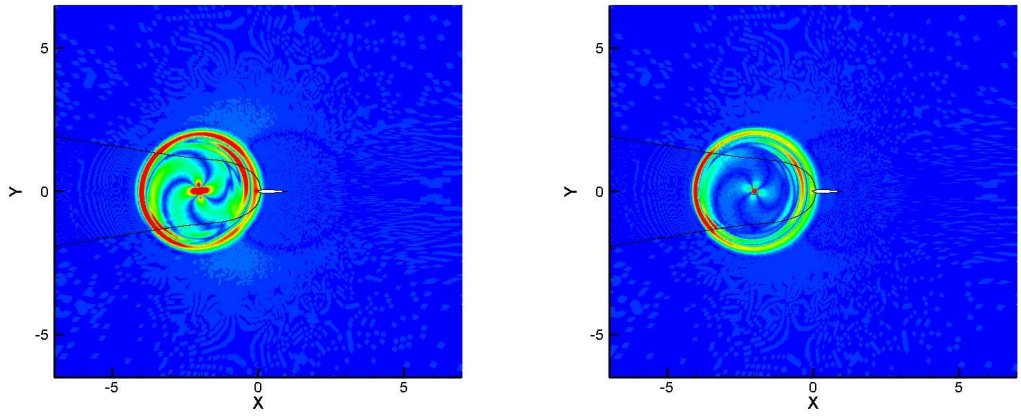

(a) ΔP ***Scully-Rankine*** **(b)** ΔP ***Vatistas-Rankine***

Figure 6.7: ΔP differences between three vortex models, (Contours clipped [0-20]Pa, $x_v = -2c$)

It must be noted here that even if the Vatistas, Scully and Rankine models belong to the same family, the ΔP difference fields between the models are of considerable magnitude, especially if compared with the human hearing threshold which is $2\mu Pa$. In the case of the Taylor model, which has a different mathematical form, the ΔP difference field, between this vortex and the others, reaches higher magnitudes. In Figure 6.8 the contour ranges have been extended up to $2kPa$, i.e. 100 times the one used in Figure 6.5.

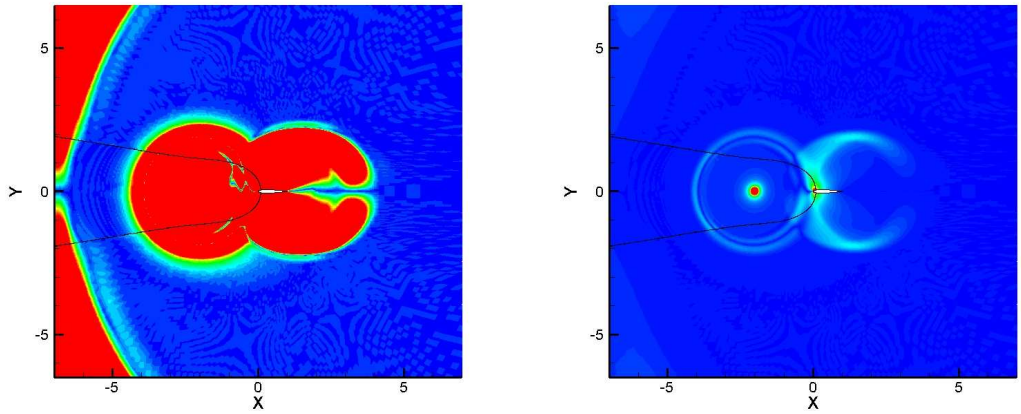

(a) ***Contours*** $(0-20)Pa$ **(b)** ***Contours*** $(0-2000)Pa$

Figure 6.8: ΔP differences between Taylor and Scully models, ($x_v = -2c$)

6.1.2.3 Supercritical Parallel Interaction

The case presented in the previous subsection was an Head-on interaction and the vortex was convected with a subcritical Mach number. In the following case the Mach number is $M_\infty = 0.8$ and the vortex has a miss distance of $y_v = 0.25c$ from the aerofoil L.E. The parameters for the vortex models are: non-dimensionalised $\Gamma = 0.2$ and $R_c = 0.05$, as in [111],[113] and [115]. Since the Mach number is supercritical, two shocks are present in the steady state solution of the $NACA0012$. This means that the aerofoil vortex interaction is more complex because of the additional interaction of the vortex with the shocks over the aerofoil. In effect, the presence of the shocks influences the ΔP field as shown in Fig.6.9, where the maximum pressure contour was maintained at 20 Pa for consistency with the previous plots. In this case there are 3 scattered waves which originate from the L.E. and from the two shocks over the aerofoil. Furthermore the ΔP magnitude is much higher than that of the subcritical case and the shock positions and magnitudes are affected by the differences in the models.

6.1.2.4 Acoustic Pressures

The near-field ΔP differences between the vortex models have been presented in the previous section. From the discussion above and by analysing the contour plots, it appears that the differences between the models are smoothed during the propa-

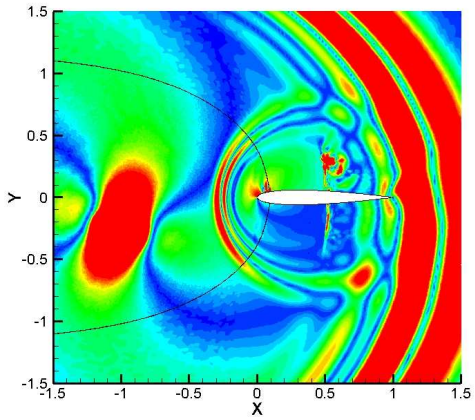

Figure 6.9: ΔP differences between Scully and Vatistas models, ($M_\infty = 0.8$, $x_v = -1c$, Contours $(0 - 20)Pa$)

gation. Hence, it is necessary to analyse the far-field acoustic pressure in order to understand whether the smoothing is due to the intrinsic dissipation of the CFD or the physical dispersion of the pressure signal.

In the following results the far-field acoustic pressure is predicted using the noise prediction code on permeable surfaces developed during this research. Four observer positions have been considered, $2c$, $5c$, $10c$ and $20c$ from the aerofoil. The following analysis is focused on the subcritical head-on case which presented a lower ΔP magnitude and hence weaker front waves, Fig.6.6(b).

In Fig.6.10 the acoustic pressure prediction at an observer $2c$ above the aerofoil, Fig.6.10(a), and $2c$ below the aerofoil, Fig.6.10(b), are compared with the prediction from Morvant et al. [112]. Both plots follow very closely the predictions in [112] which to the knowledge of the author have the only acoustic pressure data for the head-on aerofoil-vortex interaction case.

The acoustic pressure time history at an observer $y_o b = 20c$ above the aerofoil is shown in Fig.6.11. It should be noted that in Fig.6.11 a small oscillation in the acoustic pressure is apparent, this oscillation was identified as spurious noise due to the passage of the vortex through the permeable surface. The spurious source was identified by performing the calculations of the vortex in free stream, i.e. without the airfoil, and computing the emitted acoustic pressure, which in this case should be equal to 0. The problem of spurious noise affects permeable surface algorithms when turbulent fluctuations or vortices pass through the control surface, [100].

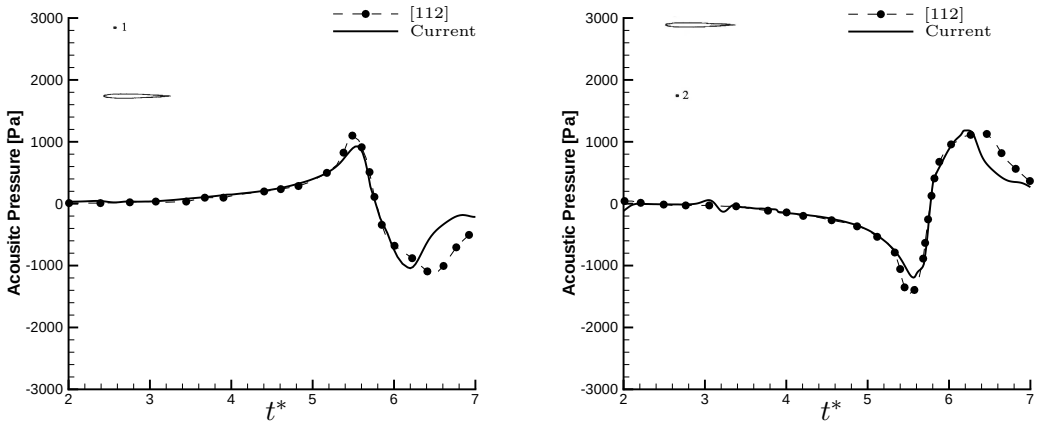

(a) *Observer* 1 *at* $2c$ *above the aerofoil **(b) *Observer* 2 *at* $2c$ *bleow the aerofoil***

Figure 6.10: Comparison Acoustic Pressure at 2 observer positions above and below the aerofoil

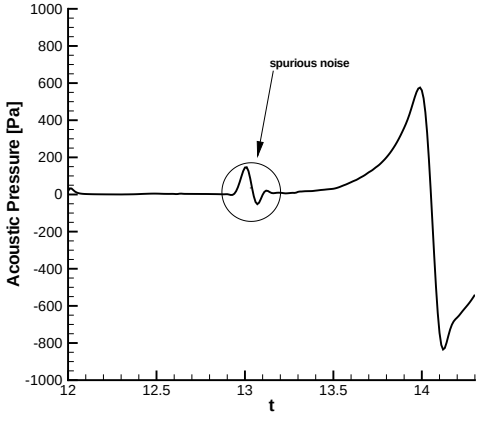

Figure 6.11: Far field Acoustic Pressure, $y_{ob} = 20c$

Despite the existence of the spurious sources, it is still possible to evaluate the differences in the far field acoustic pressure between the Vatistas and the Scully Vortex models, as presented in Fig.6.12. These differences are around $50Pa$ for the observer in $y_{ob} = 10c$, Fig.6.12(a). Moving further away from the aerofoil, an observer positioned at $y_{ob} = 20c$, Fig.6.12(b) perceives a ΔP signal which has half the magnitude of the one in Fig.6.12(a).

This trend suggests a linear behaviour, i.e. the amplitude of the acoustic signal decays as the inverse of the radiation distance, as expected from the theory. Hence the excessive decay presented in Fig.6.6 must be attributed to the intrinsic numerical dissipation. It must be highlighted that the initial difference in the induced pressure fields is contained only in the vortex core, which in the case under analysis is 0.0184 chords. This means that the initial pressure difference can be perceived in a region of $1000R_c$, at the observer $y_{ob} = 20c$.

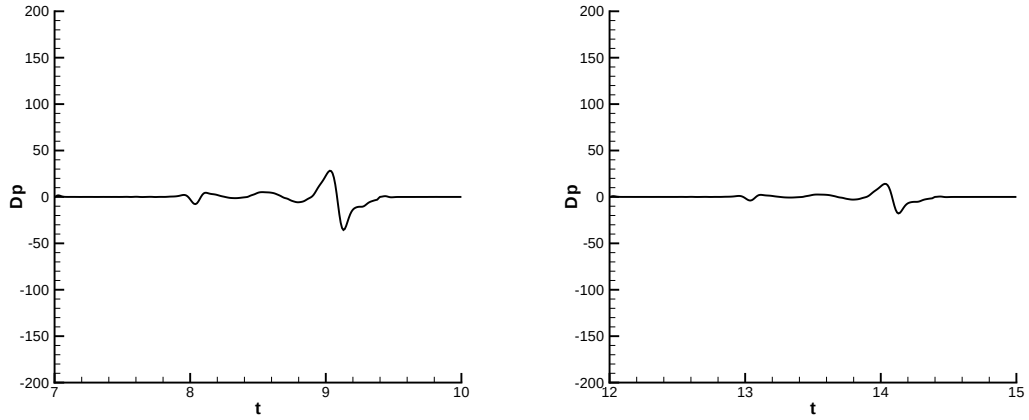

(a) $y_{ob} = 10c$ **(b)** $y_{ob} = 20c$

Figure 6.12: Differences in the far field acoustic pressure between Vatistas and Scully models for two observer positions

It is interesting to observe the differences in Sound Pressure Levels (SPL) and directivity patterns between the different vortex models. More precisely in Fig.6.13 the directivity patterns for the Vatistas, Scully and Taylor vortices are presented. It is clear that between the Vatistas and Scully models, 6.13(a), the differences in both directivities and SPL magnitude are very small, around ΔSPL_{V-S} $1dB$. On the other hand, the differences between Vatistas and Taylor are apparent not only in the directivity patterns but even more in the SPL magnitude $\Delta SPL_{V-T} \geq 15dB$. In the case of the Rankine vortex these values should be in between the above boundaries,

i.e. $\Delta SPL_{V-S} \leq \Delta SPL_{V-R} \leq \Delta SPL_{V-T}$ and closer to the difference between Vatistas and Scully vortices.

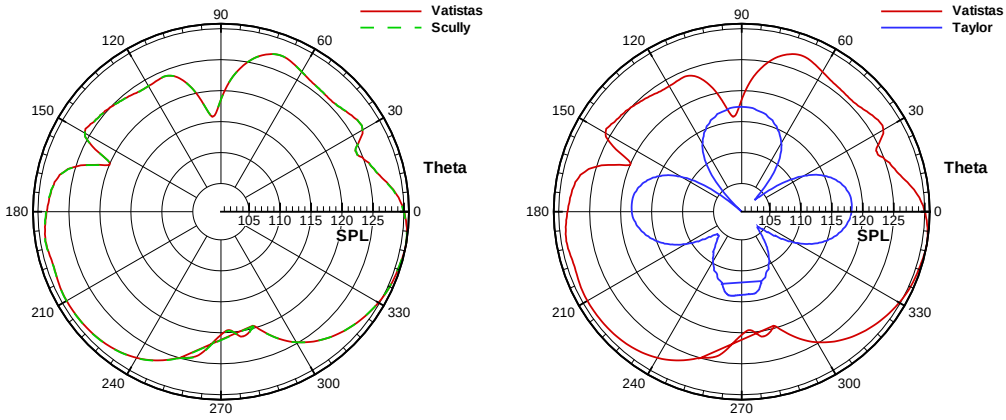

(a) ***Vatistas and Scully vortices*** **(b)** ***Vatistas and Taylor vortices***

Figure 6.13: Directivities Comparisons between three vortex models at an observer $y_{ob} = 10c$

6.2 3D Blade Vortex Interactions

In the previous section, the analysis of $2D$ aerofoil-vortex interaction was presented in order to examine the issues involved during the complex problem of vortex body interaction. In this section the study of vortex body interaction problems is extended to three dimensions by analysing two model scale helicopter rotors during Blade Vortex interaction.

The analysis of such a problem is useful to further testing the capabilities of the aeroacoustic prediction tool developed during the current research. The aeroacoustic results will be compared against the measurements from the wind tunnel experiments [17], performed by the HELISHAPE consortium in the nineties. These experimental results have been already documented in other European projects [19], and used for validation purposes, [116].

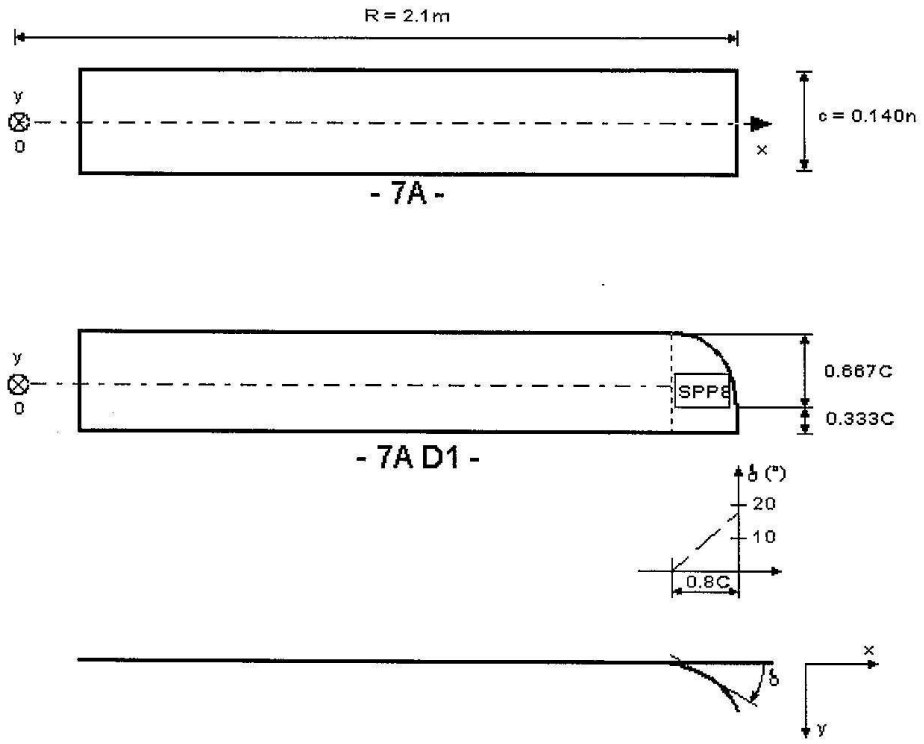

Figure 6.14: Model Rotor Blade geometries in the Helishape campaign, [117]

6.2.1 Experiments description

Within the framework of a previous European cooperative research program on rotorcraft aerodynamics and acoustics (HELISHAPE), a parametric model rotor test was conducted in the open test section of the DNW. These tests used the MWM test rig of DLR and a highly instrumented model of a fully articulated ECF rotor equipped with blades of advanced design and two exchangeable blade tips. The two blade geometries shown in Fig.6.14 were considered during the Helishape experimental campaign.

One set of blade tips had a rectangular shape whilst the other one had a swept-back parabolic/anhedral shape. The objectives of those experimental tests were to evaluate noise reduction techniques and to validate the partners' aerodynamic and aeroacoustic codes. The aeroelastic blade deflections, especially the torsional and flap-wise deflections that represent important parameters affecting BVI noise and vibrations, were determined from the measured data by means of elementary beam bending theory . In addition, valuable information on the tip-vortex geometry and blade-vortex miss distance was obtained by means of the LLS flow visualization

technique.

A comprehensive set of simultaneous acoustic and aerodynamic blade surface pressure data, as well as blade dynamic and performance data, were measured during the HELISHAPE tests.

Test Case No.	Rotor Type	Aerodynamic Conditions
TC08.4	7A	Low-speed 6° descent $\mu = 0.16616$ $C_T/\sigma = 0.08155$ $M_{\Omega R} = 0.61651$ $\alpha_{TPP} = 4.5°$ $\theta.70 = 2.90°$ $\theta 1c = 2.76°$ $\theta 1s = -1.42°$
TC09.5	7AD1	Low-speed 6° descent $\mu = 0.16599$ $C_T/\sigma = 0.08147$ $M_{\Omega R} = 0.61816$ $\alpha_{TPP} = 4.22°$ $\theta.70 = 3.01°$ $\theta 1c = 2.99°$ $\theta 1s = -1.69°$

Table 6.2: Helishape low speed descent cases chosen for validation. $\mu_{ar_{x_i}} = \frac{U_{x_i}}{U_{tip}}$

For each acoustic measurement point, the ensemble averaged sound pressure time histories as well as the averaged narrow band power spectra (via FFT) have been calculated. A time domain window was not applied to these data. The conditional sampling approach employed minimised leakage of acoustic energy at the blade passage frequency (bpf) and its harmonics, and thus a time domain window was not required to improve the spectral estimates at these frequencies. The data were further evaluated in terms of A-weighted summary levels.

The two test cases chosen for the assessment of the computational tools discussed above are presented in Table 6.2. Both of them are at low speed 6° descent, a condition in which the wake coming from one blade impinge directly on the following blade generating strong BVI events and thus fluctuations in the blades' loading. This unsteady pressure distribution is the main factor of the noise produced by the rotor in subsonic flights.

6.2.2 Computational tools

The complex motion and aeromechanics of the helicopter rotor was discussed in Chapters 3 and 4. Given this complexity, a stand alone aerodynamic prediction tool is not capable of accurately computing all the flow features necessary for a reliable aeroacoustic analysis of helicopters rotors in descent or in forward flight. Only the comprehensive tools, described in the previous section, can produce an accurate aerodynamic prediction for BVI noise analysis.

Since no in-house comprehensive code was available at Cranfield, the following aerodynamic predictions were obtained as a collaboration with AGUSTA and University of Roma Tre as a part of the Friendcopter project, Task 2.1 described in the introductory Chapter. The aim of this task is to define noise abatement procedures, which is a fundamental step towards a more environmentally friendly helicopter. BVI noise is the source more affected by the particular flight procedure.

It follows a brief description of the comprehensive tools of Augusta [118], identified with Comprehensive Tool 1 (CT1) and Roma Tre, [119], identified with CT2.

6.2.2.1 Aeroelasticity

The aeroelasticity calculations in CT1 uses an AGUSTA in-house code. The formulation of the code is entirely based on a Finite Element Method (FEM) approach providing modal and frequency response to aerodynamic and inertial loads acting on the blades. This is done via the lifting surface method in order to determine the aerodynamic load on the deformed blades by means of a free wake vortex lattice formulation.

The evaluation of the blade structural dynamics for the CT2 is based upon the non linear flap-lag-torsion equations of motion developed by Hodges and Dowell, [120]. These are based on a beam-like model and are valid for straight, slender, homogeneous, isotropic, nonuniform, twisted blades and undergoing moderate displacement. In the present calculations the kinematics of the blade are included through a simplified model in which the blade deformations vary linearly along the radial direction, with the tip flap, lead-lag and torsion deflections coinciding with those measured in the wind tunnel tests.

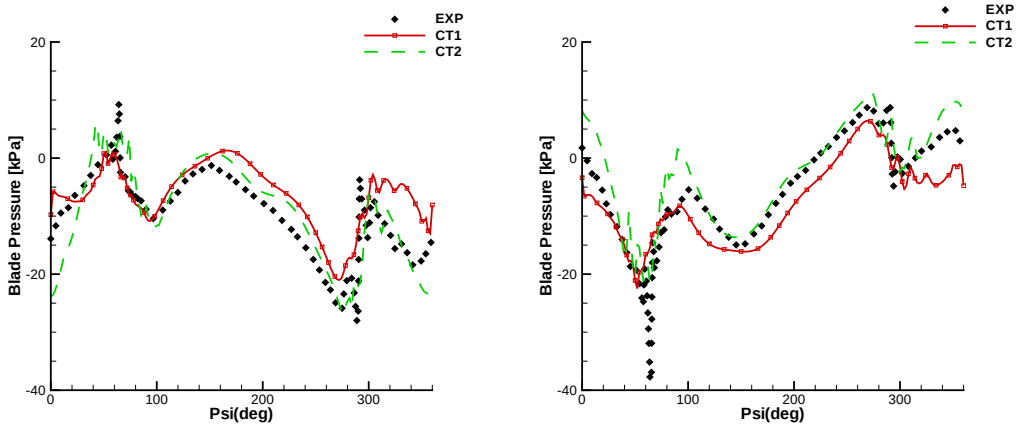

(a) ***Upper surface*** **(b)** ***Lower surface***

Figure 6.15: Pressure time history on the blade upper and lower surfaces, case TC08.4, for the point $x/c = 0.02$ $y/R = .98$

6.2.2.2 Aerodynamics and wake modelling

The aerodynamics prediction modules of the two comprehensive tools exploited herein are quite similar and are based on the Boundary Element Method (BEM). This is the most widely used approach in helicopters' analysis due to the complexity of the geometry and motions of the vehicle. Other approaches such as Finite Volume Method (FVM) would require: firstly the generation of a domain grid, whereas the BEM methods are based only on boundary surfaces grids, and secondly the computational resources and convergence time are much greater than the BEM case.

In particular, CT1 utilizes an unsteady 3D panel method where the prediction of the flow field around complex multi-component configurations in arbitrary motion is possible. The methodology is based on the solution of the Drichlet problem for Laplace's equation written for a discrete singularities' distribution simulating the bodies' surfaces. Tangency of the fluid flow to solid boundaries is adopted at every time step following Morino's formulation and the mutual interactions of bodies and wakes are taken into account.

The aerodynamic module of CT2 is based on a boundary integral formulation for the velocity potential that is suitable for helicopter configurations where wake/blade interactions (BVI) occurs. This formulation is fully 3D, and can be applied to bodies with arbitrary shape and motion, and allows the calculation of both wake distortion and blade pressure field. For a realistic modelling of a close interaction between the wake and a body, a non-zero thickness wake model is essential because of the

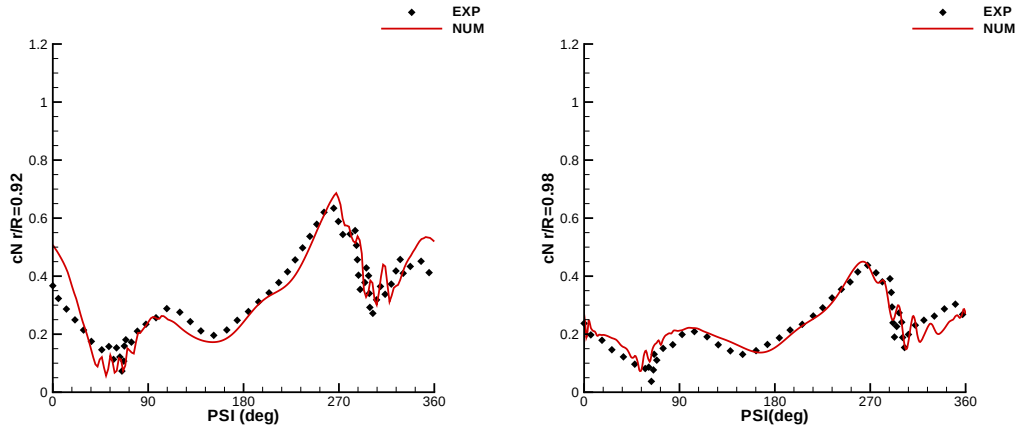

(a) ***Spanwise location*** $y/R = .92$ **(b)** ***Spanwise location*** $y/R = .98$

Figure 6.16: Normal force coefficient, case TC08.4 at two blade sections

fundamental role played by the vorticity spatial distribution when determining the local fluid flow around the impact region.

In particular, both in CT1 and CT2 the contribution of the wake portion experiencing BVI is expressed in terms of thick vortex distributions (i.e. Rankine vortices) rather than in terms of doublets distributions. The two comprehensive tools can perform prescribed or free wake calculations. Using the latter approach the solution is obtained by a time marching integration scheme in which the wake is moved according to the velocity field computed from the potential solution.

6.2.2.3 Results

In Figures 6.15(b) to 6.16(b) are presented the pressure, at the L.E., and the normal force coefficient C_n time histories for the case TC08.4, as described in Table 6.2. The time is represented as the blade azimuth position. The pressure distributions along the blade surface have been computed by AGUSTA and Roma Tre exploiting the tools described above. The C_n distributions in Fig. 6.16(a) and 6.16(b), have been computed using the quadratures and the kinematic tools implemented in the HelicA aeroacoustic code. All the results are compared with the available experimental data. It is clear from the plots that the prediction codes are capable of capturing the measurements very closely. The zones close to 90 and 270 degrees of azimuth are of particular interest to check the quality of the predictions because they are the positions where all the BVI encounters happen.

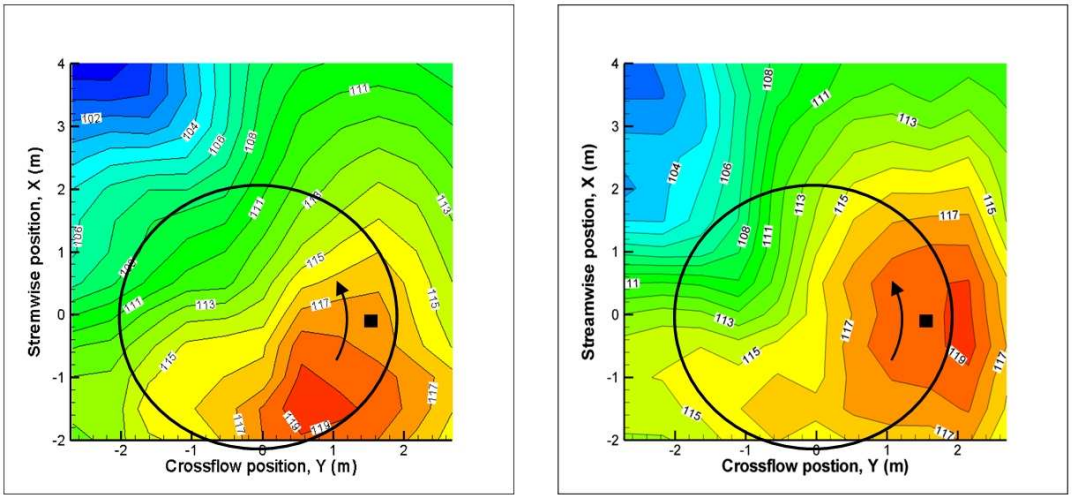

Figure 6.17: Noise footprints comparisons for the case TC08.4, left numerical and right experimental. Represented in OASPL [dB]

The codes predict the characteristics of the pressure fluctuations in good agreement with the experimental data, both in terms of phase and amplitude. Higher differences are visible around the peaks of both pressure and C_n. It should be noted that the spanwise positions presented, $r/R = 0.92$ and $r/R = 0.98$ are the ones in which BVI phenomena are more intense, hence, the predictions can be considered in very good agreement. Furthermore, the C_n plots, Fig. 6.16(a) and 6.16(b), at the same spanwise sections, show that the blade aerodynamics and kinematics have been well resolved.

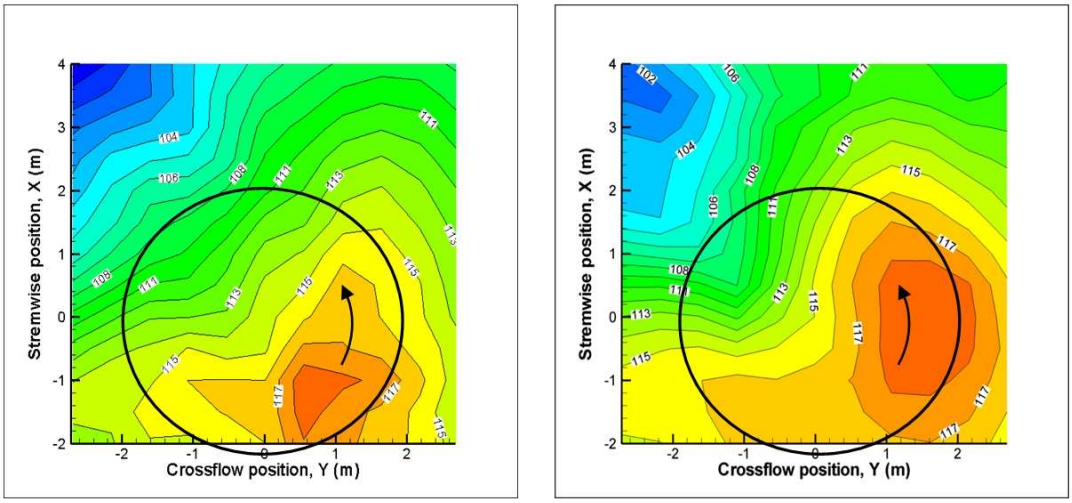

Figure 6.18: Noise footprints comparisons for the case TC09.5, left numerical and right experimental. Represented in OASPL [dB]

The above discussion demonstrates that the dynamics and aerodynamics of the rotor have been predicted correctly. Hence, based on the above predictions, it is possible to compute the noise generated during BVI conditions for the two rotor geometries. It should be noted that in the Figures 6.17-6.18 are presented only the results obtained by coupling CT1 with the HelicA noise prediction tool. This is because the results obtained with the other computational chain, i.e. CT2 + HelicA, are very similar to the ones presented here.

Several HelicA formulations, as shown in Table 6.3, have been applied for the noise prediction of the 3D-BVI cases. From the table is evident that the time required by HelicA ES is comparable with both HelicA ADV and HelicA RET, but in this latter case there is a difference when the Brent root finder is used instead of Newton-Raphson. Although the different formulations require slightly different computational times, Tab.6.3, the acoustic prediction are coinciding. For this reason only the result from the HelicA ES algorithm are presented here.

Acoustic solver	Comp. Time*
HelicA RET (Newton root finder)	≈ 1.2
HelicA RET (Brent root finder)	≈ 0.7
HelicA ADV	1.0
HelicA ES	≈ 1.1

Table 6.3: Summary of time required by different formulations, subsonic sources. (*All times are divided by the time required by the ADV formulation.)

The control surface used for the FW-H approach and the aeroacoustic calculations coincide with the solid surface of the rotor blade. Figures 6.17 and 6.18 present the comparisons between the computational and the experimental noise footprints for the two test cases. Figure 6.17 refers to the case TC08.4 which corresponds to the standard untapered blade ONERA 7A, while the results presented in Fig.6.18 are for the ONERA 7AD rotor with blades of advanced design. The OASPL are about 2dBA lower than the ones in Fig.6.17 and also the extension of the dark red region, i.e. higher dBA levels on the rotor advancing, is smaller which suggest that the 7AD design is able to lower some of the BVI noise.

Both characteristics described above are captured also by the computational results which are in fair agreement with the directivity patterns of the measurements, but it is visible a shift of about 40 deg in the maximum OASPL in the patterns which is attributed to the difficulties in capturing the complex $3D$ vortex-body interaction problem. The higher discrepancies between the predictions and the measurements are visible in the retreating side of the rotor. This is thought to be connected

with the CT, both CT1 and CT2, which are not able to fully capture the complex aerodynamic phenomena taking place in this region. The oncoming flow is much slower in this region, and hence a degree of flow separation could appear over the blade. The use of Finite Volumes Methods with turbulence modelling could improve the predictions over this region.

It is useful to examine in detail the acoustic pressure time histories on the microphones. This will enable to assess whether the physics of BVI (number of peaks, magnitude and position of the dominant peak) are well captured by the aeroacoustic computations as was the case for the aerodynamic predictions.

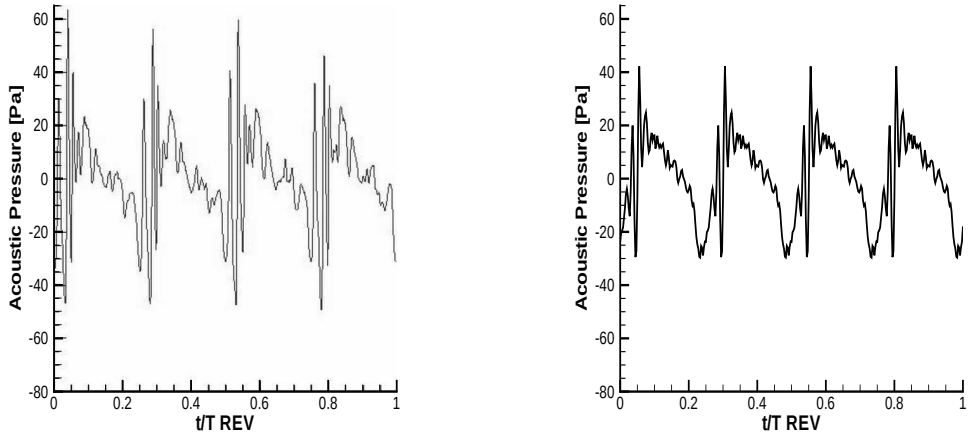

(a) ***Experimental*** **(b)** ***Numerical***

Figure 6.19: Experimental and numerical acoustic pressure time history for the microphone in the advancing side, indicated in figure 6.17 by a black square.

The pressure time histories in Fig.6.19 refer to the microphone, indicated by a black square in Fig.6.17 and 6.18, which is positioned just under the $Psi = 90$ position, i.e. under the rotor advancing side. The Figure shows that the computational chain used here has been able to capture the physics of the BVI phenomena. The number of peaks and the positions of the dominant peak are close to the experimental ones, which is demonstrated also from the frequency spectrum in Fig.6.20(b). Fair agreement is obtained for the magnitude of the peaks, also visible in Fig.6.20(b) where the peaks are appearing at the same frequencies but their magnitudes are underestimated.

For instance, the numerical prediction is about $20dB$ lower for the peak at bpf

$\sim 64Hz$, the highest magnitude peak for the measurements. It should also be noted that the highest peak for the numerical prediction is at a frequency $\sim 780Hz$ which is ~ 12 times the bpf, where the measurements are overestimated of $\approx 5dB$. Thus, the numerical predictions are largely underestimating the amplitude of the BVI peak at bpf which is the main indication of the strength of the blade vortex interaction phenomenon.

As discussed in Subsection 3.1.4, the amplitude of this peak is connected with the oncoming vortex properties: miss distance, vortex strength, position and core size, which are very complex properties to capture via numerical simulation. From the results shown in Fig.6.19 and Fig.6.20 it is clear that some of the aforementioned quantities driving the BVI intensity are not correctly simulated by the aerodynamic prediction codes. While the OASPL footprints in Fig.6.17 and 6.18 have an amplitude difference of around $2dB$, the detailed analysis at one microphone position, Fig.6.19 and Fig.6.20, suggests that a low difference in OASPL can hide lager discrepancies at particularly important frequencies, such as the bpf.

In conclusion, the results obtained from the two computational tool chains presented herein confirm their capabilities to provide aeroacoustic predictions that are overall in fair agreement with the experimental data for the complex phenomenon presented here. Furthermore, from the discussion above is clear that the analysis of OASPL results should always be accompanied by acoustic pressure time histories and SPL frequency spectra at significant microphone positions, such as the microphone at maximum OASPL value.

6.3 Transonic rotor noise

As discussed in Chapter 3, the High Speed Impulsive noise is the main source of rotor noise generation during transonic conditions. The intensity of this phenomenon is a non linear function of the rotor tip Mach number M_T and becomes very intense as the $M_T \longrightarrow 1$. In particular, the HSI intensity is connected with the extension of the supersonic flow pocket which appears over the blade when $M_T \geq M_c$ (aerofoil critical Mach number). In these conditions a shock appears over the upper surface of the blade forming a supersonic flow pocket. With the increase of M_T the extension of the supersonic bubble increases until a shock delocalization appears.

Shock delocalisation was discussed in Section 3.1.3. In Fig. 6.21(a) and (b) the

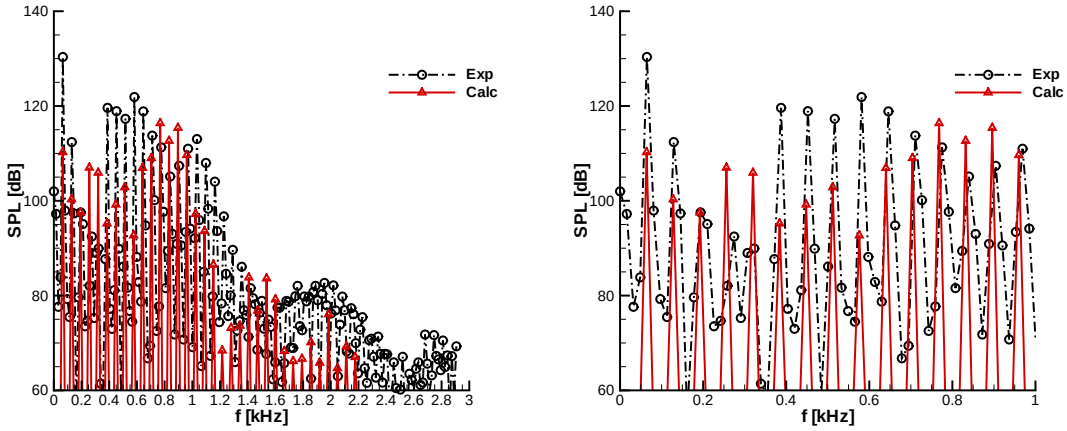

Figure 6.20: Experimental and numerical frequency spectra of the time histories in Fig. 6.19. (a) shows the spectrum for frequencies up to $3kHz$, while (b) shows a zoom in $[0-1]kHz$.

phenomenon is illustrated by means of CFD flow visualisation from the analyses conducted in this research. Fig.6.21(a) shows the extension of the supersonic bubble, in a reference frame rotating with the blade, for $M_T = 0.85$ where there is no delocalisation. In this Figure is also visible the sonic circle, which is defined as the radius beyond which the undisturbed flows appears supersonic to an observer in the blade frame.

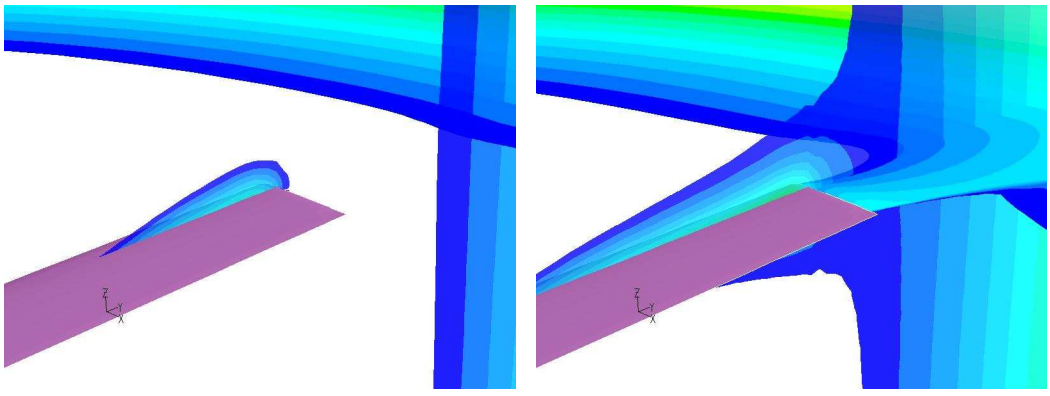

(a) $M_T = 0.85$ ***non delocalised shock*** **(b)** $M_T = 0.95$ ***delocalised shock***

Figure 6.21: Shock delocalisation phenomenon. (dark blue lines $M = 1$)

When the tip Mach number increases, for $M_T \geq 0.92$, the shock bubble extends up to the sonic circle. This is shown in Fig. 6.21(b), for $M_T = 0.95$, where the shock bubble is connected with the sonic circle and the strong pressure disturbance on the

rotor disk plane goes far beyond the sonic circle. The extension of the high pressure gradient is more clear in Figure 6.22.

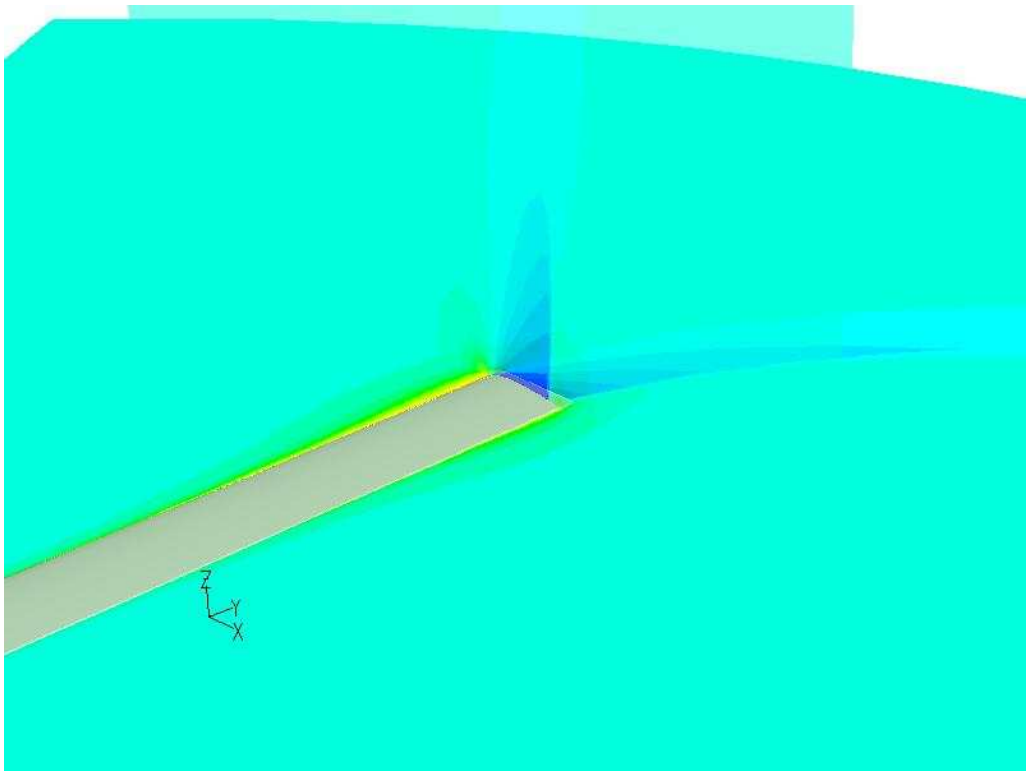

Figure 6.22: Shock distribution in the rotor disk plane

6.3.1 Experiment description

Purcell, [32], identified the importance of HSI noise , which mainly occurs in high speed forward flight conditions, and devised an experimental set-up which allows to obtain HSI and shock delocalisation by using a hovering rotor. The HSI phenomenon can be obtained by considering a hovering rotor with M_T values similar to the advancing tip Mach numbers reached during high speed forward flights.

The experimental study in [32] was conducted in the NASA Anechoic Hover Chamber using a $1/7^{th}$ scale model of the UH1H main rotor, which has straight untwisted blades with NACA 0012 aerofoil sections. The rotor has a blade span of $R_T = 1.044m$ and a constant chord of $ch = 0.0762m$ which gives a blade aspect ratio of $AR = 13.71$. Such a simple blade geometry was intentionally chosen by Purcell in order to produce a database for aeroacoustic code validation. For these reasons the experiment has been exploited by many researchers for validating and

testing the capabilities of rotor noise predictions tools, [38], [44] and [121], [48].

In this experiment were analysed 5 different Mach number values, ranging from $M_T = 0.85$ up to $M_T = 0.95$, hence considering both non-delocalised and delocalised conditions. The acoustic pressure data were measured along the sonic circle, $R = \frac{\Omega}{A_0}$ and at $R = 2.18R_T$ and $R = 3.09R_T$. In the present thesis the aeroacoustic analysis of all the aforementioned flow conditions has been performed using the numerical approach described in the following subsection.

6.3.2 Numerical method

The most important parameters contributing to the overall intensity of HSI sources are the shock position, strength and extension. Hence, the viscous effects play a secondary role for this specific rotor noise source. For these reasons the aerodynamic predictions have been calculated using the $3D$ inviscid Euler solver of the commercial software Fluent. The Euler solver is based on a cell centred finite volume method with Roe Flux-Difference Splitting (FDS) scheme for calculation of the convective fluxes. For the spatial discretisation a second order upwind scheme was adopted.

Other simplifying assumptions can be obtained via a careful consideration of the flow conditions and rotor kinematics:

- The hovering condition implies that the flow is rotationally periodic, thus it is possible to divide the domain in as many sectors as the number of blades and consider only the domain sector surrounding one blade
- The UH1H rotor has symmetric aerofoil sections with angle of attack $\alpha = 0$, i.e. it is possible to analyse only the upper surface of the blade. The combination of the two hypotheses brings the domain extension, and hence the nodes count, to one quarter of the initial domain
- In a reference frame rotating with the blades, the fluid flow around the rotor can be considered steady. This means that using a relative velocity formulation, it is possible to perform steady state CFD calculations instead of unsteady time accurate simulations

It should be noted that the aforementioned assumptions do not bring any approximation to the computed solution. They are not based on a simplification of the model, but on physical considerations on the particular case under analysis.

Following the above assumptions, the chosen domain starts from the rotor disk plane and extends $2R_T$ above this plane and $2.5R_T$ from the rotor hub, i.e. $1.5R_T$ from the blade tip. The domain was discretised using a mesh of $(121x86x52)$ respectively in the chordwise, spanwise and blade normal directions. A grid sensitivity study was also performed to check the dependance of the solution on the number of grid nodes in each direction. Four different meshes were considered, one obtained from the fine mesh considering every other node respectively in the I, thus obtaining a mesh with $(61x86x52)$, a second mesh which has half of the node of the previous one in the I direction, i.e. $(31x86x52)$ and the fourth mesh with $(121x43x52)$, i.e. half the nodes of the fine mesh in the spanwise direction.

In Fig.6.23, are shown the comparisons between the results in Baeder [122] and three meshes from coarse to fine in the chordwise direction. From Fig. 6.23(a) it is clear that the coarse mesh can capture the pressure distribution over the blade with acceptable accuracy. The difference in the predictions between the coarse and the fine mesh becomes much higher further away from the blade. Figure 6.23(b) shows the same comparison at the sonic circle where an underestimation of the peak negative pressure clearly visible. Furthermore, although the shape and the amplitude of the expansion are in reasonable agreement, the position of the shock at the sonic circle is very different between the coarse and fine mesh, while the medium mesh has a much closer agreement to the fine one.

Given the good agreement between the results computed on the fine mesh and the Euler computations for the predicted acoustic pressure at the sonic circle, presented by Baeder [122], the flow solutions presented in the following section were obtained using the fine mesh.

Since the correct prediction of shock delocalisation plays a major role in the calculation of HSI noise, careful consideration was given to the node distribution in the region outside the sonic circle. Usually the grid nodes are clustered around the blade surface and the clustering extends for a short distance span-wise after the blade tip. Using such an approach leads to a well resolved flow field in the proximity of the blade surface, but the accuracy of the solution strongly decreases going further away from the blade.

In effect, the standard clustering, adopted during aerodynamic analysis of fixed and rotating wings, can provide correct results for the position and extension of the supersonic pocket over the blade surface, but it fails in the presence of moderate to strong delocalisation.

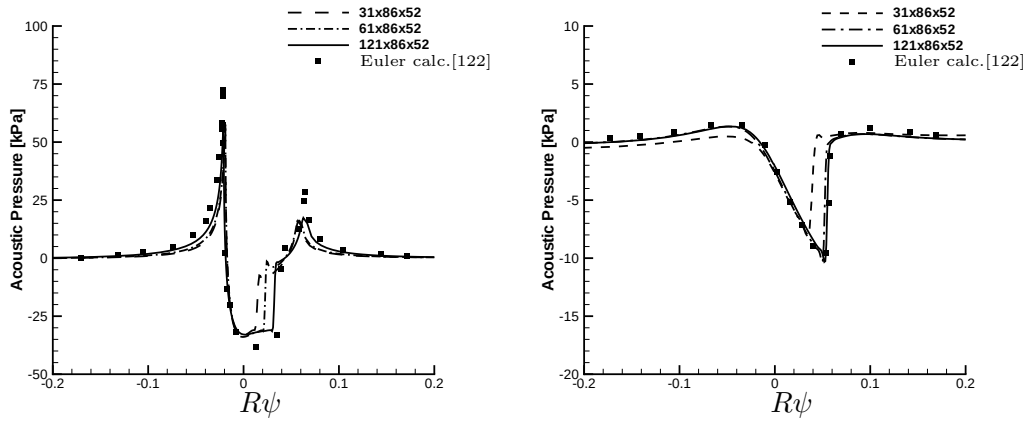

(a) *Acoustic Pressure at* $r = 0.99R_T$ **(b) *Acoustic Pressure at*** $r = R_T/M_T$

Figure 6.23: Grid Sensitivity I direction for $M_T = 0.92$

In order to enhance the accuracy of the CFD prediction in the regions further away from the blade surface, especially in the span-wise direction, the clustering of the nodes must be carefully devised. Isom et al. [123] demonstrated that once a shock reaches the sonic cylinder, it propagates from the contact point along curves with a specific slope. These curves are known as "linear acoustic characteristics", and are defined by the following expressions:

$$x = \frac{c_0}{\Omega}(\cos t + t \sin t) \tag{6.14}$$

$$y = \frac{c_0}{\Omega}(\sin t - t \cos t) \tag{6.15}$$

Equation (6.14) expresses the involute of the sonic circle, i.e. the locus described by a point on a straight line that rolls around the sonic circle. These curves identify the wave front of the propagating shock disturbance. Both Isom et al. [123] and Baeder [38] enhanced the accuracy of their CFD predictions by clustering the grid nodes in the region outside the sonic circle, along the linear characteristic curves.

This same node clustering was exploited in the CFD calculations performed during this study. The final mesh is presented in Fig. 6.24 which shows that the clustering in proximity of the blade and outside the sonic circle is following eq.(6.14). In order to understand the effect of the clustering, the flow was also calculated using a mesh with a conventional clustering, i.e. distributed along straight lines in the region outside the sonic circle.

In Fig.6.25(b) are shown the comparisons of the acoustic pressure predicted using

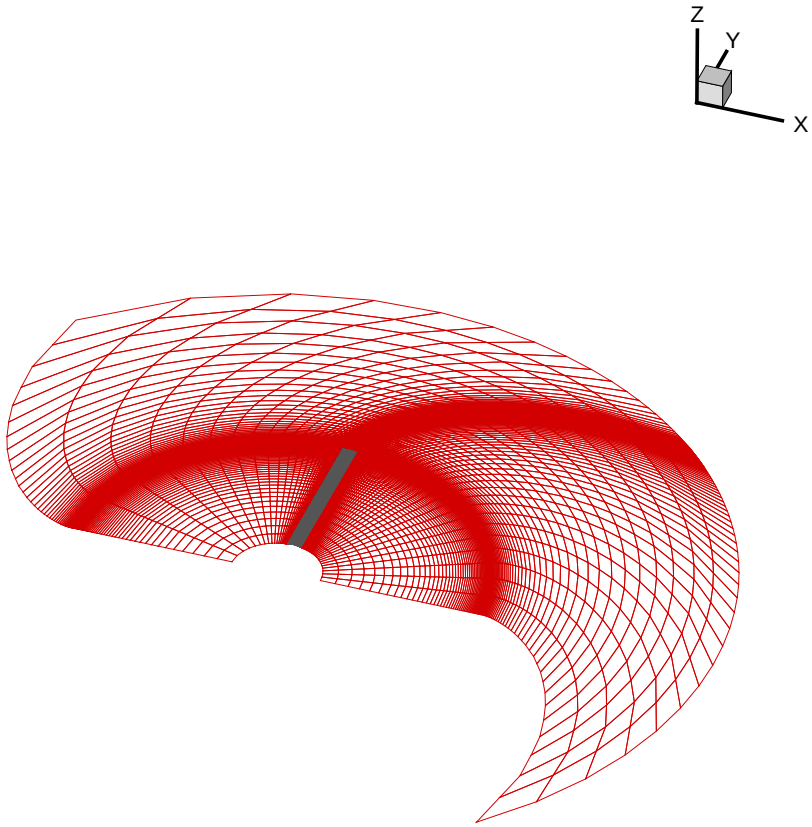

Figure 6.24: Grid nodes distribution on rotor disk plane

the grid clustered along the linear acoustic characteristic, red line, and the one predicted using the grid with the clustering along straight lines, dashed green line. It is obvious that the pressure signal, which compares well at the sonic circle Fig.6.25(a), is completely dissipated because of the lack of grid points along the linear characteristic.

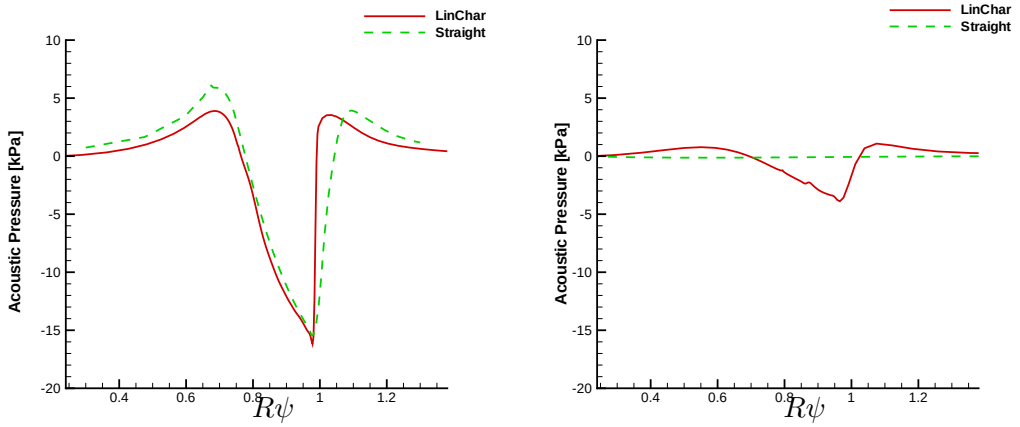

(a) *Acoustic Pressure at* $r = R_T/M_T$ **(b) *Acoustic Pressure at*** $r = 1.5R_T$

Figure 6.25: Comparison of Spanwise Clustering

In the following section the aerodynamic results are presented, followed by the aeroacoustic predictions.

6.3.3 Results

Detailed Aerodynamic measurements are not available from the experiments of Purcell, which were conducted for an aeroacoustic campaign. For this reason, the predicted chordwise pressure distributions are compared to the numerical results presented by Baeder in [38] and [122]. These data have also been used by many researchers, [89],[124], [45] and [41], as the aerodynamic input for their aeroacoustic prediction tools.

The flow conditions considered during this study are based on those of Purcell, [32], with tip Mach numbers ranging from $M_T = 0.85$ to $M_T = 0.95$. The chordwise pressure distribution over the blade, in sections close to the tip, and the relative Mach number contour plots are the most appropriate indicator to identify the supersonic pocket over the blade.

In Fig. 6.26-6.28 are shown the comparisons with the predictions presented in [122].

Each group of Figures is for a different Mach number and shows the chordwise pressure distribution in four position , three over the blade ($r/R_T = 0.89$, 0.95 , 0.99) and one at the sonic circle $r = R_T/M_T = c_0/\Omega$. Observing the plots in Fig.6.26 is clear that the present CFD calculations follow very closely the CFD predictions in [122] for all the positions considered.

Also in Figures 6.27 and 6.28 the predictions are in very good agreement. It should be noted that the magnitudes of the peak negative pressure at the sonic circle is increasing with M_T, 6.26(d), 6.27(d), 6.28(d) and in all cases the current CFD simulation captures both peak values and shape of the pressure wave. As expected from the theory, earlier discussed in Section 3.1.3, the waveform is almost symmetric for $M_T = 0.88$ and becomes increasingly asymmetric at higher M_T as in 6.28(d). While the prediction for non-delocalised conditions, $M_T = 0.85$, does not present many issues, the clustering along the linear acoustic characteristic greatly improves the prediction during delocalised conditions.

The results above prove that the CFD predictions are in good agreement with the results in [122]. It is thus possible to use these data as an input to the noise prediction tool.

Figure 6.29 shows the contribution of the lateral surface to the overall prediction. The lateral surface is indicated in Fig.6.29(a). It is clear that even if the surface is fairly close to the blade its contribution is one tenth of the overall predicted waveform. For this reason it was decided to extend the control surfaces further away form the blade so that the contribution of the lateral surface becomes 0. The End Surfaces chosen as control surfaces extend until the domain's outer boundary, as illustrated in Fig.6.30. These control surfaces are at constant j, spanwise index, and hence at constant relative Mach number M_j which is indicated in this Figure for each surface.

All the control surfaces in Fig.6.30 were used to calculate the predicted sound pressure at an observer $R_{ob} = 3.09R_T$ from the origin of the domain. The results in Fig.6.31 are compared with the experimental data from [32] in order to verify for which of the chosen control surfaces the solution converges closer to the measured data.

Fig.6.31(a) shows a much lower negative peak pressure and a quasi-symmetric waveform shape, which were calculated using both the Retarded Time and the ES formulations. Increasing the relative Mach number M_j, i.e. choosing a control surface further away from the blade tip, the predicted waveform starts to look more like the

measured one. For $M_j = 1.1$, Fig.6.31(b), the predicted waveform is asymmetric following the measured data, but both the negative and positive pressure peaks are overpredicted. Furthermore, in the predicted curve some oscillations are present just after the positive pressure peak.

In Fig.6.31(c), using the surface with $M_j = 1.3$, the predicted waveform is now following the measured data both in shape and in magnitude. Negative and positive pressure peaks are now correctly predicted by the ES algorithm. Using a surface at $M_j = 1.5$ the prediction is not much affected, the shape and the negative pressure peak are correct like in the prediction with $M_j = 1.3$. The only difference is visible in the positive pressure peak which is slightly underpredicted. One possible reason for this could be the clustering in the spanwise direction. For the surface at $M_j = 1.3$ the cell size in the spanwise direction is smaller than the large cells close to the surface at $M_j = 1.5$, and comparable to the zone just after the blade tip clustering, this is visible in Fig.6.30.

From the discussion above it is clear that using a surface at $M_j \geq 1.3$ will ensure that the predicted waveform is not anymore affected by the surface positioning, i.e. all the non linearities in the flow are contained within the control surface. The results for $M_T = 0.92$ and $M_T = 0.95$ using the control surface $M_j = 1.3$ are presented in Fig.6.32 and 6.33 respectively. It should be noted that in these two cases there is a strong shock delocalisation, hence these are the most challenging cases for HSI prediction. The tool developed during this research is capable of capturing very well the shape and peaks in both pressure waveforms for $M_T = 0.92$, Fig.6.32, as opposed to the use of Retarded Time formulation (indicated with HelicA RET in the Figure).

It is evident how the HelicA RET result, calculated along a subsonic porous surface at $M_j = 0.95$ 6.30, under predicts the negative pressure peak and does not capture the asymmetric shape of the experimental pressure wave. On the other hand, HelicA algorithm with ES formulation allows to move the control surface further away from the blade, along the surface at $M_j = 1.3$ 6.30, thus accounting for the non linearities due to the shock delocalisation. The prediction with HelicA ES is in very good agreement with the experiment at $M_T = 0.92$, Fig.6.32, and also at $M_T = 0.95$, Fig.6.33.

In this latter Figure are presented also comparisons with all the other numerical predictions available in literature for supersonic cases, as discussed in Subsection 3.2.8. More precisely in Fig.6.33(a) are shown the comparisons with Brentner et

al. [80], using the Marching Cube Algorithm, with Ianniello [48], which exploits an Emission Surface algorithm called K-algorithm. While in Fig.6.33(b) are shown the comparisons with Delrieux et al. [124], using the Non-Compact forward time algorithm, and with Kessler et al. [90], which exploits a different Non-Compact forward time algorithm.

Clearly all the results in Fig.6.33 follow closely the measured values, but as discussed in Subsection 3.2.8 the results from Ianniello [48], using an ES formulation, can predict the negative peak pressure at the same level as the experimental value and give an very close value also for the peak to peak difference, i.e. the jump from the negative peak to the positive peak. In Fig.6.33(a), HelicA result shows an error level comparable with the one presented in [48] for both the negative peak and the peak to peak difference, which further demonstrates the capabilities of the HelicA prediction tool.

It is not possible to show a precise comparison of the computational effort required by the different methods in literature because the other studies do not provide such information. Computational time values are discussed briefly by Ianniello in [47],[48], but they dependent on the particular computer used and not applicable to a more general comparison, independent from the machine. Some considerations on the computational effort required by different formulations of HelicA are presented in the following Subsection.

6.3.4 Summary and conclusions

In this Chapter the noise prediction tool has been applied to the analysis of three test cases. In the first test case four different semi-empirical vortex models have been implemented in the analysis of aerofoil-vortex interaction. From the analysis is clear that the ΔP difference field between the vortex models is non negligible both for low and high Mach number cases. ΔP is clearly more intense for supercritical conditions and for vortices with very different mathematical form, such as the Taylor and the Scully. The aeroacoustic analysis has shown that the ΔP differences in the far-field acoustic pressures cannot be neglected even for an observer at large distance. Furthermore, differences can be noted in both in SPL magnitude and directivities for different vortex models.

The analysis of the BVI noise test cases shows the capability of the computational tool in the analysis of sources in subsonic conditions. This is confirmed by compar-

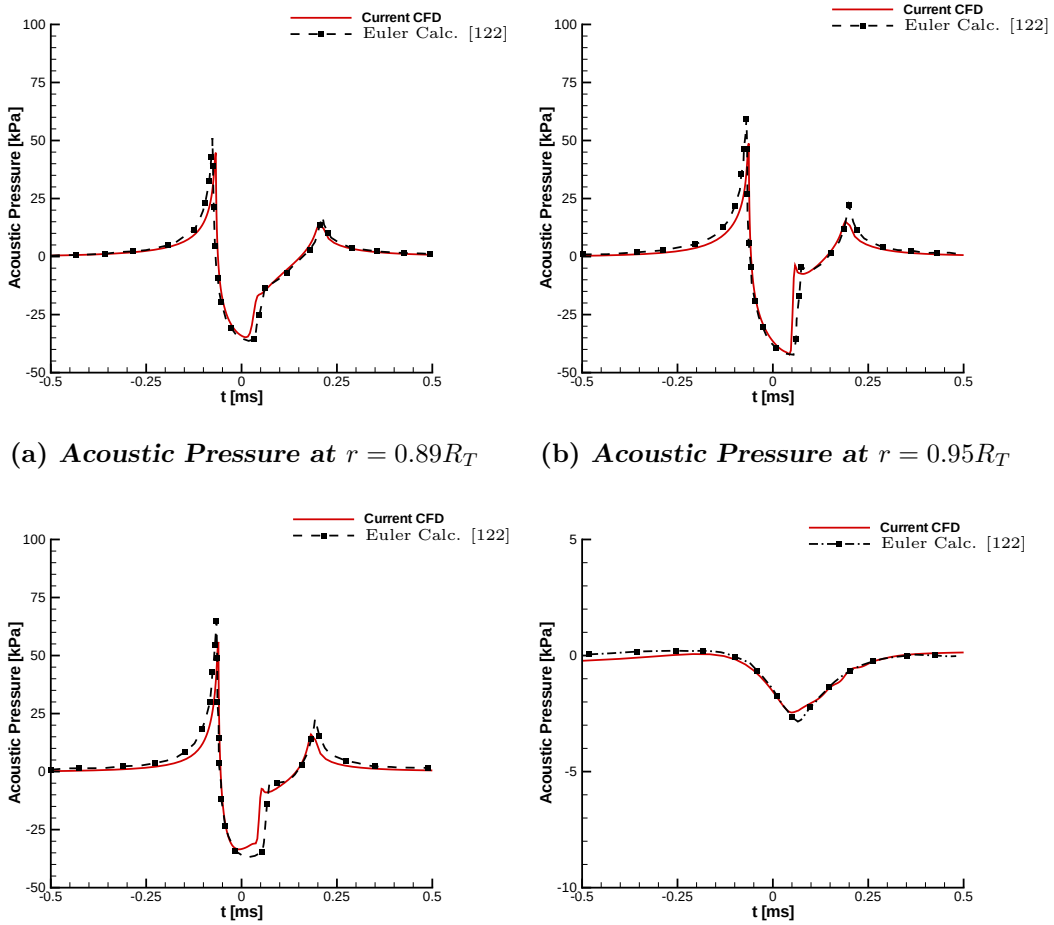

(a) ***Acoustic Pressure at*** $r = 0.89R_T$ (b) ***Acoustic Pressure at*** $r = 0.95R_T$

(c) ***Acoustic Pressure at*** $r = 0.99R_T$ (d) ***Acoustic Pressure at*** $r = R_T/M_T$

Figure 6.26: Comparisons of Acoustic pressure distribution for $M_T = 0.88$

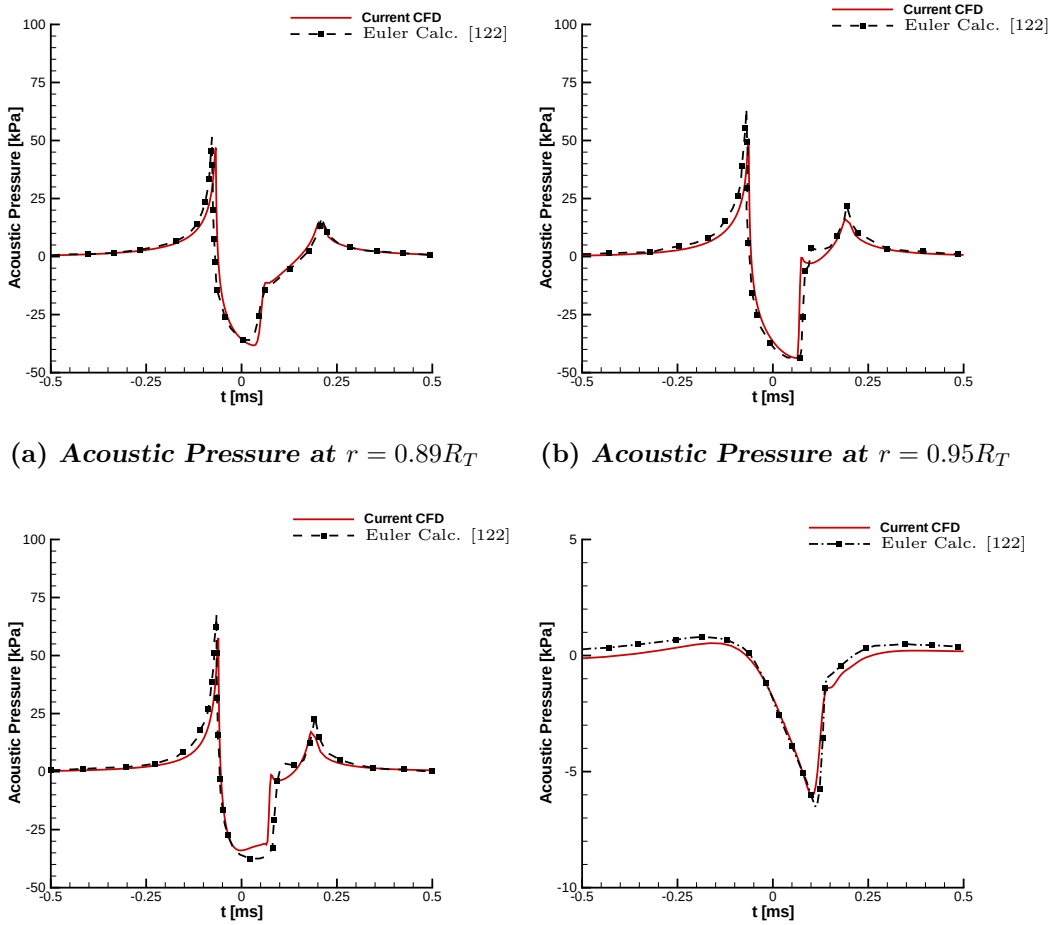

(a) ***Acoustic Pressure at*** $r = 0.89R_T$ (b) ***Acoustic Pressure at*** $r = 0.95R_T$

(c) ***Acoustic Pressure at*** $r = 0.99R_T$ (d) ***Acoustic Pressure at*** $r = R_T/M_T$

Figure 6.27: Comparisons of Acoustic pressure distribution for $M_T = 0.90$

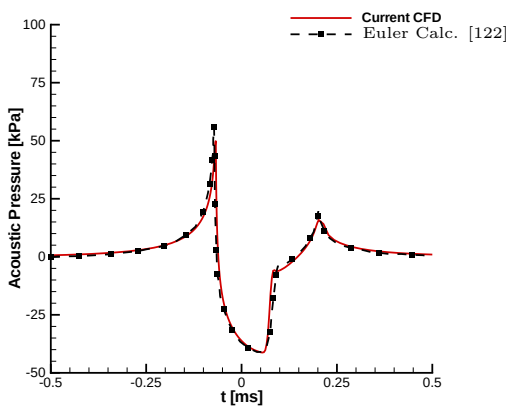

(a) ***Acoustic Pressure at*** $r = 0.89R_T$

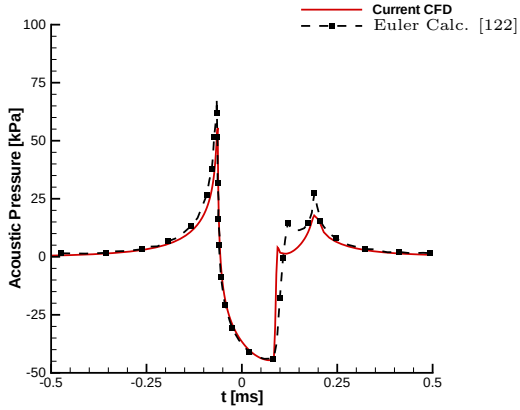

(b) ***Acoustic Pressure at*** $r = 0.95R_T$

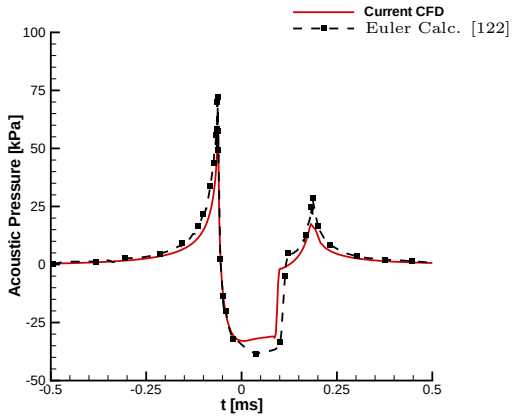

(c) ***Acoustic Pressure at*** $r = 0.99R_T$

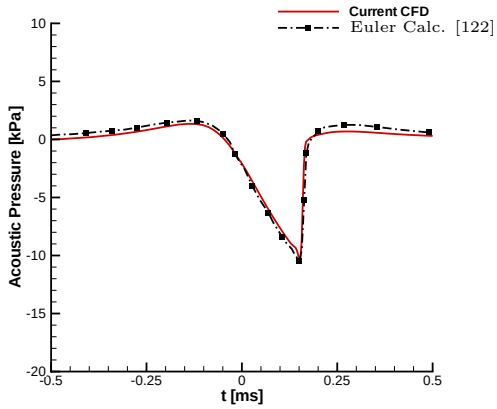

(d) ***Acoustic Pressure at*** $r = R_T/M_T$

Figure 6.28: Comparisons of Acoustic pressure distribution for $M_T = 0.92$

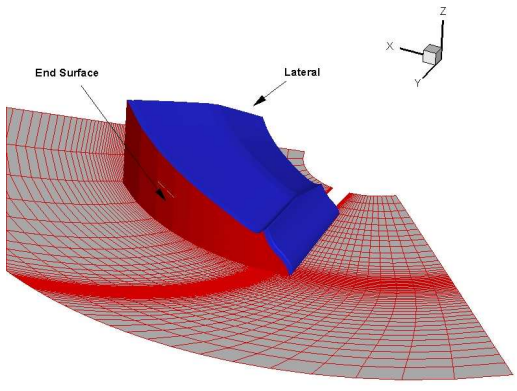

(a)

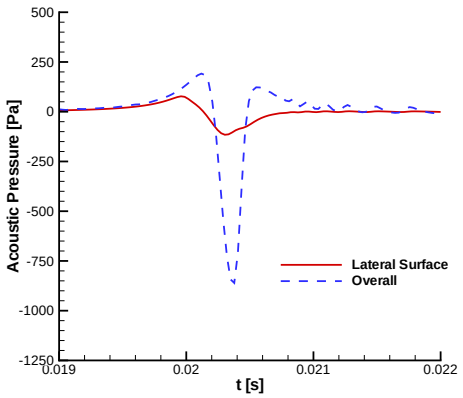

(b)

Figure 6.29: Contribution of Lateral Surface with respect to the overall prediction, (lateral surface at an average distance of 6c from the blade surface)

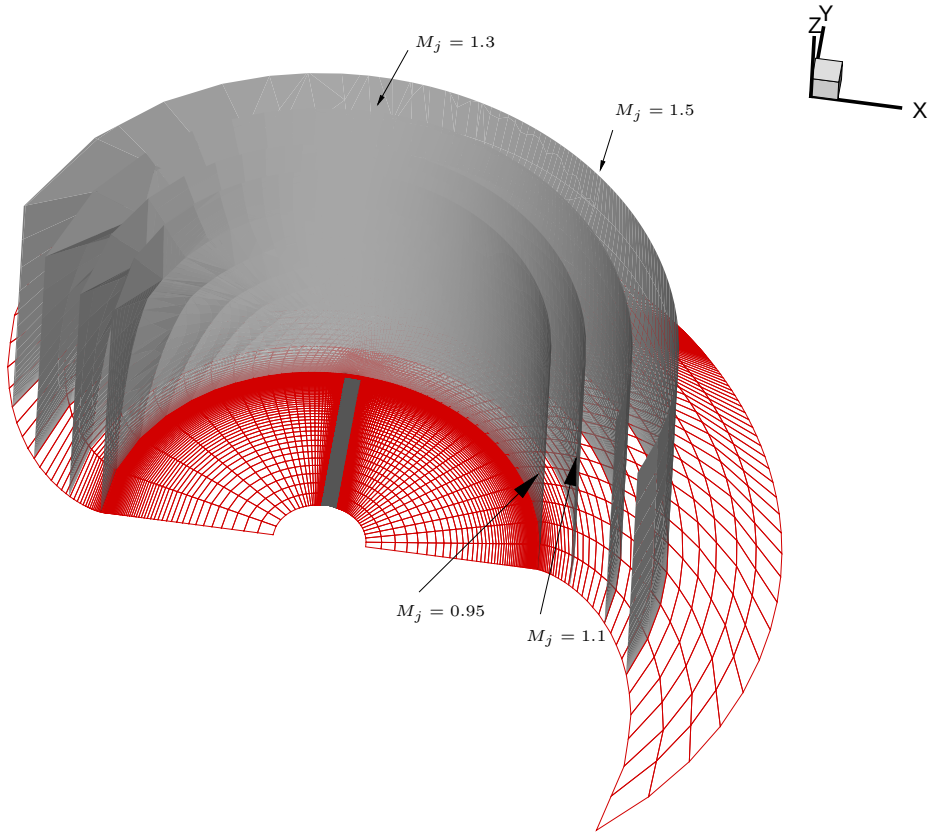

Figure 6.30: Control Surfaces used as input in the FW-H calculations to verify the convergence of the solution, M_j indicates the relative Mach number of the surface at j constant

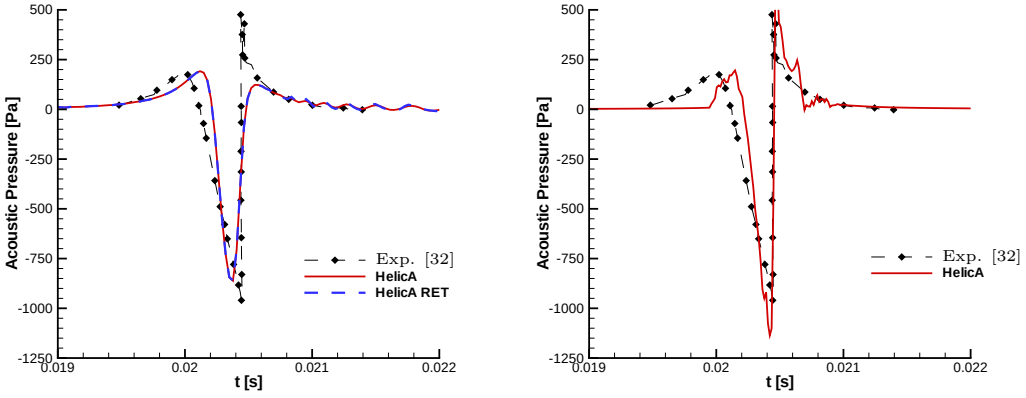

(a) $M_j = 0.95$

(b) $M_j = 1.1$

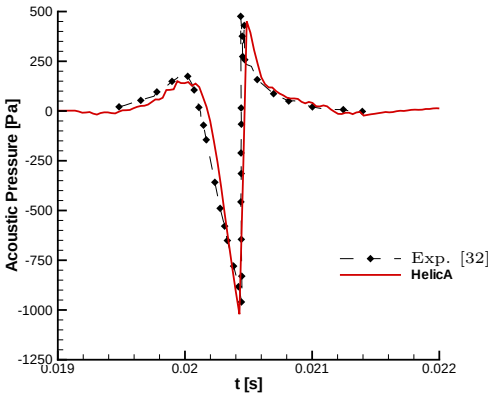

(c) $M_j = 1.3$

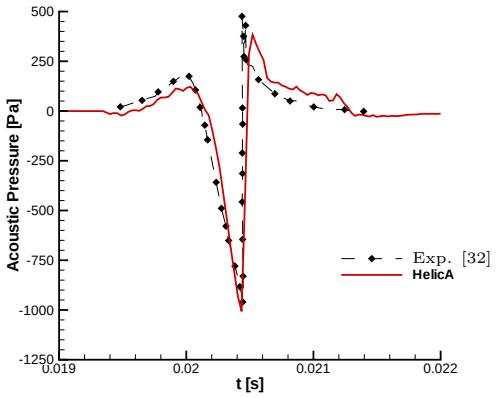

(d) $M_j = 1.5$

Figure 6.31: Comparisons of Acoustic pressure distribution for $M_T = 0.92$ at an observer $\mathbf{X}_{ob} = 3.09R_T$. The different plots are obtained for Control surface positioned further away form the blade starting from $M_j = 0.95$, the only case for which the retarded time formulation is applicable

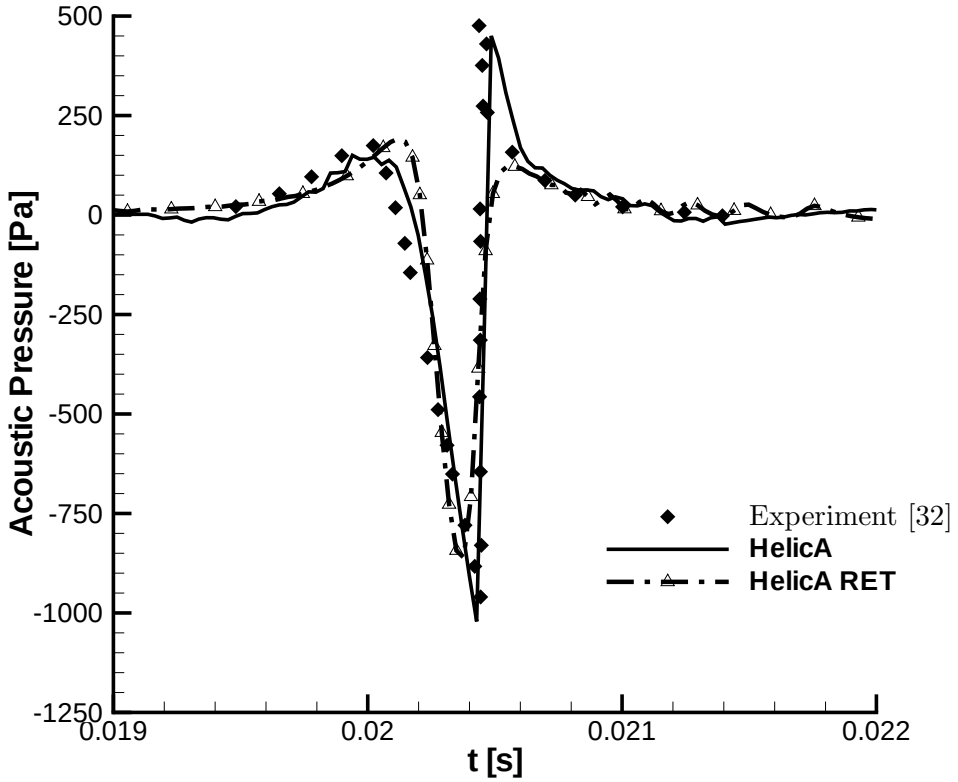

Figure 6.32: Far-field comparisons of Acoustic pressure distribution for $M_T = 0.92$ at $R_{Ob} = 3.09$ (HelicA RET refers to retarded time formulation as opposed to HelicA which is in Emission Surface formulation)

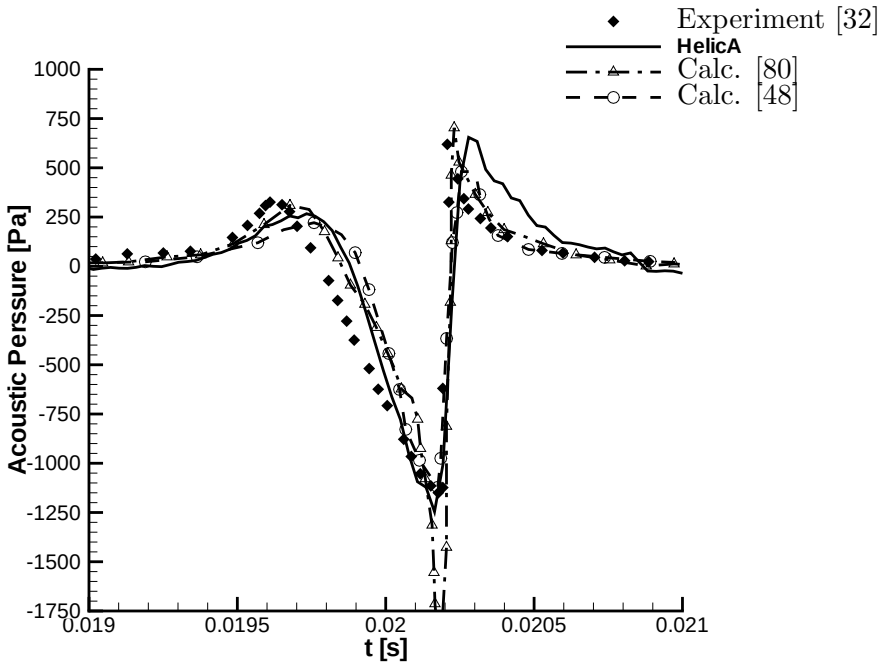

(a)

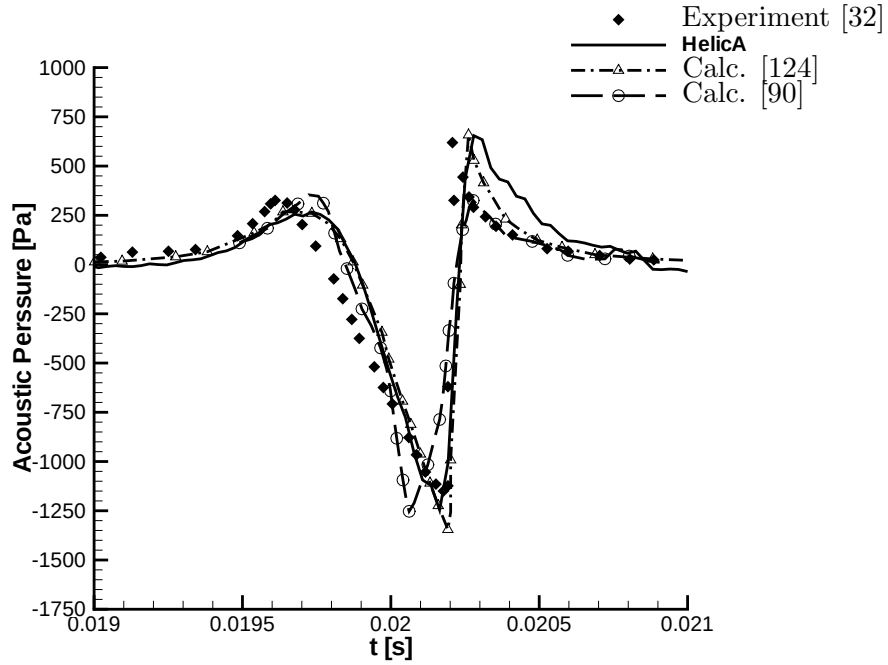

(b)

Figure 6.33: Far-field comparisons of Acoustic pressure distribution for $M_T = 0.95$ at $R_{Ob} = 3.09$

ing the calculated and measured noise footprints and from the good agreement of the computed acoustic pressure time history with that measured at a microphone position close to the maximum OASPL.

The third test case is presented in the last part of the Chapter. This is the analysis of a helicopter's rotor in delocalised conditions rotating at 5 different tip Mach numbers ranging from $M_T = 0.85$ to $M_T = 0.95$. A particular focus is given to the analysis of the cases at $M_T = 0.92$ and $M_T = 0.95$ which present a strong shock delocalisation. These cases are the most challenging for both aerodynamic and aeroacoustic predictions. The use of the porous FW-H in Retarded Time formulation was also explored for the case at $M_T = 0.92$, but the results obtained with this formulation clearly underestimate the negative pressure peak. On the other hand, the results obtained with the HelicA's Emission Surface algorithm on supersonically rotating control surfaces are in very good agreement with the measurements in both $M_T = 0.92$ and $M_T = 0.95$ cases. Using such control surfaces all the non-linearities of the flow are contained in the domain enclosed by the control surface.

From the results presented in Chapter 5 and 6 it is possible to make a comparison between the computational effort required by the HelicA RET, the HelicA ADV and the Helica ES formulations. Comparisons between the time required by the different formulations, for the solution of the retarded time equation, were presented in Fig.5.1. The different formulations have also been applied for the acoustic predictions in Section 6.2, Table 6.3 and finally results from HelicA RET and HelicA ES were compared in the Subsection 6.3.3, Fig.6.32.

From the aforementioned comparisons it is possible to conclude that, for the solution of sources in subsonic motion, the proposed HelicA algorithm in Emission surface formulation, with the improved root finder algorithm, requires a computational time comparable to those required by HelicA RET and HelicA ADV formulations, Fig.5.1. For the solution of sources in supersonic motion the other algorithms based on RET and ADV formulations, because of the Doppler singularity $1 - M_r$, cannot predict the pressure waveforms as well as the HelicA ES algorithm, Fig.6.32.

Chapter 7

Conclusions

This chapter concludes the thesis describing the contribution to knowledge provided and discussing the findings of this research. Furthermore, some limitations of this work are identified and the corresponding future research activities are proposed. Section 7.1 is an outline of the research study. Section 7.2 then presents the accomplishment of the objectives proposed in Chapter 4. Section 7.3 lays out the main contributions of the current study. Finally Section 7.4 discusses the limitations of this work and of the proposed noise prediction tool. These limitations are used to define the future research activities.

7.1 Outline of research study

The aim of this research was to explore the field of computational aeroacoustics prediction applied to rotor generated noise and to develop a computational noise prediction algorithm capable of dealing with noise sources in both subsonic and transonic/supersonic regimes.

Noise prediction for rotating sources in transonic/supersonic regimes is difficult to accomplish because the classical Retarded Time Formulation is affected by the Doppler singularity for $M_r = 1$ and cannot be applied in these conditions. For this reason it is required the use of either Collapsing Sphere or Emission Surface Formulations which have the added complexity of a time dependent integration domain. Furthermore, as discussed in Chapter 4, the existence of multiple τ roots for one single observer instant t renders the solution of the retarded time equation by means of classical root finder algorithms, almost impossible.

In order to achieve the aforementioned research aim, the current research was based on the following methodological steps: first a literature survey was conducted in order to identify the current state of the art methodologies for both subsonic and transonic/superonic rotating sources; then a detailed analysis of the kinematics of rotating sources and helicopter rotor blades was performed, which helped to understand in more depth the retarded time equation. It was then possible to analyse the behaviour of this equation for rotating sources in both subsonic and transonic/superonic regimes and to identify a novel method for obtaining the τ roots more efficiently. This latter method was then implemented in a noise prediction tool based on the Emission Surface formulation, which was verified and validated benchmarking against results available in literature. Finally the tool was applied to the analysis of three experimental campaigns.

7.2 Accomplishment of research objectives

In Chapter 4 the aim and objectives of this thesis were defined. In this section we discuss the steps undertaken for the accomplishment of research objectives.

To carry out a literature survey in order to identify the current state of the art in noise prediction algorithms for external noise applications
An extensive literature survey was performed and presented in Chapter 3. With the help of this survey it was then possible to define the current state of the art in noise prediction algorithms and to identify the existing research gaps.

To develop a computational prediction tool based on the state of the art algorithms identified in the literature survey
Following the literature survey the novel noise prediction tool was developed starting from the state of the art algorithms which were identified

To create a novel algorithm for transonic and supersonic sources and incorporate it in the noise prediction tool
The algorithm and its components are defined in Chapter 4. In this chapter, a detailed discussion is presented on the different parts of the newly developed algorithm, i.e. the root finder algorithm, the kinematics module, the quadrature methods and the Emission Surface construction algorithm.

To identify specific verification and validation cases for both subsonic and transonic/supersonic regimes

Based on the review presented in Chapter 3 the test cases were identified and described in the Chapters 5 and 6.

To validate the noise prediction tool for the selected cases

Along with the description of the chosen cases in Chapters 5 and 6 the results that have been obtained with the noise prediction tool are presented and compared to the data available in literature.

7.3 Research Contributions

The following points highlight the contribution to knowledge as a result of this work. This study fills in the research gaps which were identified from the literature survey.

Identification of the currently used approaches for rotating sources in transonic/supersonic regimes

Using a literature survey the current state of the art approaches and algorithms used for the noise prediction of rotating sources were identified. In the case of sources in subsonic regime the wide use of Retarded Time formulations based on the Farassat Formulation 1A was highlighted. The majority of the codes based on this approach use the Retarded Time algorithms while only few are based on the Advanced Time algorithm. On the other hand, only few algorithms are capable of handling sources in transonic/supersonic regime in time domain. More precisely, in literature 5 noise prediction tools for these conditions have been identified. Two are based on the Emission Surface formulation, [44] and [45], the first of which exploits an Advanced Time approach and the "Marching Cubes algorithm" from computer graphics while the second uses a sophisticated retarded time algorithm, named "K-algorithm". Only one Collapsing Sphere algorithm, [88, 43] and finally two "Non-Compact" Advanced Time algorithms, [89] and [90].

Detailed analysis of retarded time equation in the two flow regimes

In the literature survey there was clear the lack of a detailed analysis on the retarded time equation $g(t, \tau, r) = 0$, especially in the case of sources moving or rotating in transonic/supersonic regime. By focusing on the kinematics of single point and then of a panel, rotating from subsonic up to high supersonic

conditions, it was possible to illustrate the behaviour of the τ roots of this equation. It was found that the multiple ES branches of a source with finite extension, such as a panel, will "appear" and "collapse" in a single point at those locations, along their path, where $1 - M_r = 0$. Furthermore, some more insights on the τ roots were gained by observing both $\frac{\partial g}{\partial \tau}$ and $\frac{\partial^2 g}{\partial \tau^2}$, first and second partial derivatives of g.

Definition of a root finder algorithm for supersonically rotating sources

Following the analysis of $g(t, \tau, r) = 0$, and the behaviour of its τ roots, a novel root finder algorithm was defined. This algorithm is capable efficiently providing the τ roots of g by literally "tracking" the curves $\tau(t)$ even in the presence of multiple roots.

Implementation of the proposed root finder algorithm

The aforementioned algorithm was then implemented and applied to the solution of $g(t, \tau, r) = 0$ in the case of points rotating from subsonic to supersonic speeds. The implementation was carried out by exploiting the solution of the 3^{rd} order polynomials proposed by Nickalls, [95]. To the knowledge of the author it is the first time that this solution is exploited in the current field. The proposed root finder algorithm was the compared with the classical Newton's and Brent's methods which are usually exploited for the solution of the retarded time equation. In Chapter 5 it was shown that the efficiency of the proposed method is comparable to the efficiency of the Advanced Time algorithm and the method is in some cases more than 5 times faster than the two classical root finder algorithms.

Development and implementation of the Noise Prediction tool

During this study a noise prediction tool named Helic(opter)A(coustics) and based on the ES formulation was developed. This tool exploits the above mentioned findings and the proposed root finder algorithm. In this way the ES construction algorithm results simpler than the "K-algorithm" in [45]. The noise prediction tool is verified and validated using test cases available in literature, and the comparisons in Chapter 5 shows good agreement between the results. More precisely, the accuracy of the tool was demonstrated by comparing the results with the analytical solutions for $3D$ monopole, dipole and quadrupole sources. This study highlighted the numerical errors produced by both spatial and temporal discretisations, which remain under $\varepsilon < 3\%$, even for coarse surface meshes with $\Delta L_{max} \leq 0.05$ and become $\varepsilon_{av} < 1\%$ for $\Delta L_{max} \leq 0.01$. This is similar for all the quadrature methods analysed,

i.e. Midpoint, Simpson and Gauss-Legendre quadratures, with the difference that the latter two methods reach $\varepsilon \leq 1\%$ for higher values $\Delta L_{max} \leq 0.1$. The comparisons suggested the used of Midpoint quadrature in the cases of a discretisation with $\Delta L_{max} \leq 0.05$. This is because of its efficiency and the fact that the other two methods give only slightly higher accuracies but at a much higher computational time. The capabilities of the Emission Surface construction algorithm were tested on a rotating cylindrical strip, [48], a supersonically rotating blade planform, [99] and on a supersonically rotating panel with $\Lambda = 0$ singularity. In all cases the tool was capable of capturing the correct shapes and topologies of the corresponding Emission Surfaces. Finally the noise prediction tool was applied to the analysis of three experimental campaigns, [114], [17] and [32]. In these analyses the results obtained, Chapter 6, were in fair agreement with the measurements for the $3D$ BVI and in good agreement with [32], for the HSI noise test case. It should be highlighted that in Section 6.3, the comparisons with the measurements [32] is presented for the cases with stronger shock delocalisation, $M_T = 0.92$ and $M_T = 0.95$, hence the most difficult tests for aeroacoustic prediction. For the analysis of the first condition also the classical Farassat Formulation 1A was applied, with a Retarded Time algorithm, on a Control Surface rotating at subsonic speed, $M_j = 0.95$. It was demonstrated that using this S_C the non linear terms pass through the surface and the noise prediction is underestimated. While using the ES formulation on a S_C at $M_j = 1.3$ all the non linearities are contained in S_C and the prediction is in very good agreement with the measurements.

7.4 Future work

The research was focused only on the analysis of rotating sources and in particular on helicopter rotors From the Introduction Chapter is clear that a more general scope for future research could be on Open Rotors. These form a general class containing Wind Turbines, Turboprop engines, Tilt rotor, helicopter rotors and high speed Propfans. It is evident that a generalised research on the full range of open rotors would be impossible, but it would be interesting to analyse each of these rotary machines separately. It should be noted that Propfans are under the attention of many current research efforts to obtain more efficient aircraft engines. Despite the attractive efficiency, Propfan rotates at high speed and in the regions close to the tip are often present supersonic conditions. Furthermore, all

the proposed Propfan configurations are based on double counter rotating rotors, so that both BVI and HSI phenomena affect these engines. For these reasons, the noise prediction tool developed during this research would be very well suited for the analysis of supersonically rotating flow around Propfans. Another very interesting application, pointed out in the Introduction, is the $X2$ helicopter rotor concept. This exploits two axial counter rotating rotors in order to reach higher forward flight speed without being affected by the asymmetric flows which penalises the classical helicopter main-rotor configurations. Given the high speeds at which these rotors would fly it is certain that HSI phenomena will arise. An aerodynamic and aeroacoustic research on this novel concept will be helpful to highlight both performance and noise characteristics of such rotors. It should be noted that although the noise prediction tool was developed and tested for rotating sources, HelicA could be applied with minor modifications to other kind of problems, such as the analysis of Jet Noise.

The presented test cases did not include any HSI analysis in forward flight An Euler/N-S CFD tool which could handle the complex kinematics of the helicopter rotor in forward flight and which could be coupled with a comprehensive code for aeroelastic analysis was not available at Cranfield University during the course of this study, . If in the future such a coupled code becomes available, the analysis of helicopter in forward flight in HSI conditions could be accomplished. This would bring more insight into such complex phenomena and could be used to improve the design of helicopter rotors to handle these conditions.

The algorithm was defined to handle unstructured surface grids This is clearly an advantage when using unstructured gird and data such as the output file format of Fluent computations. Future research efforts could aim at optimising the handling of the surface grids and data structures which would improve the performance and the efficiency of the specific noise prediction tool. In the presence of structured (i, j) nodes and data distributions it would be possible to save computational time. Furthermore, even though the current tool can perform automatic grid adaptations both in space and time, it lacks a smoothing procedure for the generated Emission Surfaces. Such a procedure was exploited in [48] and it was shown to yield smoother pressure waveforms. Further investigation on how to improve the Emission Surface construction at low computational cost would be of great interest.

References

[1] A. F. Demming, "Noise from propellers with symmetrical sections at zero blade angle," *NACA TM 679*, 1938.

[2] W. Ernsthausen, "The source of propeller noise," *NACA TM 825*, 1937.

[3] L. Gutin, "On the sound of a rotating airscrew," *NACA TM 1192*, 1948.

[4] I. E. Garrick and C. E. Watkins, "A theoretical study of the effect of forward speed on the free-space sound-pressure field around propellers," *NACA Report 1198*, 1954.

[5] M. V. Lowson, "The Sound field of singularity in motion," *Proceedings of the Royal Society*, vol. A268, pp. 559–572, 1965.

[6] S. E. Wright, "Sound Radiation from a Lifting Rotor Generated by Asymmetric Disk Loading," *Journal of Sound and Vibration*, vol. 9, pp. 223–240, 1969.

[7] M. V. Lowson and B. J. Ollerhead, "A Theoretical Study of Helicopter Rotor Noise," *Journal of Sound and Vibration*, vol. 9, pp. 197 – 222, 1969.

[8] M. J. Lighthill, "On Sound Generated Aerodynamically - 1. General Theory," *Proceedings of the Royal Society of London, Series A, Mathematical and Physical Sciences*, vol. 211, no. 1107, pp. 564–587, 1952.

[9] M. J. Lighthill, "On Sound Generated Aerodynamically - 2. Turbulence as a Source of Sound," *Proceedings of the Royal Society of London, Series A, Mathematical and Physical Sciences*, vol. 222, no. 1148, pp. 1–32, 1954.

[10] M. J. Lighthill, "The Bakerian Lecture, 1961. Sound Generated Aerodynamically," *Proceedings of the Royal Society of London, Series A, Mathematical and Physical Sciences*, vol. 267, no. 1329, pp. 147–182, 1962.

[11] J. E. Ffowcs Williams and D. L. Hawkings, "Sound Generation by Turbulence and Surfaces in Arbitrary Motion," *Philosophical Transactions of the Royal Society of London. Series A, Mathematical and Physical Sciences*, vol. 264, no. 1151, pp. 321–342, 1969.

[12] D. L. Hawkings and M. V. Lowson, "Theory of Open Supersonic Rotor Noise," *Journal of Sound and Vibration*, vol. 36, no. 1, pp. 1–20, 1974.

[13] F. Farassat, "Theory of Noise Generation from Moving Bodies with an Application to Helicopter Rotors," tech. rep., NASA TR R-451, 1975.

[14] O. J. Childress, "The NASA/AHS Rotorcraft Noise Reduction Program," *Vertiflite*, vol. 34, pp. 18–22, 1988.

[15] B. L. Gmelin, H. H. Heller, E. Mercker, J. J. Philippe, J. S. Preisser, and Y. H. Yu, "The HART Programme, a Quadrilateral Cooperative Research Effort," in *51st American Helicopter Society Annual Forum, Ft. Worth, TX*, 1995.

[16] W. Splettstoesser, G. Niesl, F. Cenedese, F. Nitti, and D. Papanikas, "Experimental Results of the European HELINOISE Aeroacoustic Rotor Test in the DNW," in *19th European Rotercraft Forum, Cernobbio (Como), Italy, 14.-16. September 1993*, 1993.

[17] K.-J. Schultz, W. Splettstoesser, B. Junker, W. Wagner, G. Arnaud, E. Scholl, and D. Fertis, "A Parametric Windtunnel Test on Rotorcraft Aerodynamics and Aeroacoustics (Helishape) - Test Procedures and Representative Results," *The Aeronautical Journal*, vol. 101, no. 1004, pp. 143 – 154, 1997.

[18] P. Renzoni, A. D'Alascio, N. Kroll, and D. Peshkin, "EROS: a common European Euler code for the analysis of the helicopter rotor flowfield," *Progress in Aerospace Sciences*, vol. 36, pp. 437–485, Aug. 2000.

[19] A. Kokkalis, M. Righi, and A. Pagano, "ROSAA - A first step in meeting the rotorcraft industry's need for advanced aeromechanics in rotorcraft simulation systems," in *Computational fluid dynamics '98; Proceedings of the 4th European Computational Fluid Dynamics Conference*, vol. 2, Sept 1998.

[20] Heliflow-Consortium, "Improved Experimental and Theoretical Tools for Helicopter Aeromechanic and Aeroacoustic Interactions - HELIFLOW Synthesis Report," tech. rep., European Commission, 2002.

[21] B. G. van der Wall, C. L. Burley, Y. Yu, H. Richard, K. Pengel, and P. Beaumier, "The HART II test measurement of helicopter rotor wakes," *Aerospace Science and Technology*, vol. 8, no. 4, pp. 273–284, 2004.

[22] J. Yin, B. G. van der Wall, and S. Oerlemans, "Representative Test Results from HELINOVI Aeroacoustic Main Rotor/Tail Rotor/Fuselage Test in DNW," in *31st ERF 2005, P42*, 09 2005.

[23] Friendcopter-Consortium, "Friendcopter Project Description of Work," internal report, Friendcopter Consortium, 2005.

[24] C. Bolkcom, "V-22 Osprey Tilt-Rotor Aircraft," report of the panel to review the v-22 program, U.S. Department of Defense, 2001.

[25] C. V. Pena, "V-22: Osprey or Albatross?," *Foreign Policy Briefing*, no. 72, 2003.

[26] E. Wood, "V/STOL," *AEROSPACE AMERICA*, pp. 22–23, December 2005.

[27] A. Garcia, "Sustainable Aviation," in *ASD, Aerospace and Defence Annual Convention*, 2007.

[28] B. J. Gordon, "The development of the unducted fan," *Aerospace (UK)*, vol. 15, pp. 22–26, July 1988.

[29] N. T. Birch, "2020 VISION - The prospects for large civil aircraft propulsion," in *International Congress of Aeronautical Sciences, 22nd*, Sept. 2000.

[30] P. Schimming, "Counter rotating fans - An aircraft propulsion for the future?," *Journal of Thermal Science*, vol. 12, pp. 97–103, May 2003.

[31] N. Kehayas, "Aeronautical technology for future subsonic civil transport aircraft," *Aircraft Engineering and Aerospace Technology: An International Journal*, vol. 79, no. 6, pp. 600–610, 2007.

[32] T. W. Purcell, "CFD and Transonic Helicopter Sound," in *Fourteenth European Rotorcraft Forum, Paper 2*, Sept. 1988.

[33] F. H. Schmitz, "Rotor noise," in *NASA. Langley Research Center, Aeroacoustics of Flight Vehicles: Theory and Practice. Volume 1: Noise Sources p 65-149* (H. H. Hubbard, ed.), vol. 1, pp. 65–149, Aug. 1991.

[34] F. Farassat, "Extension of Isom's thickness noise formula to the near field," *Journal of Sound Vibration*, vol. 67, pp. 280–+, Nov. 1979.

[35] K. S. Brentner, "Prediction of Helicoptr Rotor Discrete Frequency Noise," tech. rep., NASA TM-87721, 1986.

[36] F. Farassat, R. J. Pegg, and D. A. Hilton, "Thickness Noise of Helicopter Rotors at High Tip Speeds," tech. rep., AIAA Paper No. 75-453, NASA Langley Technical Report Server, 1975.

[37] D. A. Boxwell, F. H. Schmitz, W. R. Splettstoesser, and K. J. Schultz, "Model Helicopter Rotor High-Speed Impulsive Noise: Measured Acoustics and Blade Pressures," tech. rep., NASA, 1983. NASA TM-85850.

[38] J. Baeder, "Euler Solutions to Non Linear Acoustics of Non-Lifting Hovering Rotors," in *16th European Rotorcraft Forum*, Sept. 1990.

[39] F. Farassat and K. S. Brentner, "The uses and abuses of the acoustic analogy in helicopter rotor noise prediction," *Journal of the American Helicopter Society*, vol. 33, no. 1, pp. 29–36, 1988.

[40] F. Farassat and K. S. Brentner, "Supersonic Quadrupole Noise Theory For High-Speed Helicopter Rotors," *Journal of Sound and Vibration*, vol. 218, no. 3, pp. 481–500, 1998.

[41] K. S. Brentner and P. C. Holland, "An Efficient and Robust Metod for Computing Quadrupole Noise," *Journal of the American Helicopter Society*, vol. 42, no. 2, pp. 172–181, 1997.

[42] F. Farassat, *The evolution of methods for noise prediction of high speed rotors and propellers in the time domain*, pp. 129–147. Recent advances in aeroacoustics (A87-11766 02-71). New York, Springer-Verlag, 1986, p. 129-147., 1986.

[43] F. Farassat, "Prediction of advanced propeller noise in the time domain," *AIAA Journal*, vol. 24, pp. 578–584, Apr. 1986.

[44] K. S. Brentner, "A new algorithm for computing acoustic integrals," in *Proceedings of the IMACS 14th World Congress on Computational and Applied Mathematics*, vol. 2, pp. 592–595, 1994.

[45] S. Ianniello, "Algorithm to integrate the Ffowcs Williams-Hawings equation on supersonic rotating domain," *AIAA Journal*, vol. 37, no. 9, pp. 1040–1047, 1999.

[46] S. Ianniello, "Quadrupole noise predictions through the FWH equation," *AIAA Journal*, vol. 37, no. 9, pp. 1048–1054, 1999.

[47] S. Ianniello, "Aerocoustic analysis of high tip-speed rotating blades," *Aerospace Science and Technology*, vol. 5, no. 3, pp. 179–192, 2001.

[48] S. Ianniello, "New perspectives in the use of the Ffowcs Williams Hawkings equation for aeroacoustic analysis of rotating blades," *Journal of Fluid Mechanics*, vol. 570, pp. 79–127, 2007.

[49] J. Prieur and G. Rahier, "Aeroacoustic integral methods, formulation and efficient numerical implementation," *Aerospace Science and Technology*, vol. 5, no. 7, pp. 457–468, 2001.

[50] J. W. Leverton and F. W. Taylor, "Helicopter Blade Slap," *Journal of Sound and Vibration*, vol. 4, 1966.

[51] F. H. Schmitz and D. A. Boxwell, "In flight Far-Field Measurement of Helicopter Impulsive Noise," *Journal of the American Helicopter Society*, vol. 21, pp. 2–16, Oct. 1976.

[52] D. A. Boxwell and F. H. Schmitz, "Full-Scale Measurements of Blade-Vortex Interaction Noise," *Journal of the American Helicopter Society*, vol. 27, pp. 11–27, Oct. 1982.

[53] M. B. Horner, E. Saliveros, A. Kokkalis, and R. A. Galbraith, "Results from a Set of Low Speed Blade-Vortex Interaction Experiments," *Experiments in Fluids*, vol. 14, 1993.

[54] C. Kitaplioglu and F. X. Caradonna, "Aerodynamics and Acoustics of Blade-Vortex Interaction using an Independently Generated Vortex," in *American Helicopter Society Aeromechanics Specialists Conference*, 01 1994.

[55] S. E. Widnall, "Helicopter Noise Due to Blade-Vortex Interactions," *Journal of the Acoustical Society of America*, 1971.

[56] J. D. Baeder and G. R. Srinivasan, "Computational Aeroacoustic Study of Isolated Blade-Vortex Interaction Noise," in *American Helicopter Society Aeromechanics Specialists Conference*, 01 1994.

[57] T. F. Brooks, M. A. Marcolini, and D. S. Pope, "Main rotor broadband noise study in the DNW," in *AHS, National Specialists' Meeting on Aerodynamics and Aeroacoustics, Paper. 12 FAA-Army-supported research.*, Feb. 1987.

[58] T. Brooks, S. D. Pope, and M. Marcolini, "Airfoil Self-Noise and prediction," nasa reference publication 1218, NASA, 1989.

[59] F. Magagnato, E. Sorguven, and G. M., "Far field noise prediction by large-eddy simulation and FfowcsWilliams and Hawkings analogy," in *AIAA paper 2003-3206, 9th AIAA/CEAS Aeroacoustics Conf*, May 2003.

[60] M. C. Jacob, J. Boudet, D. Casalino, and M. Michard, "A rod-airfoil experiment as a benchmark for broadband noise modeling," *Theoretical and Computational Fluid Dynamics*, vol. 19, pp. 171–196, July 2005.

[61] T. F. Brooks and C. L. Burley, "Rotor broadband noise prediction with comparison to model data," in *AIAA/CEAS Aeroacoustics Conference and Exhibit, paper AIAA-2001-2210*, pp. 1–16, May 2001.

[62] P. J. Moriarty, G. Guidati, and P. G. Migliore, "Recent Improvement of a Semi-Empirical Aeroacoustic Prediction code for Wind Turbines," in *Proceedings of 10th AIAA/CEAS Aeroacoustics Conference*, (Manchester, United Kingdom), 2004. AIAA 2004-3041.

[63] M. Roger, S. Moreau, and M. Wang, "An analytical model for predicting airfoil self-noise using wall pressure statistics," in *Center for Turbulence Research Annual Briefs*, 2002.

[64] B. Mitchell, S. Lele, and P. Moin, "Direct computation of the sound generated by vortex pairing in an axisymmetric jet," *Journal Fluid Mech*, vol. 383, pp. 113–142, 1999.

[65] J. Freund, S. Lele, and P. Moin, "Direct simulation of Mach 1.92 jet and its sound field," in *4th AIAA/CEAS Aeroacoustics Conference, AIAA Paper 98-2291*, June 1998.

[66] C. Bogey and C. Bailly, "Direct computation of the sound of a high Reynolds number subsonic jet," in *CEAS workshop from CFD to CAA*, p. 121, Nov. 2002.

[67] X. Jiang, E. J. Avital, and K. H. Luo, "Direct computation and aeroacoustic modelling of a subsonic axisymmetric jet," *Journal of Sound Vibration*, vol. 270, pp. 525–538, Feb. 2004.

[68] S. B. Pope, *Turbulent Flows*. Turbulent Flows, by Stephen B. Pope, pp. 806. ISBN 0521591252. Cambridge, UK: Cambridge University Press, September 2000., Sept. 2000.

[69] S. Sarkar and M. Hussaini, *Computation of the Acoustic Radiation from Bounded Homogeneous Flows*, pp. 335–355. Computational Aeroacoustics (Editors: J. Hardin and M. Hussaini), Springer-Verlag, 1993.

[70] C. Bogey and Bailly, "Contributions of Computational Aeroacoustics to Jet Noise Research and Prediction," *International Journal of Computational Fluid Dynamics*, vol. 18, pp. 481–491, Aug. 2004.

[71] C. K. W. Tam, "Computational Aeroacoustics: An Overview of Computational Challenges and Applications," *International Journal of Computational Fluid Dynamics*, vol. 18, pp. 547–567, Aug. 2004.

[72] C. Bailly and D. Juve, "Numerical Solution of Acoustic Propagation Problems Using Linearized Euler Equations ," *AIAA Journal*, vol. 38(1), pp. 22–29, 2000.

[73] R. Ewert and W. Schroder, "On the simulation of trailing edge noise with a hybrid LES/APE method," *Journal of Sound and Vibration*, vol. 270(3), pp. 509–524, 2002.

[74] C. K. W. Tam, "Recent advances in computational aeroacoustics," *Fluid Dynamics Research*, vol. 38, pp. 591–615, Sept. 2006.

[75] V. L. Wells and R. A. Renaut, "Computing Aerodynamically Generated Noise," *Annual Review of Fluid Mechanics*, vol. 29, pp. 161–199, 1997.

[76] N. Curle, "The Influence of Solid Boundaries upon Aerodynamic Sound," *Proceedings of the Royal Society of London, Series A, Mathematical and Physical Sciences*, vol. 231, no. 1187, pp. 505–514, 1955.

[77] M. E. Goldstein, *Aeroacoustics*. New York: McGraw-Hill International Book Co, 1976.

[78] F. Farassat and M. K. Myers, "Extension of Kirchhoff's formula to radiation from moving surfaces," *Journal of Sound and Vibration*, vol. 123, no. 3, pp. 451 – 461, 1988.

[79] K. S. Brentner and F. Farassat, "An Analytical Comparison of the Acoustic Analogy and Kirchoff Formulation for Moving Surfaces," *AIAA Journal*, vol. 36, no. 8, pp. 1379–1386, 1998.

[80] K. S. Brentner and F. Farassat, "Modeling aerodynamically generated sound of helicopter rotors," *Progress in Aerospace Sciences*, vol. 39, pp. 83–120, 2003.

[81] F. Farassat, M. J. Doty, and C. A. Hunter, "The Acoustic Analogy A Powerful Tool in Aeroacoustics with Emphasis on Jet Noise Prediction," in *10th AIAA/CEAS Aeroacoustics Conference, AIAA Paper 2004-2872*, May 2004.

[82] C. A. Hunter and R. H. Thomas, "Development of a Jet Noise Prediction Method for Installed Jet Configurations," in *9th AIAA/CEAS Aeroacoustics Conference, AIAA Paper 2003-3169*, May 2003.

[83] F. Farassat, "Discontinuities in Aerodynamics and Aerocoustics: the Concept and Application of Generalized Derivatives," *Journal of Sound and Vibration*, vol. 55, no. 2, pp. 165–193, 1977.

[84] F. Farassat, "Introduction to Generalized Function with Applications in Aerodynamics and Aeroacoustics," tech. rep., NASA Technical Paper 3428, 1996.

[85] F. Farassat and G. P. Succi, "The prediction of helicopter rotor discrete frequency noise," in *American Helicopter Society, Annual Forum, 38th, (A82-40505 20-01)*, pp. 497–507, May 1982.

[86] F. Farassat and M. Farris, "The Mean Curvature of the Influence Surface of Wave Equation With Sources on a Moving Surface," *Journal Mathematical Methods in the Applied Sciences*, vol. 22, pp. 1485–1503, 1999.

[87] P. di Francescantonio, "A New Boundary Integral Formulation for the Prediction of Sound Radiation," *Journal of Sound and Vibration*, vol. 202, no. 4, pp. 491–509, 1997.

[88] F. Farassat and T. J. Brown, "A New Capability for Predicting Helicopter Rotor and Propeller Noise Including the Effect of Forward Motion," *NASA TM X-74037*, 1977.

[89] G. Rahier and J. Prieur, "An efficient Kirchhoff integration method for rotor noise prediction starting indifferently from subsonically or supersonically rotating meshes," in *AHS, Annual Forum, 53rd* (ONERA, ed.), TP-1997-48, (Virginia Beach, VA), 1997.

[90] M. Kessler and S. Wagner, "Source-time dominant aeroacoustics," *Computers and Fluids*, vol. 33(5-6), pp. 791–800, 2004.

[91] D. Casalino, "An advanced time approach for acoustic analogy predictions," *Journal of Sound Vibration*, vol. 261, pp. 583–612, Apr. 2003.

[92] A. S. Lyrintzis, "Surface Integral Methods in Computational Aeroacoustics - From the (CFD) near-field to the (Acoustic) far-field," *International Journal of Aeroacoustics*, vol. 2, no. 2, pp. 95–128, 2003.

[93] W. H. Press, S. A. Teukolsky, W. T. Vetterling, and B. P. Flannery, *Numerical Recipes in FORTRAN; The Art of Scientific Computing*. New York, NY, USA: Cambridge University Press, 1993.

[94] J. G. Leishman, *Principles of Helicopter Aerodynamics*. Cambridge University Press, 1st ed., 2000.

[95] R. W. D. Nickalls, "A New Approach to Solving the Cubic: Cardan's Solution Revealed," *The Mathematical Gazette*, vol. 77(480), pp. 354–359, 1993.

[96] K. S. Brentner, "Numerical Algorithms for Acoustic Integrals with Examples for Rotor Noise Prediction," *AIAA Journal*, vol. 35, no. 4, pp. 625–630, 1997.

[97] C. A. Felippa, *Introduction to finite elements.* Internet Source, http://www.colorado.edu/engineering/CAS/courses.d/IFEM.d/Home.html, 2004.

[98] P. J. Roache, "Quantification of Uncertainty in Computational Fluid Dynamics," *Annu. Rev. Fluid Mech.*, vol. 160, pp. 29–123, 1997.

[99] V. L. Wells, "Acoustic Waveform Singularities from Supersonic Rotating Surface Sources," *AIAA Journal*, vol. 29, no. 3, pp. 387–394, 1991.

[100] G. Rahier, J. Prieur, and F. Vuillot, "Ivestigation of Integral Surface Formulation for Acoustic Predictions of Hot Jets Starting From Unsteady Aerodynamic Simulations," in *9th AIAA/CEAS Aeroacoustics Conference and Exhibit, AIAA 2003-3164*, May 2003.

[101] A. Bagai and J. Leishman, "Flow visualization of compressible vortex structures using density gradient techniques," *Experiments in Fluids*, vol. 15, pp. 431–442, 1993.

[102] S. Loiodice, A. Kokkalis, D. Drikakis, G. Perez, P. Rita, and G. Bernardini, "Assessment of computational tools for the prediction of BVI noise," in *Proccedings of the 32nd European Rotorcraft Forum*, (Maastricht, Netherlands), 2006.

[103] M. J. Baghwat and J. Leishman, "Generalised viscous vortex model for application to free-vortex wake and aeroacoustic calculations," in *Proceedings of the Annual Forum of the American Helicopter Society*, May 2002.

[104] A. Povitsky, T. Zheng, and G. Vatistas, "Effect of vortex profile on sound generation in a non-uniform flow," *Mathematics and Computers in Simulation*, vol. 65, pp. 447–468, 2004.

[105] W. Rankine, *Manual of Applied Mechanics.* C. Griffen Co., London, 1858.

[106] H. Lamb, *Hydrodynamics, 6th ed.* Cambridge University Press, Cambridge, UK, 1932.

[107] G. Taylor, "On the Dissipation of Eddies," *The Scientific Papers of Sir Geoffrey Ingram Taylor*, vol. 2, pp. 96–101, 1958.

[108] G. Vatistas, "New Model for Intense Self-Similar Vortices," *J. Propul. Power*, vol. 14, no. 4, pp. 462–469, 1998.

[109] T. Colonius, S. Lele, and P. Moin, "The scattering of sound waves by a vortex: numerical simulations and analytical solutions," *J. Fluid Mech.*, vol. 260, pp. 271–298, 1994.

[110] M. P. Scully and J. P. Sullivan, "Helicopter Rotor Wake Geometry and Airloads And Development of Laser Doppler Velocimetry for Use in Rotor Wakes," tech. rep., Massachusetts Institute of Technology, Aerophysics Laboratory, Technical Report 183, 1972.

[111] L. Tang and J. D. Baeder, "Adaptive Euler Simulations of Airfoil-Vortex Interaction," *Int. J. Numer. Meth. Fluids*, vol. 53, pp. 777–792, 2007.

[112] R. Morvant, K. J. Badcock, G. N. Barakos, and B. E. Richards, "Airfoil-vortex interaction using the compressible vorticity confinement method," *AIAA Journal*, vol. 43, no. 1, pp. 63–75, 2005.

[113] W. S. Oh, J. S. Kim, and O. J. Kwon, "Numerical simulation of two-dimensional blade-vortex interactions using unstructured adaptive meshes," *AIAA Journal*, vol. 40, no. 3, pp. 474–480, 2002.

[114] S. Lee and D. Bershader, "Head-on parallel blade-vortex interaction," *AIAA Journal*, vol. 32, no. 1, pp. 16–22, 1994.

[115] G. R. Srinivasan, , and W. J. McCroskey, "Numerical Simulations of Unsteady Airfoil-Vortex Interactions," *Vertica*, vol. 11, no. 1, p. 328, 1987.

[116] O. Rouzaud, J. Raddatz, and J. C. Boniface, "Euler calculations of multi-bladed rotors in hover by DLR and ONERA methods and comparison with HELISHAPE tests," in *53rd AHS Annual Forum*, pp. 1102–1114, May 1997.

[117] M. H. L. Hounjet, "Common Test Cases for Task 2.2.2," friendcopter report, Friendcopter, 2004.

[118] R. Ponza, "Flying Helicopters Acoustic impact assessment: towards a more realistic simulation methodology," in *ECCOMAS*, July 2004.

[119] M. Gennaretti and G. Bernardini, "A Novel Potential-Flow Boundary Integral Formu-lation for Helicopter Rotors in BVI Conditions," in *Proceedings of the 11th AIAA/CEAS Aeroacoustics Conference, AIAA Paper 2005-2924*, May 2005.

[120] D. Hodges and O. R.A., "Stability of Elastic Bending and Torsion of Uniform Cantilever Rotor Blades in Hover with Variable Structural Coupling, NASA TN D-8192," tech. rep., European Commission, 1976.

[121] A. S. Morgans, S. A. Karabasov, A. P. Dowling, and T. P. Hynes, "Transonic helicopter noise," *AIAA Journal*, vol. 43, no. 7, pp. 1512–1524, 2005.

[122] J. Prieur, M. Costes, and J. D. Baeder, "Aerodynamic and Acoustic Calculations of Transonic Nonlifting Hovering Rotors," *Journal of the America Helicopter Society*, vol. 41, no. 2, pp. 17–26, 1996.

[123] M. Isom, T. Purcell, and R. Strawn, "Geometrical Acoustics and Transonic Helicopter Sound," in *11th AIAA Aeroacoustics Conference, AIAA-87-2748*, Oct. 1987.

[124] Y. Delrieux, J. Prieur, G. Rahier, and G. Drousie, "A new implementation of aeroacoustic integral method for supersonic deformable control surfaces," in *9th AIAA/CEAS Aeroacoustics Conference and Exhibit, AIAA 2003-3201*, May 2003.

Appendix A

Generalized Functions: basics

In this appendix, the basic properties and definitions of Generalized Functions are shown. These are the tools which allow to obtain the FW-H equation from Lighthill's Analogy.

Let $f(x)$ be a piecewise continuous function with a discontinuity at x_0 such that $\Delta f = f(x_{0_+}) - f(x_{0_-})$. If we want to take the generalized derivative of f, we have:

$$\frac{\overline{d}f}{dx} = \overline{f}'(x) = f'(x) + \Delta f \delta(x - x_0) \tag{A.1}$$

In which $\delta(x)$ is the Dirac delta function. The useful properties of generalized derivatives is that:

$$\int_a^x \frac{\overline{d}f}{dx} \mathrm{d}x = f(x) - f(a) \neq \int_a^x f'(x) \mathrm{d}x \tag{A.2}$$

More in general, if we refer to a function $q(\mathbf{x})$ that is discontinuous across a surface $h(\mathbf{x}) = 0$, we can define the jump of q as $\Delta q = q(f = 0+) - q(f = 0-)$. Thus the partial generalized derivative of $q(\mathbf{x})$ is:

$$\frac{\overline{\partial}q}{\partial x_i} = \frac{\partial q}{\partial x_i} + \Delta q \frac{\partial f}{\partial x_i} \delta(f) \tag{A.3}$$

It easy to derive from the previous equation the form of ∇q.

Certainly a good property to show for the Dirac delta function is:

$$\int_V F(\mathbf{x}) |\nabla f| \delta(f) \mathrm{d}\mathbf{x} = \int_{f=0} F(\mathbf{x}) \mathrm{d}S$$

In which the integral in the right part is a surface integral on the surface $f = 0$.

Another important property of the generalized derivatives it that the order of the

operators can be exchanged, for instance:

$$\frac{\overline{\partial}}{\partial x_j}\int_V F(\mathbf{x})\mathrm{d}\mathbf{x} \;=\; \int_V \frac{\overline{\partial}}{\partial x_j}F(\mathbf{x})\mathrm{d}\mathbf{x}$$

supposed that the limits of the integral are not a function of x_j.

All these properties stated above are useful when we have to deal with discontinuities of any type.